Theoretical and Finite Element Analysis of

Origami and Kirigami Based Structures

by

Cheng Lv

A Dissertation Presented in Partial Fulfillment
of the Requirements for the Degree
Doctor of Philosophy

Approved July 2016 by the
Graduate Supervisory Committee:

Hanqing Jiang, Chair
Hongbin Yu
Liping Wang
Marc Mignolet
Owen Hildreth

ARIZONA STATE UNIVERSITY

August 2016

ABSTRACT

Origami and kirigami, the technique of generating three-dimensional (3D) structures from two-dimensional (2D) flat sheets, are now more and more involved in scientific and engineering fields. Therefore, the development of tools for their theoretical analysis becomes more and more important. Since much effort was paid on calculations based on pure mathematical consideration and only limited effort has been paid to include mechanical properties, the goal of my research is developing a method to analyze the mechanical behavior of origami and kirigami based structures. Mechanical characteristics, including nonlocal effect and fracture of the structures, as well as elasticity and plasticity of materials are studied. For calculation of relative simple structures and building of structures' constitutive relations, analytical approaches were used. For more complex structures, finite element analysis (FEA), which is commonly applied as a numerical method for the analysis of solid structures, was utilized. The general study approach is not necessarily related to characteristic size of model. I believe the scale-independent method described here will pave a new way to understand the mechanical response of a variety of origami and kirigami based structures under given mechanical loading.

DEDICATION

I dedicate my dissertation work to my family and friends. Firstly, I shall give my special thanks to my parents, Dr. Jianwei Lv and Mrs. Yanxia Jiang, who let me know the world and always try their best to support me to pursue my dreams. Then I shall say thank you to my wife Yu Luo whose love, support and encouragement have always been the light of my life, and my daughter Rebecca X. Lv who is a gift from the beginning.

I shall also say thank you to many of my friends. My friends Zeming Song, Xu Wang, Yiling Fan, Teng Ma, Wenwen Xu and Haokai Yang give me lots of help and advice. It is my great pleasure to work with you and have you as my friends. And special thanks to Yong Wang who broadened my horizons on my study.

ACKNOWLEDGMENTS

I wish to thank my committee members who gave their precious time to help me throughout the whole process. Special thanks go to Dr. Hanqing Jiang, my committee chairman, who not only patiently taught me knowledge of solid mechanics and modelling, but also gave me guidance on my life. These moments will be the treasures of my life. I shall also thank Dr. Hongbin Yu, Dr. Liping Wang, Dr. Marc Mignolet and Dr. Owen Hildreth for agreeing to serve on my committee.

I would like to acknowledge and thank SEMTE for allowing me to conduct my research and providing any assistance requested. Special thanks go to the members of staff development and human resources department for their continued support.

TABLE OF CONTENTS

Page

CHAPTER Page

APPENDIX Page

LIST OF FIGURES

Figure Page

CHAPTER 1 : INTRODUCTION

1.1. Outline

This dissertation begins with Chapter 1 for introduction. In this chapter, background of work related to origami and kirigami based structure will be briefly summarized in Section 1.2. Then, a brief introduction of conventional finite element method will be shown in Section 1.3. After that, the nonlocal finite element method, which is specially designed by me for the study for the nonlocal effect of 3D complex rigid origami, will be introduced in Section 1.4. In this section, the relationship between the nonlocal finite element method (NFEM) and the conventional finite element method will also be discussed. After the introduction of the necessary background, detailed study will be included in the following chapters. My research begins with the study of origami based structures. In Chapter 2, the most simple but also the most well-known origami pattern—Miura-ori, will be studied. By taking advantage of its periodic characteristics, an analytical expression of the Poisson's ratio for Miura-ori is derived[1]. By introducing the non-periodic feature of the unit cell, which has long been ignored by others, new and interesting results can be obtained. Then, for a more complex non-periodic rigid origami, it is impossible to reach an analytical solution. Instead, a numerical method should be introduced. In Chapter 3, a non-periodic rigid origami pattern called water bomb will be studied[1] as an example. NFEM, which is originate from atomic-scale finite element method (AFEM)[2] (See details in Section 1.4), is applied as the tool to analyze water bomb pattern under given complex boundary conditions. This specific case is shown here to illustrate the generality of NFEM on the study of rigid origami based structures. It is

proved to give a good accuracy. After the study of rigid origami, non-rigid origami is considered. In Chapter 4, a commonly observed locking effect was captured in finite element analysis (FEA) by including plasticity in the analysis. It suggests the long ignored plasticity during modelling of origami should be included. After having the three projects related macroscale origami, my study begins to focus on microscale origami. In Chapter 5, I developed a new manufacture process of microscale silicon origami, *i.e.* using buckling of silicon thin film bonded by predesign soft suspension (or wall), which was impossible to obtain before on this small scale. This process is guided under the prediction from FEA, which enables people to design the pattern and predict its deformation behaviors without the need of physical experiment. After finishing all the study for origami based structures, kirigami based structures, which provides more degree of freedom compared with origami based ones, attract me by their much higher stretchability. In Chapter 6, analysis is carried out on kirigami based lithium-ion battery[3]. Both fracture, which is introduced during cutting process, and plastic, which is introduced during folding process, are considered during the modelling process. By an approach combines numerical and analytical method, the fracture of kirigami based lithium-ion battery can be avoided. In Chapter 7, by taking advantage of the stretchability of kirigami and observations of existing design of stretchable interconnection, an innovative non-periodic spiral-based pattern for the interconnection in electrical circuit was created, optimized and analyzed[4]. It is proved by FEA that the new design provide much higher stretchability.

1.2. Background

Origami and kirigami, originally two kinds of the traditional art form of paper folding, which create 3D structures from 2D sheets, have become a source of inspiration for not only artists (See example of origami and kirigami in Fig. 1.1) but also scientists and engineers. The former involves only folding along the crease while the latter also involves cutting to form desired pattern.

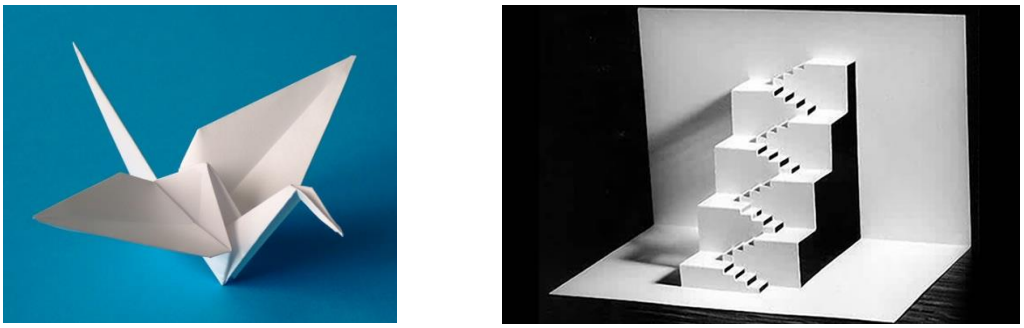

A **B**

Fig. 1.1. Example of origami and kirigami. (**A**) Paper made origami crane. Reprinted from Origami crane, In *Wikipedia*, n.d., Retrieved June 28, 2016, from https://en.wikipedia.org/wiki/Origami#/media/File:Origami-crane.jpg. Copyright 2006 by Andreas Bauer. Reprinted with permission. (**B**) Paper made foldable kirigami stairs. Reprinted from Stairs to Paradise A, In *Virtual Gallery of Origamic Architecture*, Retrieved June 28, 2016, from http://webpages.charter.net/gstormer/. Copyright1999 by Gerry Stormer. Reprinted with permission.

By utilizing the origami's deformability and compactness, its applications range from space exploration (*e.g.*, a foldable telescope lens[5]) to automotive safety (*e.g.*, airbags[6]), biomedical devices (*e.g.*, heart stent[7]), and extremely foldable and stretchable

electronics[8,9]. An example of buckling induced Miura-ori, the simplest origami pattern, based polymer (SU8) structure is shown in Fig. 1.2A[10]. The method to obtain the pattern is commonly applied for the fabrication of origami pattern. Another example, which is shown in Fig. 1.2B[8], illustrates a solar cell design based on the idea of Miura-ori. Instead of starting from a continued 2D flat sheet, the crease pattern is formed by assembly of individual solar panels by multiple hinges. Recently investigation has been done on self-folding by external stimuli (e.g., light and temperature) and novel materials (e.g., shape memory polymers and alloys, gels)[11-17] (examples shown in Fig. 1.2 C and D). In Fig. 1.2C[16], self-folded hydrogel cube is shown. Since the gel is thermal sensitive, by changing the temperature, it can deform automatically. In Fig. 1.2D, a light sensitive gel is made by applying radiation to the material and releasing the strain to enable the self-folding of the structure. Among all types of origami, a specific one called rigid origami, in which the faces between the creases remain rigid during folding/unfolding and only the creases deform, is different from most origami patterns that require faces bending or partial crumpling to make many-step folds. Due to its finite number of degrees of freedom, the deformation of it can be well controlled. Thus, it can be readily used as a new kind of metamaterial[18], *i.e.* man-made material that can hold properties hardly found in natural ones.

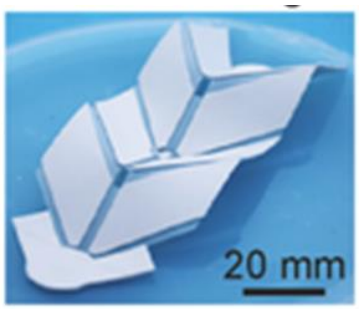

A

B

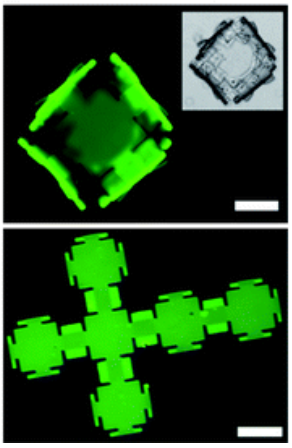

C

D

Fig. 1.2. Photos of origami based structures. (**A**) Origami pattern made by SU8 polymer. (**B**) Origami based solar cell. In this photo, each of solar panels (shown as yellow part) is connected with other ones by hinges. (**C**) Fluorescence (top) and optical micrographs (inset) of a self-folded hydrogel cube at room temperature made of five tri-strip hinges connecting six square plates. Upon increasing the temperature to $50^{\circ}C$, the cube unfolds (bottom). Scale bars: $300\,\mu m$. (**D**) A six-sided box fabricated by photo-origami that with multiple hinges.

On the other hand, if the face is considered to be deformable, many interesting phenomenon, including defects in origami pattern[19], bending in faces[20,21] can be studied. In Fig. 1.3[19], A and B, different defects of origami can be obtained by introducing the vertex dislocations. Simple analytical solution is obtained to study the sensitivity of defect in various boundary conditions. In Fig. 1.3C[21], a simple theory based on variational method is developed to study the stability of origami, conical surfaces, based metamaterial. A bi-stability is discovered.

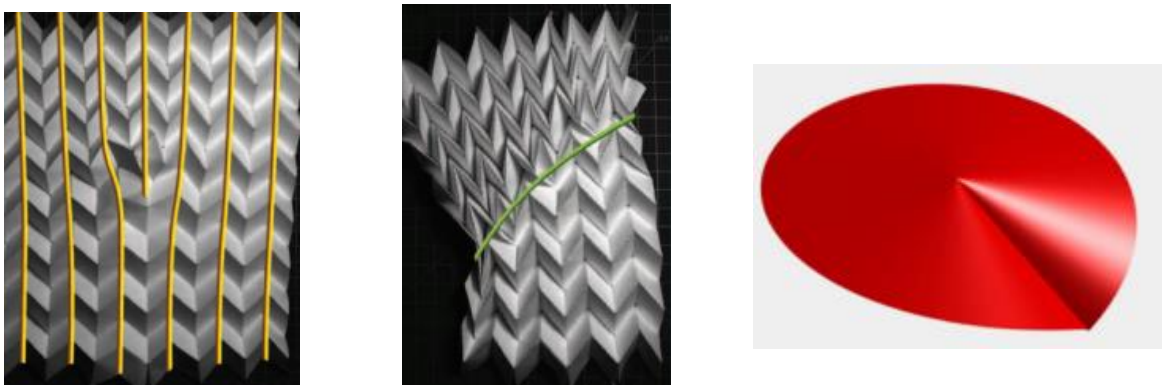

A **B** **C**

Fig. 1.3. Theory of origami based structures. (**A**) and (**B**) shows study of edge dislocation generated by lattice vacancies and grain boundary generated by edge dislocation. (**C**) Theoretical prediction of f-cone patterns corresponding to semi-infinite crease configuration.

Compared with origami, kirigami has its own advantages. By involving the cutting process, the resulted structure has more degrees of freedom. This will normally introduce the out-of-plane deformation, with which the strain concentration can be dramatically reduced[22-25]. Based on the fact, numerous works focus on the design of kirigami based interconnection. In Fig. 1.4, finite element analysis is carried out to study the deformation of self-similar serpentine based interconnection design. It is clear from the figure, even with a 100% stretch applied on the interconnection, the maximum strain is still about 1%. This indicates the ability of kirigami based structure to reduce strain concentration.

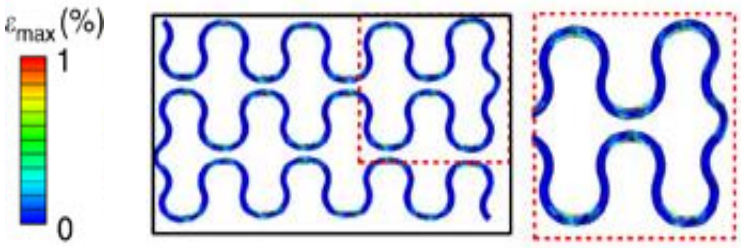

Fig. 1.4. Results from finite element analysis of self-similar serpentine kirigami based interconnection. In this figure, strain contour and the corresponding legend are given. 100% stretch is applied on the interconnection. A zoom in view is given to see the positions for relative high strain.

Large deformation is common for the practical application of origami and kirigami based structures, which indicates the significance of mechanics analysis. Although notable progress has been made in the area of origami theory including tree

theory[26] and its corresponding computer program[27] (figure of the interface shown in Fig. 1.5A), folding along creases[28-32], imperfection study[19], foldability of rigid origami[33], general pattern design[26,34,35] and geometric mechanics of a periodic folding pattern[36] (figure of the contour of Poisson's ratio is shown in Fig. 1.5B), few contain the understanding from a finite element aspect. Finite element analysis (FEA), a numerical method which originates from the principle of virtual displacement to solve the weak form partial differential equation, is currently the most widely used method in the area of solid mechanics, especially for analysis of 3D complex geometry. Since a large number of faces and creases are included in origami based structures, FEA becomes the best choice for their simulation. Based on the facts mentioned above, my research topic focuses on applying analytical method and FEA on the study of origami and kirigami based structures.

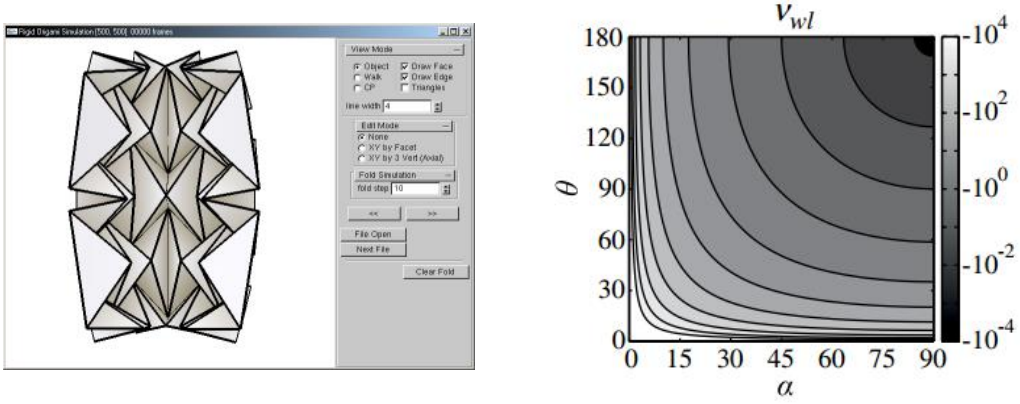

A **B**

Fig. 1.5. Figures for the existing theories of origami. (**A**) Interface of the software, which is called Rigid Origami Simulator, with a 3D configuration of water bomb shown. (**B**) In-plane Poisson's ratio of Miura-ori. Here, angle α decides the shape of faces and

angle θ is the dihedral angle which measures the folding degree of the pattern. It can be found the in-plane Poisson's ratio will always be negative in the contour plot.

1.3. Conventional Finite Element Method

This section serves as the background introduction of conventional nonlinear finite element method for large displacement. The content in this section will cover a brief derivation of the formula for finite element method originates from displacement based virtual work principle. In Section 1.3.1, a brief introduction for the background of finite element method will be given. In Section 1.3.2, useful knowledge of continuum mechanics for large deformation will be introduced. The PDE obtained in this section will be approximately solved using finite element method. This is one of the key points for nonlinear finite element method. In Section 1.3.3, the variational form of finite element formula will be obtained based on the PDE obtained in Section 1.3.2. In Section 1.3.4, linearization of the nonlinear formula obtained in Section 1.3.3 will be introduced. And, the final expression for nonlinear finite element method will be obtained. The derivation process discussed in this section will be used to compare with the special finite element methods introduced in Section 1.4. It will help the reader to understand the derivation of special finite element method better.

1.3.1. Introduction of Conventional Finite Element Method

In the macro-scale viewpoint, objects in the real world are commonly treated as continuum, which means their physical behaviors can normally be mathematically modelled by using partial differential equation (PDE). However, due to limits of computational capability, only few PDE with simple boundary condition (BC) and solving domains can be solved analytically (or exactly). Instead, for complex PDE with

complex BCs and solving domains, approximation should be made, which leads to numerical method. Numerical method, as a general approximation method, simplifies the PDE, the corresponding BC and solving domain by using the proper assumptions.

To solve problems in the solid mechanics field which are impossible to solve analytically, finite element method, as a numerical method with long history, is commonly applied. It introduces the equilibrium on an integral level, not on a pointwise one. By introducing this assumption, the continuum in the real world is discretized into a finite number of smaller pieces, called elements in FEM, so that complex structures can be analyzed. The discretization process is based on a variational method called principle of virtual work, which basically says in the equilibrium state, the total virtual work done by external forces should equal the total virtual work done by internal forces. Generally speaking, there are two types of principle of virtual work. One is displacement based while the other is force based. The difference is due to the fact that in variational method, variation is taken with respect to the primary variable. In the former, variation is taken on displacement while in the later, variation is taken on force. Normally, in the solid mechanics field, displacement is chosen as the primary variable. So finite element method is commonly displacement based. Considering the elastic body as a special case, the principle of virtual work can also be called the minimum total potential energy principle, which just states that the real motion of objects is the kinematically admissible one which can minimize the total potential energy of the object.

1.3.2. Useful Basics of Continuum Mechanics

In order to obtain the formulation of displacement based FEM, several concepts of continuum mechanics should be introduced. Firstly, some basic definitions should be given. As shown in Fig. 1.6, for large deformation theory in continuum mechanics, the volume (or domain) to solve PDE is different for reference and current state. If the position of any point of interest P can be represented by $\mathbf{X}$ and $\mathbf{x}$ for reference and current state, respectively, the mapping between these two states can be shown as $\mathbf{x}=\mathbf{x}(\mathbf{X},t)$.

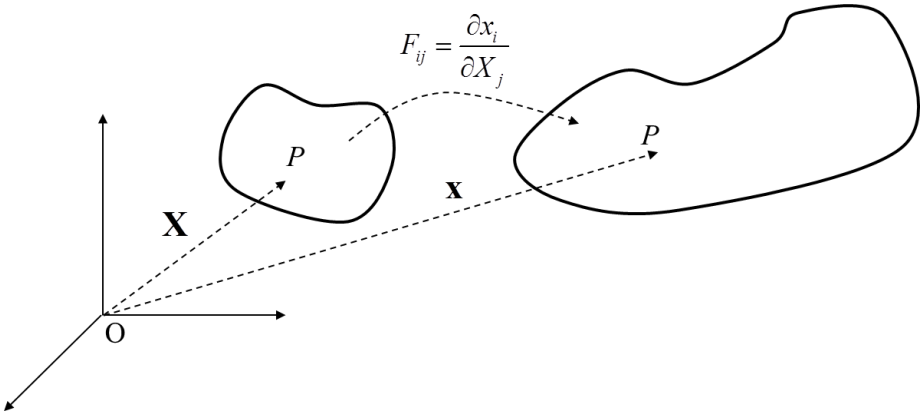

Fig. 1.6. The configurations of an object under deformation at reference and current states. As it is shown, an example point P moves from reference configuration on left to current configuration on right. Deformation gradient F_{ij} will serve as a bridge between current and reference coordinates, represented by $\mathbf{x}$ and $\mathbf{X}$, respectively .

Then, the two positions of the same point can be linked using the deformation gradient $F_{ij} = \frac{\partial x_i}{\partial X_j}$ as:

$$dx_i = \frac{\partial x_i}{\partial X_j} dX_j \tag{1}$$

Secondly, the governing equation needs to be solved. It is based on the conservation of linear momentum, *i.e.* force equilibrium. According to the integral form of conservation of linear momentum, the following can be obtained:

$$\frac{d}{dt}\int_V \rho v_i dV = \int_S f_i^S dS + \int_V f_i^B dV \tag{2}$$

Here, V and S are current volume (or domain) and surface (or boundary) of the continuum, respectively. ρ is the current density of the continuum. f_i^S and f_i^B are the surface traction and the body force of the continuum on i-direction, respectively. i can be 1, 2 and 3, which correspond to x, y and z, respectively. The subscript i, if it appears individually, will always mean the direction. This rule will be followed in the rest of the dissertation. t is time. v_i is velocity.

Using the Cauchy stress principle and divergent theorem, the following can be obtained:

$$\frac{d}{dt}\int_V \rho v_i dV = \int_S \tau_{ij} n_j dS + \int_V f_i^B dV = \int_V \tau_{ij,j} dV + \int_V f_i^B dV \tag{3}$$

Here, τ_{ij} is the Cauchy stress on the surface with normal on i-direction and points to j direction. n_i is the component of the normal vector on i-direction. ρ_0 is the density corresponding to reference configuration.

Also, note that the LHS of the equation can be transformed as the following:

$$\frac{d}{dt}\int_V \rho v_i dV = \frac{d}{dt}\int_{V_0} \rho v_i J dV_0 = \int_{V_0} \left(\dot{\rho J}\right) v_i dV_0 + \int_{V_0} \rho J \dot{v}_i dV_0$$
$$= \int_{V_0} \dot{\rho}_0 v_i dV_0 + \int_V \rho \dot{v}_i dV = \int_V \rho \dot{v}_i dV \tag{4}$$

Here, V_0 is the volume of the object in reference state. J is the determinant of the deformation gradient $\mathbf{F}$. The dot-hat means time derivative.

Finally, the following can be obtained:

$$\int_V \left(\rho \dot{v}_i - \tau_{ij,j} - f_i^B\right) dV = 0 \tag{5}$$

As the volume of integration is arbitrary, the differential form for the conservation of linear momentum can be obtained:

$$\tau_{ij,j} + f_i^B = \rho \dot{v}_i \tag{6}$$

For the static case, $\rho \dot{v}_i = 0$ is satisfied, the following can be obtained:

$$\tau_{ij,j} + f_i^B = 0 \tag{7}$$

1.3.3. Derivation of General Formula

The derivation should begin with the derivation of the virtual work principle[37] (exclude the damping and the inertial terms):

The variation of external virtual work can be written as:

$$\begin{aligned}\delta W_{ext} &= \int_V f_i^B \delta u_i dV + \int_{S_f} f_i^S \delta u_i^S dS \\ &= \int_V f_i^B \delta u_i dV + \int_S f_i^S \delta u_i^S dS \\ &= \int_V f_i^B \delta u_i dV + \int_S \tau_{ij} n_j \delta u_i^S dS \\ &= \int_V \left(f_i^B + \tau_{ij,j} \right) \delta u_i dV + \int_V \tau_{ij} \delta u_{i,j} dV\end{aligned} \tag{8}$$

Here, δ means taking the variation by adding the symbol. So δu_i is the variation of displacement u_i. δu_i^S is the variation of displacement on the boundary.

As it is known from continuum mechanics, the body in its equilibrium state should satisfy $f_i^B + \tau_{ij,j} = 0$. So, the following can be obtained:

$$\delta W_{ext} = \int_V \tau_{ij} \delta u_{i,j} dV = \int_V \tau_{ij} \delta e_{ij} dV = \delta W_{\text{int}} \tag{9}$$

Here the symmetry of stress tensor $\boldsymbol{\tau}$ is applied so that

$$\tau_{ij} \delta u_{i,j} = \frac{1}{2}\left(\tau_{ij} \delta u_{i,j} + \tau_{ji} \delta u_{i,j} \right) = \frac{1}{2}\left(\tau_{ij} \delta u_{i,j} + \tau_{ij} \delta u_{j,i} \right) = \tau_{ij} \left[\frac{1}{2}\left(\delta u_{i,j} + \delta u_{j,i} \right) \right] = \tau_{ij} \delta e_{ij} \tag{10}$$

So, it can be found that the principle of virtual displacement just says that for a body in equilibrium, the variation of total internal virtual work equals the variation of total external virtual work under any kinematically admissible displacement field. It should be noted that this principle is valid for any constitutive relation.

$$\begin{aligned} \delta W_{\text{int}} &= \int_V \tau_{ij}\delta e_{ij} dV \\ \delta W_{ext} &= \int_V f_i^B \delta u_i dV + \int_{S_f} f_i^S \delta u_i^S dS \\ \delta W_{\text{int}} &= \delta W_{ext} \end{aligned} \tag{11}$$

This is the general formula for linear FEM. For large deformation, as discussed in the last section, difference between reference and current configuration needs to be taken into consideration. As the integration domain, *i.e.* current volume, is unknown before solving the PDE, the formula above is difficult to handle. Therefore, transformation is needed to change the integration domain from current volume to reference volume. Then, the modified formula will be easier to deal with. About the choice of the reference state, two candidates are available—initial configuration and configuration computed at last iteration. The former corresponds to total Lagrangian (TL) formulation while the later corresponds to updated Lagrangian (UL) formulation. In the following derivation, the TL formulation will be considered. Note here UL formulation can also be obtained in a very similar way. So, in order to transfer the formula from the configuration in current state to the reference one, the following derivation will be necessary:

$$\begin{aligned} \delta W_{\text{int}} &= \int_V \tau_{ij}\delta e_{ij} dV = \int_V \left(\frac{{}^t\rho}{{}^0\rho} S_{kl} F_{ik} F_{jl} \right) \left(F_{mi}^{-1} F_{nj}^{-1} \delta\varepsilon_{mn} \right) dV \\ &= \int_V \frac{{}^t\rho}{{}^0\rho} S_{kl}\delta_{km}\delta_{\ln}\delta\varepsilon_{mn} dV = \int_{{}^0V} S_{kl}\delta\varepsilon_{kl} d\,{}^0V \end{aligned} \tag{12}$$

Here the formulas $\tau_{ij} = \frac{{}^t\rho}{{}^0\rho} S_{kl} F_{ik} F_{jl}$ and $e_{ij} = F_{mi}^{-1} F_{nj}^{-1} \varepsilon_{mn}$ in large deformation theory in continuum mechanics are applied. S_{ij} is second-PK stress. ε_{ij} is Green-Lagrangian strain tensor.

So, the general formulation for large deformation is as follows:

$$\int_{{}^0V} S_{ij}\delta\varepsilon_{ij} d\,{}^0V = \delta W_{ext} \tag{13}$$

1.3.4. Linearization of General Formula

Normally, the nonlinear PDE as shown in the last section cannot be solved analytically. Therefore, numerical method should be applied to give an approximated result. In order to readily solve the general nonlinear formula numerically, a process must be taken to make it solvable. One of the techniques is making a linearization of it. After linearization, techniques for linear algebra can be applied. Note here the linearization process is where approximation is introduced for the first time. The obtained results are then approximated results. The method can be called the incremental step-by-step method. Assume the time of interest is from 0 to $t+\Delta t$, which is properly discretized into shorter time steps (*e.g.* 0 to Δt, Δt to $2\Delta t$, $2\Delta t$ to $3\Delta t$, …). Δt is the chosen time increment in the current step. The solution from 0 to t has already been obtained. Consider the force balance at time $t+\Delta t$:

$$ {}^{t+\Delta t}\mathbf{F}_{ext} - {}^{t+\Delta t}\mathbf{F}_{\text{int}} = \mathbf{0} \tag{14} $$

where $\mathbf{F}_{ext}$ and $\mathbf{F}_{\text{int}}$ are external and internal force vectors, respectively.

Assume ${}^{t+\Delta t}\mathbf{F}_{\text{int}}$ is independent of deformation and the incremental decomposition is possible for $\mathbf{F}_{\text{int}}$, *i.e.* ${}^{t+\Delta t}\mathbf{F}_{\text{int}} = {}^{t}\mathbf{F}_{\text{int}} + \mathbf{F}_{\text{int}}$. And, introduce that approximation for the increment $\mathbf{F}_{\text{int}}$ has the following relation:

$$ \mathbf{F}_{\text{int}} \doteq {}^{t}\mathbf{K}\mathbf{U} \tag{15} $$

where ${}^{t}\mathbf{K} = \dfrac{\partial {}^{t}\mathbf{F}}{\partial {}^{t}\mathbf{U}}$ is tangential stiffness matrix.

Finally, the linearized equation can be obtained as:

$$ {}^{t}\mathbf{K}\mathbf{U} = {}^{t+\Delta t}\mathbf{F}_{ext} - {}^{t}\mathbf{F}_{\text{int}} \tag{16} $$

This equation written in matrix form is what is actually solved in FEM. In the following, the general FEM formula derived in the last section is linearized in similar fashion to arrive at the same matrix-form equation.

Applying the general formula to current time $t+\Delta t$, the following can be obtained:

$$
\begin{aligned}
{}^{t+\Delta t}W_{\text{int}} &= \int_{{}^{t+\Delta t}V} {}^{t+\Delta t}\tau_{ij}\,\delta\, {}_{t+\Delta t}e_{ij}\, d\, {}^{t+\Delta t}V \\
{}^{t+\Delta t}W_{ext} &= \int_{{}^{t+\Delta t}V} {}^{t+\Delta t} f_i^{\,B}\,\delta u_i\, d\, {}^{t+\Delta t}V + \int_{{}^{t+\Delta t}S_f} {}^{t+\Delta t} f_i^{\,S}\,\delta u_i^{S}\, d\, {}^{t+\Delta t}S \\
{}^{t+\Delta t}W_{\text{int}} &= {}^{t+\Delta t}W_{ext}
\end{aligned}
\tag{17}
$$

Here the subscript $t+\Delta t$ stands for the configuration the derivative taken with respect to is for the current time $t+\Delta t$. The superscript $t+\Delta t$ stands for the value to take the derivative of is taken at the current time $t+\Delta t$. The same rule will be applied in all the following derivation.

Then, the following incremental decompositions should be introduced:

$$
{}^{t+\Delta t}_{0}u_i = {}^{t}_{0}u_i + {}_0u_i \tag{18}
$$

$$
{}^{t+\Delta t}_{0}S_{ij} = {}^{t}_{0}S_{ij} + {}_0S_{ij} \tag{19}
$$

$$
{}^{t+\Delta t}_{0}\varepsilon_{ij} = {}^{t}_{0}\varepsilon_{ij} + {}_0\varepsilon_{ij} \tag{20}
$$

$$
{}_0\varepsilon_{ij} = {}_0e_{ij} + {}_0\eta_{ij} \tag{21}
$$

$$
{}_0e_{ij} = \frac{1}{2}\left({}_0u_{i,j} + {}_0u_{j,i} + {}^{t}_{0}u_{k,i}\,{}_0u_{k,j} + {}_0u_{k,i}\,{}^{t}_{0}u_{k,j} \right) \tag{22}
$$

$$
{}_0\eta_{ij} = \frac{1}{2}\,{}_0u_{k,i}\,{}_0u_{k,j} \tag{23}
$$

Here, ${}_0e_{ij}$ is the linear (with respect to incremental displacement ${}_0u_i$) part of the incremental strain and ${}_0\eta_{ij}$ is the nonlinear part. The value with superscript $t+\Delta t$ is the

one to solve for. The one with superscript t is the result from the last iteration. The one without the superscript is the corresponding incremental value between the two adjacent times.

Then, the following derivation can be obtained:

$$\begin{aligned}
&\int_{{}_0V} {}^{t+\Delta t}_{0}S_{ij}\,\delta\,{}^{t+\Delta t}_{0}\varepsilon_{ij}\,d\,{}^0V = \int_{{}_0V} {}^{t+\Delta t}_{0}S_{ij}\,\delta\left({}^{t}_{0}\varepsilon_{ij} + {}_0\varepsilon_{ij}\right)d\,{}^0V = \int_{{}_0V} {}^{t+\Delta t}_{0}S_{ij}\,\delta\,{}_0\varepsilon_{ij}\,d\,{}^0V \\
&= \int_{{}_0V}\left({}^{t}_{0}S_{ij} + {}_0S_{ij}\right)\delta\,{}_0\varepsilon_{ij}\,d\,{}^0V = \int_{{}_0V} {}_0S_{ij}\,\delta\,{}_0\varepsilon_{ij}\,d\,{}^0V + \int_{{}_0V} {}^{t}_{0}S_{ij}\,\delta\left({}_0e_{ij} + {}_0\eta_{ij}\right)d\,{}^0V \\
&= \int_{{}_0V} {}_0S_{ij}\,\delta\,{}_0\varepsilon_{ij}\,d\,{}^0V + \int_{{}_0V} {}^{t}_{0}S_{ij}\,\delta\,{}_0\eta_{ij}\,d\,{}^0V + \int_{{}_0V} {}^{t}_{0}S_{ij}\,\delta\,{}_0e_{ij}\,d\,{}^0V
\end{aligned} \tag{24}$$

Note here, $\delta\,{}^{t}_{0}\varepsilon_{ij} = 0$ because the variation is taken with respect to $t + \Delta t$. As it is assumed to be given the variation of the displacement field, *i.e.* the value of $\delta\,{}_0u_i$ is known, the second term in the above equation is therefore linear in the incremental displacement ${}_0u_i$. The last term is known. So, only the first term should be linearized.

By using the Taylor series expansion at time t, the first term can be linearized as followed:

$${}^{t+\Delta t}_{0}S_{ij} = {}^{t}_{0}S_{ij} + \frac{\partial\,{}^{t}_{0}S_{ij}}{\partial\,{}^{t}_{0}\varepsilon_{ij}}\,{}_0\varepsilon_{ij} + \text{higher order terms} \tag{25}$$

Then, the following can be obtained:

$$\begin{aligned}
&\int_{{}_0V} {}_0S_{ij}\,\delta\,{}_0\varepsilon_{ij}\,d\,{}^0V = \int_{{}_0V}\left(\frac{\partial\,{}^{t}_{0}S_{ij}}{\partial\,{}^{t}_{0}\varepsilon_{ij}}\,{}_0\varepsilon_{ij} + \text{higher order terms}\right)\delta\left({}_0e_{ij} + {}_0\eta_{ij}\right)d\,{}^0V \\
&= \int_{{}_0V}\left(\frac{\partial\,{}^{t}_{0}S_{ij}}{\partial\,{}^{t}_{0}\varepsilon_{ij}}\left({}_0e_{ij} + {}_0\eta_{ij}\right) + \text{higher order terms}\right)\delta\left({}_0e_{ij} + {}_0\eta_{ij}\right)d\,{}^0V \\
&\qquad\quad \downarrow \qquad\quad \downarrow \qquad\quad \downarrow \qquad\quad \downarrow \\
&\qquad {}_0C_{ijkl} \qquad \text{Neglect} \qquad \text{Neglect} \qquad \text{Neglect} \\
&\doteq \int_{{}_0V} {}_0C_{ijkl}\,{}_0e_{kl}\,\delta\,{}_0e_{ij}\,d\,{}^0V
\end{aligned} \tag{26}$$

Finally, linearized equation for general nonlinear problem can be shown as followed (For total Lagrangian formulation):

$$\int_{{}_0V} {}_0C_{ijkl}\,{}_0e_{kl}\delta\,{}_0e_{ij}\,d\,{}^0V + \int_{{}_0V} {}_0^tS_{ij}\delta\,{}_0\eta_{ij}\,d\,{}^0V = {}^{t+\Delta t}\Re - \int_{{}_0V} {}_0^tS_{ij}\delta\,{}_0e_{ij}\,d\,{}^0V \tag{27}$$

Compared with Equation(16), the following will be clear:

$$\begin{gathered}\int_{{}_0V} {}_0C_{ijkl}\,{}_0e_{kl}\delta\,{}_0e_{ij}\,d\,{}^0V + \int_{{}_0V} {}_0^tS_{ij}\delta\,{}_0\eta_{ij}\,d\,{}^0V = \delta\mathbf{U}^T\,{}^t\mathbf{K}\mathbf{U} \\ {}^{t+\Delta t}\Re = \delta\mathbf{U}^T\,{}^t\mathbf{F}_{ext} \\ \int_{{}_0V} {}_0^tS_{ij}\delta\,{}_0e_{ij}\,d\,{}^0V = \delta\mathbf{U}^T\,{}^t\mathbf{F}_{\text{int}}\end{gathered} \tag{28}$$

As $\delta\mathbf{U}$ is arbitrary, it is clear that Equation (28) above is the final formula to be solved in FEM.

1.4. Nonlocal Finite Element Method

This chapter serves as introduction of two special finite element methods called atomic-scale finite element method and nonlocal finite element method, respectively. The content will cover a brief derivation of the formula atomic-scale finite element method. And, it will be compared with conventional finite element method described in Section 1.3 (in Section 1.4.1). Finally, in Section 1.4.2, the relationship between atomic-scale finite element method and nonlocal finite element method will be discussed. From the comparison of the three different methods, people can understand the origin of nonlocal finite element method which is proposed by author and used to study the nonlocal behaviors of origami based structures in Chapter 4 and 5.

1.4.1. Atomic-scale Finite Element Method and Its Relation with Conventional Finite Element Method

Atomic-scale Finite Element Method (AFEM) is a numerical method designed to combine molecular dynamics and conventional FEM in order to consider the nonlocal mechanical effect of materials. The biggest difference between AFEM and conventional FEM arises from the introduction of element overlaps. The reason to introduce the overlap is that atomic interaction of any atom will, in most of the cases, involve not only its most adjacent atoms but also certain of their neighbors. A 1D example is shown in Fig. 1.7. As it is shown in Fig. 1.7B, the bond energy of the *ith* atom is $U_{tot} = U_{i-2,i-1} + U_{i-1,i} + U_{i,i+1} + U_{i+1,i+2}$. It is clear that the energy not only includes the interaction between the most adjacent atoms i-1 and i+1, *i.e.* $U_{i-1,i}$ and $U_{i,i+1}$, but also the

other two terms from effect of the two neighbors (atom i-2 and i+2). This nonlocal effect is not included in conventional FEM as the element in conventional FEM does not include the overlap shown above, *e.g.* element i shown in Fig. 1.7C does not have any information from the neighbor atoms i-2, i+1 and i+2.

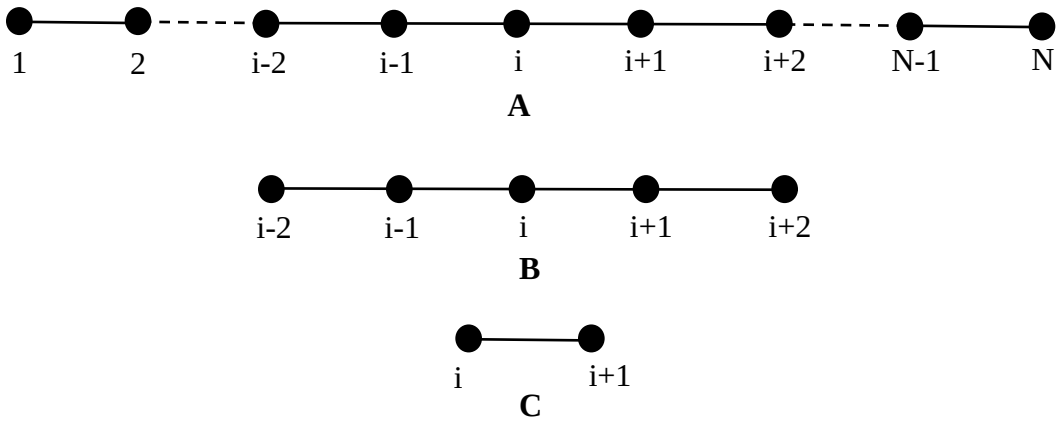

Fig. 1.7. Comparison of element definitions of conventional FEM and AFEM. (**A**) Global mesh with nodal number from 1 to N. (**B**) The *ith* element of AFEM with nodal number from i-2 to i+2. (**C**) The *ith* element of Conventional FEM with nodal number from i to i+1.

Although many differences exist between AFEM and conventional FEM, they share the same theoretical bases. Firstly, both of the methods discretize the complex global model into smaller and simpler pieces which is called "element". The element in AFEM, which is on micro-scale, contains all atoms which apply atomic interactions on central atom. All atoms and the atomic energy bonds connecting them form AFEM element. The element in conventional FEM, which is on macro-scale, contains all nodes

in the smaller continuum pieces partitioned from global continuum model. Secondly, the derivations of the general formulas for the two methods are based on variational method and the minimization of total potential energy. In what follows, the general derivation process of AFEM will be shown. By comparison of the content here and the one shown in the last chapter for conventional FEM, the similarities between the two numerical methods will be introduced.

The first step for the derivation is to build the function of total potential energy. It is consisted of two parts. One is internal energy (in this case atomic bond energy) and the other is external energy (in this case concentrated force applied on atom). Therefore, the total energy can be written as:

$$\Pi = W_{\text{int}} - W_{ext} = W_{\text{int}}\left(\mathbf{x}\right) - \sum_{i=1}^{N} \mathbf{F}_i \cdot \mathbf{x}_i \tag{29}$$

where $W_{\text{int}} = W_{\text{int}}\left(\mathbf{x}\right)$ is the internal energy due to the multi-body interaction from the atomic bonds. $W_{ext} = W_{\text{int}}\left(\mathbf{x}\right) - \sum_{i=1}^{N} \mathbf{F}_i \cdot \mathbf{x}_i$ is the external energy due to the concentrated forces $\mathbf{F}_i$ (if any) applied on atoms, $\mathbf{x}$ is the coordinate vector of all the atoms, N is the total number of atom in the system. Π is the total potential energy. As stated in the minimum of total potential energy discussed in the last chapter, the equilibrium of a system is obtained if the kinematically admissible deformation of the system enables the total potential energy of the system reaches its stationary point. So, the following can be obtained:

$$\delta\Pi = \delta W_{\text{int}} - \delta W_{ext} = \frac{\partial W_{\text{int}}\left(\mathbf{x}\right)}{\partial \mathbf{x}} \delta\mathbf{x} - \sum_{i=1}^{N} \mathbf{F}_i \cdot \delta\mathbf{x}_i = 0 \tag{30}$$

Since the variation $\delta\mathbf{x}$ is arbitrary, the following can be obtained:

$$\frac{\partial \Pi(\mathbf{x})}{\partial \mathbf{x}} = 0 \tag{31}$$

The PDE above, similarly as discussed in the last section, is usually impossible to be solved analytically. In order to obtain the solution, numerical method should be applied so that an approximate solution can be obtained. Again, linearization is applied on the PDE so that the obtained linearized (or approximated) equation can be readily solved by computer. In order to linearize the PDE, again the Tylor series expansion is applied at $\mathbf{x}^{(0)}$, which is the position of the atom at last time step.

$$\Pi(\mathbf{x}) \doteq \Pi(\mathbf{x}^{(0)}) + \left.\frac{\partial \Pi}{\partial \mathbf{x}}\right|_{\mathbf{x}=\mathbf{x}^{(0)}} \cdot (\mathbf{x}-\mathbf{x}^{(0)}) + \frac{1}{2}(\mathbf{x}-\mathbf{x}^{(0)})^T \cdot \left.\frac{\partial^2 \Pi}{\partial \mathbf{x}\partial \mathbf{x}}\right|_{\mathbf{x}=\mathbf{x}^{(0)}} \cdot (\mathbf{x}-\mathbf{x}^{(0)}) \tag{32}$$

Substitute the expression of $\Pi(\mathbf{x})$ to $\frac{\partial \Pi(\mathbf{x})}{\partial \mathbf{x}} = 0$, the PDE can be linearized. Then, similarly as done in the last section for conventional FEM, the concept of displacement can be introduced as $\mathbf{u} = \mathbf{x} - \mathbf{x}^{(0)}$, stiffness matrix as $\mathbf{K} = \left.\frac{\partial^2 \Pi}{\partial \mathbf{x}\partial \mathbf{x}}\right|_{\mathbf{x}=\mathbf{x}^{(0)}} = \left.\frac{\partial^2 W_{\text{int}}}{\partial \mathbf{x}\partial \mathbf{x}}\right|_{\mathbf{x}=\mathbf{x}^{(0)}}$, reaction force as $\mathbf{P} = -\left.\frac{\partial \Pi}{\partial \mathbf{x}}\right|_{\mathbf{x}=\mathbf{x}^{(0)}} = \mathbf{F}_i - \left.\frac{\partial W_{\text{int}}(\mathbf{x})}{\partial \mathbf{x}}\right|_{\mathbf{x}=\mathbf{x}^{(0)}}$.

After all the linearization, the final expression to be solved by computer can be shown as:

$$\mathbf{KU} = \mathbf{P} \tag{33}$$

which no matter on its form or on its physical meaning is almost the same as the final formula for conventional FEM shown in the last section.

1.4.2. Relation between Atomic-scale Finite Element Method and Nonlocal Finite Element Method

Nonlocal effect also exists in origami due to its special structure, *i.e.* multiple dihedral angles between adjacent faces are connected to form a network. In order to capture the nonlocal effect of origami, nonlocal finite element method (NFEM) is built. The only difference between the NFEM and AFEM discussed in the last section is on the definition of element. In AFEM, element is made of atoms as nodes and atom bounds as connection of the nodes. In NFEM, however, element is made of vertexes where multiple creases meet as nodes and dihedral angles between adjacent faces (the face is normally flat with vertexes as its corners) to connect vertexes. The total energy of an element in AFEM is assumed to be stored in atom bounds. It is a function of the length of the bounds. The energy in NFEM for origami is assumed to be stored in the artificial rotational spring mounted in any two adjacent faces connected by a crease. The spring is used to give stiffness to the two faces when there is a relative motion between them. Therefore, the total energy of an element in NFEM is a function of the dihedral angle of the two faces. Besides that difference, the rest of the two methods are the same.

CHAPTER 2 : SINGLE DEGREE OF FREEDOM RIGID ORIGAMI: MIURA-ORI—ANALYTICAL SOLUTION OF POISSON'S RATIO

From this chapter to Chapter 7, details of the projects for the study of origami and kirigami based structures will be presented. This chapter includes detailed study for the Poisson's ratio of an origami pattern called Miura-ori, which is the simplest and, at the same, probably the most well-known origami pattern. By introducing a complete list of design parameters, general Miura-ori pattern can be studied. The non-periodic feature of Miura-ori, which has long been ignored, is included in the calculation. Analytical solutions for out-of-plane and in-plane Poisson's ratio of the general Miura-ori pattern can be obtained. Finally, from the obtained results, the in-plane Poisson's ratio of Miura-ori, which has long been believed to always negative is shown can also be positive. Corresponding geometrical explanation of the interesting phenomenon will also be given.

Unit cell and the whole pattern of a Miura-ori are shown in Fig. 2.1, A and B, respectively. Fig. 2.1A illustrates a Miura-ori (n_1, n_2) in its folded state, containing n_1 vertices in x_1 direction and n_2 vertices in x_2 direction, with x_3 as the out-of-plane direction. The geometry of a Miura-ori is defined by many identical rigid parallelogram faces linked by edges that can be folded into ''mountain'' and ''valley'' creases. In Fig. 2.1B, four parallelograms are identical with the short sides of length a , the long sides of length b , and the acute angle $\beta \in \left[0^\circ, 90^\circ\right]$.

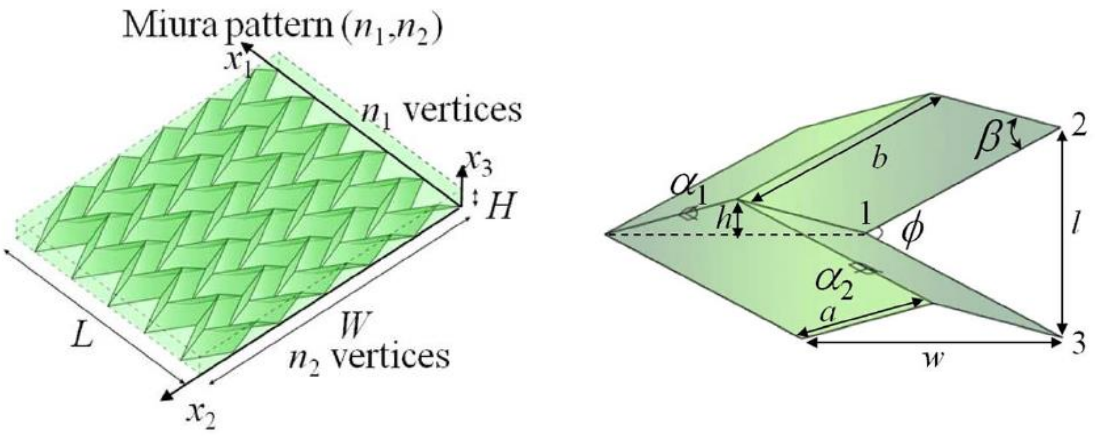

A **B**

Fig. 2.1. Geometry of Miura-ori pattern[1]. (**A**) The whole pattern with $n_1 = 11$ vertices on x_1 direction and $n_2 = 11$ vertices on x_2 direction, $\beta = 45^\circ$, $a/b = 1/\sqrt{2}$. (**B**) A unit cell of Miura-ori. α_1 and α_2 are two dihedral angles.

Since the necessary condition for rigid origami states that there are $n-3$ degrees of freedom, where n is the number of edges at one vertex[38,39]. Miura-ori with $n = 4$ has only one degree of freedom. Therefore, if the shape of a parallelogram face is prescribed, *i.e.* a, b and β are given, one parameter $\beta \in [0^\circ, 2\beta]$, the projection angle between two ridges, can be used to characterize the folding of the unit cell of Miura-ori, with $\phi = 2\beta$ for the planar state and $\phi = 0^\circ$ for the completely collapsed state. The size of the unit cell is $l = 2b\sin(\phi/2)$, $w = 2a\dfrac{\cos\beta}{\cos(\phi/2)}$ and $h = \dfrac{a\sqrt{\sin^2\beta - \sin^2(\phi/2)}}{\cos(\phi/2)}$, in x_1, x_2 and x_3

directions, respectively. It is noted that the length of the "tail" $b\cos(\phi/2)$ is normally not considered in the unit cell. The periodicity of this pattern only requires two dihedral angles $\alpha_1 \in [0^\circ, 180^\circ]$ and $\alpha_2 \in [0^\circ, 180^\circ]$ to characterize the geometry (Fig. 2.1B), which are given by:

$$\alpha_1 = \cos^{-1}\left[1 - 2\frac{\sin^2(\phi/2)}{\sin^2\beta}\right] \tag{34}$$

$$\alpha_2 = \cos^{-1}\left[1 - 2\cot^2\beta\tan^2(\phi/2)\right] \tag{35}$$

and equal 180° for the planar state and 0° for the completely collapsed state. When the whole structure of a Miura-ori is put in an imaginary box with the dashed lines as the boundaries (Fig. 2.1A), the dimension of the whole Miura-ori is then given by:

$$L = \frac{n_1 - 1}{2} l = (n_1 - 1) b \sin(\phi/2) \tag{36}$$

$$W = \frac{(n_2 - 1)}{2} w + b\cos(\phi/2) = (n_2 - 1) a \frac{\cos\beta}{\cos(\phi/2)} + b\cos(\phi/2) \tag{37}$$

$$H = h = \frac{a\sqrt{\sin^2\beta - \sin^2(\phi/2)}}{\cos(\phi/2)} \tag{38}$$

and thus the imaginary volume occupied by this Miura-ori is given by:

$$V = L \times W \times H \tag{39}$$

Apparently even the Miura-ori is periodic, its size in x_2 direction (i.e. W) is not proportional to its counterpart for the unit cell, w, due to the existence of the ''tail'' with length $b\cos(\phi/2)$. Consequently, it is not accurate to use the unit cell to study the size change of a whole Miura-ori (*e.g.*, Poisson's ratio), particularly for smaller patterns[36,40].

In-plane Poisson's ratio of Miura-ori is believed to be negative from intuitive observations and as testified by some theoretical studies using the unit cell[36,40] (Fig. 2.1B). An accurate mean to define the Poisson's ratio is to use the size of whole Miura-ori, i.e. L, W and H, instead of using that of unit cell, i.e. l, w and h. Specifically, the in-plane Poisson's ratio ε_{12} is defined as $\nu_{12} = -\left.\dfrac{\varepsilon_{11}}{\varepsilon_{22}}\right|_{\varepsilon_{22}\to 0}$, where $\varepsilon_{11} = \dfrac{dL}{L}$ and $\varepsilon_{22} = \dfrac{dW}{W}$ are the infinitesimal strains in x_1- and x_2-directions, respectively. Using equation (36) to (38), the in-plane Poisson's ratio ν_{12} is obtained as:

$$\nu_{12} = -\cot^2(\phi/2)\frac{(n_2-1)\eta\cos\beta + \cos^2(\phi/2)}{(n_2-1)\eta\cos\beta - \cos^2(\phi/2)} \tag{40}$$

where $\eta = a/b$. Another in-plane Poisson's ratio ν_{21} is just the reciprocal of ν_{12}. Similarly, the analytical expressions of out-of-plane Poisson's ratio can be obtained as:

$$\nu_{13} = -\left.\frac{\varepsilon_{11}}{\varepsilon_{33}}\right|_{\varepsilon_{33}\to 0} = \frac{\cot^2(\phi/2)\left[\sin^2\beta - \sin^2(\phi/2)\right]}{\cos^2\beta} \tag{41}$$

$$\nu_{23} = -\left.\frac{\varepsilon_{22}}{\varepsilon_{33}}\right|_{\varepsilon_{33}\to 0} = \frac{\left[\sin^2\beta - \sin^2(\phi/2)\right]\left[(n_2-1)\eta\cos\beta - \cos^2(\phi/2)\right]}{\cos^2\beta\left[(n_2-1)\eta\cos\beta + \cos^2(\phi/2)\right]} \tag{42}$$

where $\varepsilon_{33} = \dfrac{dH}{H}$ is the strain in x_3-direction.

For in-plane Poisson's ratio, as shown in Fig. 2.2A, the contour of ν_{12} as a function of angle ϕ and a combination parameter $(n_2-1)\eta\cos\beta$. The combination parameter can be completely determined after the creation of the crease pattern. Therefore, after the design of the pattern, only ϕ is needed when calculating the Poisson's ratio. Clearly, ν_{12} can be negative or positive, which is different from commonly

observed negative in-plane Poisson's ratio. The boundary separating the negative and positive regimes of ν_{12} is defined by vanishing the denominator of ν_{12}, *i.e.*, $(n_2-1)\eta\cos\beta=\cos^2(\phi/2)$. At this boundary, ν_{12} flips between positive and negative infinities; thus $\nu_{12}\in[-\infty,+\infty]$.

In addition to the negative and positive in-plane Poisson's ratio of the Miura-ori, the ranges of out-of-plane Poisson's ratios, as shown in Fig. 2.2, B and C, *i.e.* $\nu_{13}\in[0,\infty]$, $\nu_{23}\in[-\infty,\infty]$, are also fascinating if the range of Poisson's ratio for common materials is considered as the reference, *i.e.*, $\nu\in[-1,0.5]$. For ν_{23}, the same boundary, *i.e.* $(n_2-1)\eta\cos\beta=\cos^2(\phi/2)$ to separate the negative and positive value of Poisson's ratio also exist. In the application of Miura-ori, the sudden change of the Poisson's ratio can be used or avoided by using the contour plot. The contour plot here can be used as guidance for the design of Miura-ori for the interaction between the motions on any two perpendicular directions.

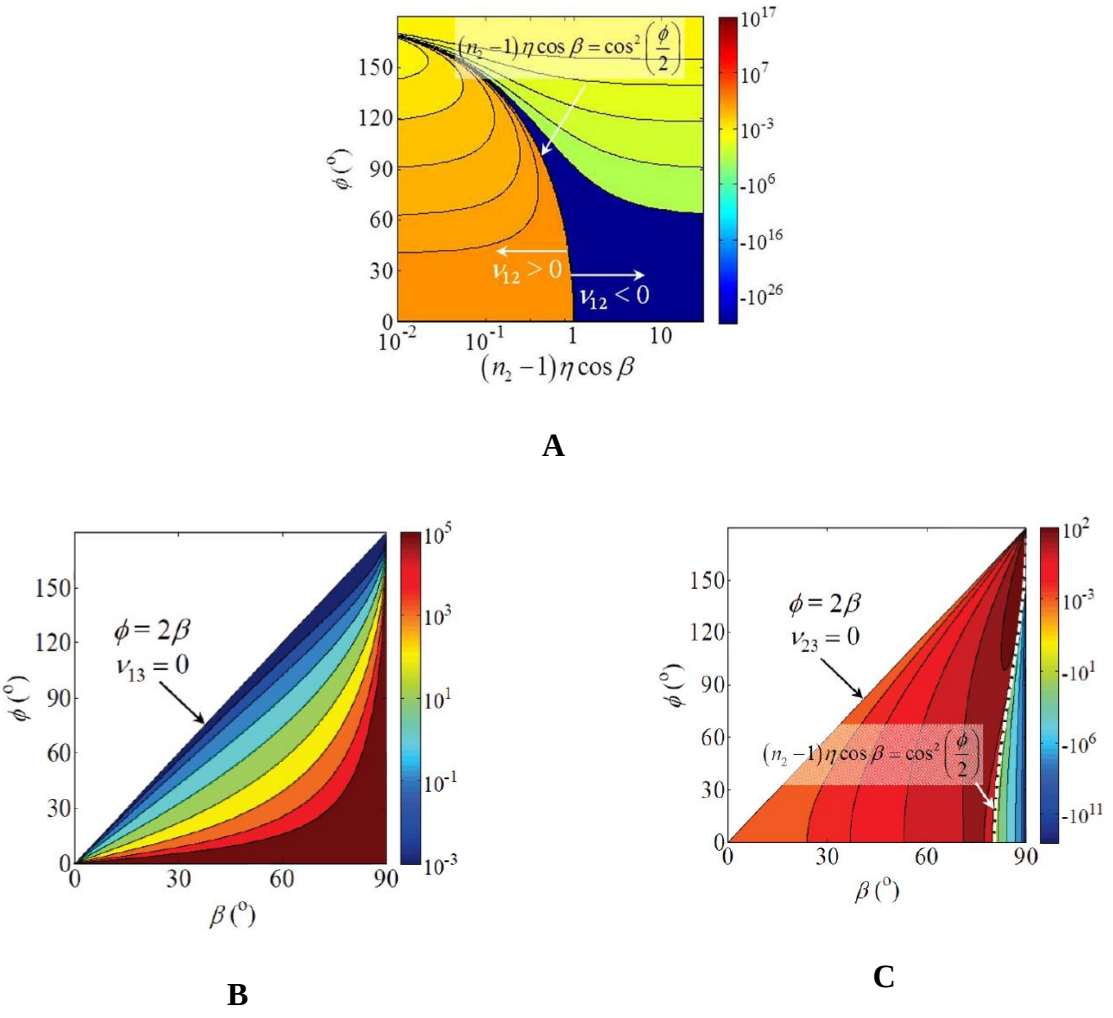

Fig. 2.2. Contour plot of Poisson's ratio of Miura-ori [33]. (**A**) Contour plot of in-plane Poisson's ratio ν_{12} as a function of ϕ and combination parameter $(n_2-1)\eta\cos\beta$. (**B**) Contour plot of out-of-plane Poisson's ratio ν_{13} as a function of ϕ and β. (**C**) Contour plot of out-of-plane Poisson's ratio ν_{23} as a function of ϕ and β.

Fig. 2.3 provides an intuitive explanation of the sign change in the in-plane Poisson's ratio ν_{12}. For the specific example with $n_1 = n_2 = 5$, $\eta = 1/2$ and $\beta = 78.5^\circ$, the size of this Miura pattern in x_1 direction, *L*, decreases monotonically from the planar state to the collapsed state, which is pictorially shown in the three insets for $\phi = 157^\circ \left(= 2\beta\right)$, $\phi = 140^\circ$, and $\phi = 20^\circ$ with $L_1 > L_2 > L_3$. In contrast to *L*, the respective size of this pattern in the x_2 direction, *W*, does not change monotonically with the angle ϕ. As shown in Fig. 2.3A, from the planar state to the collapsed state, $W_1 > W_2$ but $W_2 < W_3$, which gives $\nu_{12} < 0$ when *L* and *W* change in the same direction and $\nu_{12} > 0$ when *L* and *W* change in the opposite direction. The non-monotonic change of *W* is due to the "tail" term $b\cos\left(\phi/2\right)$ in equation (37), which was missed in previous studies[36,40]. Fig. 2.3B shows the derivatives of *W*'s two terms, *i.e.*, $\frac{\partial}{\partial\phi}\left[\left(n_2 - 1\right)\eta\frac{\cos\beta}{\cos\left(\phi/2\right)}\right]$ and $-\frac{\partial\left[\cos\left(\phi/2\right)\right]}{\partial\phi}$, along with *W*, as a function of ϕ, for $n_1 = n_2 = 5$, $\eta = 1/2$ and $\beta = 78.5^\circ$, the same parameters used in Fig. 2.3A. It can be seem that these two derivatives work against each other with $\frac{\partial}{\partial\phi}\left[\left(n_2 - 1\right)\eta\frac{\cos\beta}{\cos\left(\phi/2\right)}\right] > 0$ to decrease *W*, while with $\frac{\partial\left[\cos\left(\phi/2\right)\right]}{\partial\phi} < 0$ to increase *W*, from a planar state to a collapsed state. Therefore, the one among these two derivatives with larger absolute value dominates the change of *W*. It is apparent that when one folds a Miura-ori from its planar state to a collapsed state, $\frac{\partial}{\partial\phi}\left[\left(n_2 - 1\right)\eta\frac{\cos\beta}{\cos\left(\phi/2\right)}\right] > 0$ dominates firstly to decrease *W*. Once the stationary point is reached, $\frac{\partial\left[\cos\left(\phi/2\right)\right]}{\partial\phi} < 0$ starts to dominate and increase *W*.

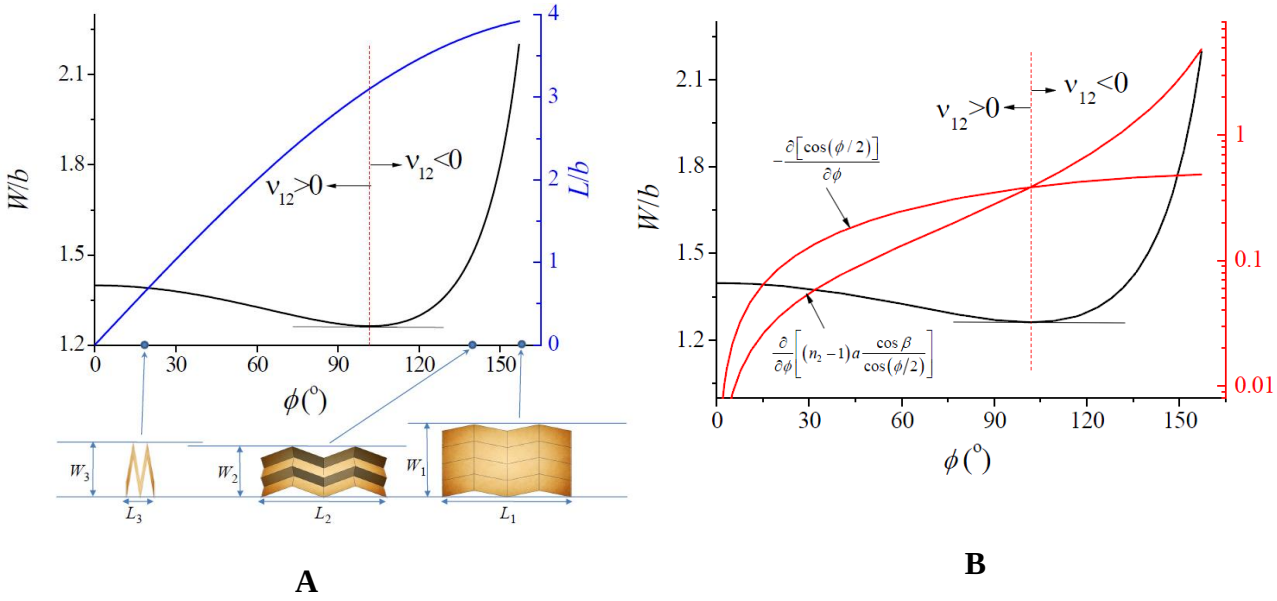

Fig. 2.3. Mathematical Explanation of negative and positive in-plane Poisson's ratio ν_{12} **[1].** (**A**) Change of W and L with ϕ. The three representative configurations during the folding process are shown as the visual explanation. (**B**) Change of size W with ϕ. Here the change rate of W's two terms with respective to ϕ is also shown.

CHAPTER 3 : MULTI-DEGREE OF FREEDOM RIGID ORIGAMI: WATER BOMB—NUMERICAL ANALYSIS BY NONLOCAL FINITE ELEMENT METHOD

After the study for relative simple rigid origami pattern shown in last chapter (Chapter 2), the content in this chapter will cover the analysis of a relative complex rigid origami pattern called water bomb. Nonlocal finite element method (NFEM) is used to capture the nonlocal effect during the deformation of water bomb structure under complex boundary conditions. Details for application of the basic NFEM theory (See details in Section 1.4) on water bomb pattern are shown. Finally, by the comparison between the results from numerical simulation and the ones from experiment, the accuracy of NFEM is validated. The current method can be readily used to study a variety of origami pattern.

NFEM is applied here to model the non-local effect of origami due to the interaction between the adjacent rigid faces. For rigid origami, all the degree of freedom is the rotational movement of flat faces along the creases which connect them. All the faces are treated as rigid in the whole simulation process. The NFEM applied in the analysis is origin from the atomic–scale finite element method[2] (AFEM), in which the pair interatomic potential is considered to represent the interaction between adjacent atoms. In the non-local finite element developed for rigid origami, the rotational stiffness is analog to the atomic bond potential in AFEM. Since NFEM is different from conventional FEM on the fact that existence of the overlap on the definition of the element in NFEM will not appear in conventional FEM. The introduction of the overlap enables the interaction between the adjacent elements. For water bomb pattern, two types of element exist. One is the non-local element which account for the non-local interaction

between adjacent nodes and the other is the spring element to ensure the rigidity of the creases during the whole calculation.

The requirement of this non-local element is that the non-local interaction must be completely captured within a single element. Using water bomb pattern as an example (Fig. 3.1), because the blue vertex affects its surrounding 12 red vertices, a non-local element is just defined by these 13 vertices with the blue vertex as the center (Fig. 3.1). This non-local element focuses on the central vertex to characterize its full interactions with neighboring vertices. Within this single element, the non-local effect is thus completely captured. Another non-local element centering on another vertex has the same structure as that of the blue vertex, and therefore these two neighboring non-local elements overlap in space. In fact, this overlap enables accurate characterization of the non-local effect for origami within a single element since it does not involve any interpolation as in conventional finite element method. By observation, two sorts of element exist due to their different connection of nodes. The global crease pattern and two kinds of the unit cells are shown in Fig. 3.1. All the vertices of the unit cell are numbered from 1 to 13 with the central node numbered as 1. The dash lines represent valley creases (creases move away from people) while the solid lines represent mountain ones (creases move toward people)

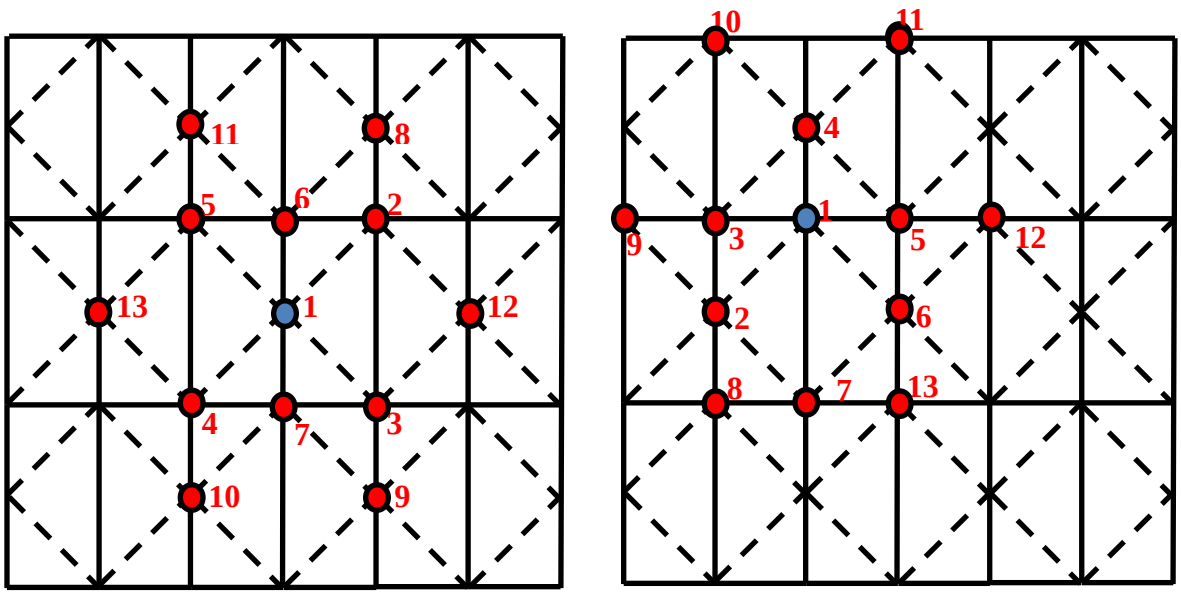

A **B**

Fig. 3.1. Crease pattern of Water bomb with nodal number of non-local elements. (**A**) Type I non-local element with No. 1 node as the central node. (**B**) Type II non-local element with No. 1 node as the central node. Here, the dash lines represent valley creases (creases move away from people) while the solid lines represent mountain ones (creases move toward people). The blue dot stands for the central node while the red nodes are its neighbor nodes which are necessary to form a whole NFEM element.

After defining the basic element types, the total potential energy of one unit cell can be written as:

$$U_{total}(\mathbf{x}) = \sum_{i=1}^{T_n} \sum_{\alpha_i} \frac{1}{2} k_i^R \left(\alpha_i(\mathbf{x}) - \alpha_{i,eq} \right)^2 - \sum_{i=1}^{N} R_i x_i \tag{43}$$

where k_i^R are the stiffness constants of the dihedral angles α_i with $\alpha_{i,eq}$ as the equilibrium angle, the superscript R stands for the rotational stiffness of the element and

T_n is the number of types of dihedral angles. Note here, dihedral angle α_i is a function of the position of the nodes $\mathbf{x}$, while $\alpha_{i,eq}$ is a constant set by the user initially. R is the external applied force (if any) on node i. N is the total number of the node. For the calculation of $\alpha_i(\mathbf{x})$ and its related derivatives $\frac{\partial \alpha}{\partial x_i}$, $\frac{\partial^2 \alpha}{\partial x_i \partial x_j}$, an generic and efficient method based on vector product is proposed (See details in Appendix).

Then the reaction force vector and the stiffness matrix can be obtained in the way similar to the ones in AFEM[2]:

$$\begin{aligned} K_{ij} &= \left.\frac{\partial^2 U_{total}}{\partial x_i \partial x_j}\right|_{\mathbf{x}={}^t\mathbf{x}} \\ F_i &= -\left.\frac{\partial U_{total}}{\partial x_i}\right|_{\mathbf{x}={}^t\mathbf{x}} \end{aligned} \tag{44}$$

here, ${}^t\mathbf{x}$ is the coordinate vector calculated at the last time step, K_{ij} is the interaction on stiffness between the ith and the jth node in the element, F_i is the nonequilibrium force on the ith node in the element.

In the current case, U_{total} is substituted into the above two general equations, the following can be obtained:

$$\begin{aligned} K_{ij} &= k^R \frac{\partial \alpha}{\partial x_i}\frac{\partial \alpha}{\partial x_j} + k^R\left(\alpha - \alpha_{eq}\right)\frac{\partial^2 \alpha}{\partial x_i \partial x_j} \\ F_i &= -k^R\left(\alpha - \alpha_{eq}\right)\frac{\partial \alpha}{\partial x_i} + R_i \end{aligned} \tag{45}$$

where, α is the dihedral angle which is a function of the corresponding coordinate x_i. If the expression of α in term of x_i can be obtained, the final expressions of K_{ij} and F_i can be obtained.

Detailed expressions of element stiffness matrix $\mathbf{K}$ and element nonequilibrium force vector can be shown as following:

$$\mathbf{K} = \begin{bmatrix} \left(\frac{\partial^2 U_{total}}{\partial \mathbf{x}_1 \partial \mathbf{x}_1}\right)_{3\times 3} & \frac{1}{2}\left(\frac{\partial^2 U_{total}}{\partial \mathbf{x}_1 \partial \mathbf{x}_i}\right)_{3\times 3(N-1)} \\ \frac{1}{2}\left(\frac{\partial^2 U_{total}}{\partial \mathbf{x}_i \partial \mathbf{x}_1}\right)_{3(N-1)\times 3} & (\mathbf{0})_{3(N-1)\times 3(N-1)} \end{bmatrix} \qquad (46)$$

$$\mathbf{F} = \begin{bmatrix} \left(\mathbf{R} - \frac{\partial U_{total}}{\partial \mathbf{x}_1}\right)_{3\times 1} \\ (\mathbf{0})_{3(N-1)\times 1} \end{bmatrix}$$

Note here, the terms in the lower right part of the stiffness matrix and in the lower part of nonequilibrium force vector are all zero. This is due to the fact that, as described before in this section, interactions between the neighboring nodes are ignored in every AFEM element. The $\frac{1}{2}$ factor before the terms on the upper right and lower left is added since the AFEM elements, which overlap with each other in their definitions, cannot double account the energy stored in dihedral angles. By defining the element in this general method, the assembly process can be much more comprehensive and also much easier.

For spring elements, relative high stiffness is used so that the deformation of them can be ignored compared to that of the non-local elements. The total potential energy of it is:

$$\frac{1}{2}k^L\left(r - r_0\right)^2 \qquad (47)$$

here, k^L is the stiffness of the linear spring elements. r and r_0 are the current and reference length of the linear spring elements. Then, by the similar method described above for non-local elements, the expressions of K_{ij} and F_i of linear spring elements can be written as:

$$\begin{aligned} K_{ij} &= k^L \frac{\partial r}{\partial x_i}\frac{\partial r}{\partial x_j} + k^L\left(r - r_0\right)\frac{\partial^2 r}{\partial x_i \partial x_j} \\ F_i &= -k^L\left(r - r_0\right)\frac{\partial r}{\partial x_i} \end{aligned} \tag{48}$$

For the FEA, commercial software ABAQUS, which is known for its accuracy on nonlinear FEA, is applied. Since applied load is considered slow enough, ABAQUS Standard static analysis is chosen. To implement the NFEM, a user developed subroutine called User-defined Element (UEL) is applied to define element properties of water bomb pattern. For the UEL, a user needs to define the residual vector RHS and stiffness matrix $AMATRX$. Note here, RHS is defined on the element level. So the term R_i, which is usually defined on the global level, in Equation (45) will be excluded, *i.e.* $RHS = -k\left(\alpha - \alpha_{eq}\right)\frac{\partial \alpha}{\partial x_i}$. $AMATRX$ just equals to the stiffness matrix K_{ij}. See the FORTRAN code for user subroutine of NFEM in Appendix E.

Since the problem is highly nonlinear, the stiffness matrix may become not positive definite, which is bad for the convergence of the numerical calculation. To ensure the positive definite of the stiffness matrix, an adjust factor is added. It will help the calculation to converge while not affect the accuracy of the final results. This is achieved as the factor will decrease when approaching the equilibrium state. Finally,

when the equilibrium is reached, the factor goes to zero, *i.e.* it has no effect on the final results.

Firstly a 2D pattern of water bomb is generated by using AutoCAD with the number of period on two in-plane directions to be 7 and 16, respectively. Instead of calculating the water bomb pattern from 2D sheet to the final 3D ball-shape, which requires a large amount of computational effort, an approximate configuration which is relative close to the final 3D ball-shape equilibrium configuration is firstly obtained as the intermediate configuration. This is achieved by using the Rigid Origami Simulator[41] with the 2D CAD file as the input. For the resulted obtained configuration, a big gap exists between two of edges of the model. It is only when the two edges exactly meet, the final water bomb configuration can be obtained. After that, one of the dihedral angles in the elements on the central layer of the water bomb is fixed to be 60° while the rest of angles are left free to change. At the same time, constraints of some linear spring elements along the creases are released, *i.e.* the change of the corresponding crease lengths are allowed. During the iteration of the numerical calculation, the constrains for the linear spring elements are gradually added back. Finally, all the constraints are added back to ensure the designated length of the creases pattern. A configuration is obtained which will be used in the next step as the initial undeformed geometry. All the dihedral angles in this configuration will be used as their corresponding equilibrium angles in the following analysis. The equilibrium state is shown in Fig. 3.2A.

After applying different loads, multiple configurations can be obtained. Fig. 3.2, B and C show two of the examples. The former is compression along axis direction and the latter is stretching.

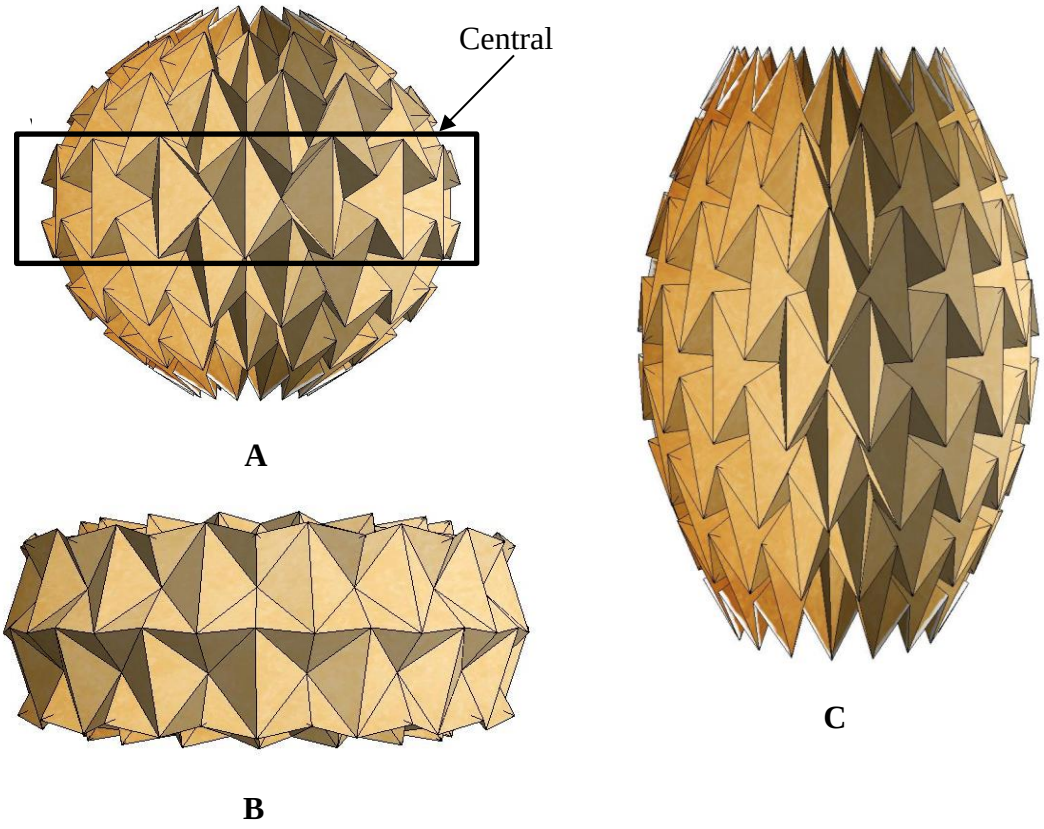

Fig. 3.2. FEA results of Water bomb under different mechanical loadings. (**A**) Equilibrium configuration of Water bomb. (**B**) Water bomb under axial compression. (**C**) Water bomb under axial stretch.

CHAPTER 4 : PLASTICITY AND LOCKING IN ORIGAMI

After the study of rigid origami shown in Chapter 2 and Chapter 3, my focus turns to the study of non-rigid origami based structures. Here, non-rigid means deformation of each individual face is allowed. In this chapter, plasticity, which has long been ignored by others, is included during the modelling of origami. The locking phenomenon, which means the origami based structure cannot recover its equilibrium state after releasing all the applied loadings, can be well captured by buckling analysis via FEA. Based on the final results from FEA and experiment, it is suggested here, plasticity should be included in the modelling of origami due to the existence of sharp creases in most of origami pattern.

In existing work on origami simulation, people often ignore the effect of plasticity in order to simplify the problem. It works for most of cases while very local behaviors cannot be captured. Here in order to model a phenomenon called “locking”, which is commonly observed in real non-rigid origami based structures, plasticity is introduced during the modelling process. Here, “locking” means the origami based structure will not go back to its equilibrium state after releasing all of the applied loads. Instead, it will stay in a quasi-stable state and appear as being “locked”.

Since large deformation and shell-structure will be included in the 3D analysis of origami based structure, difficulty on convergence of result will be an issue if implicit analysis is applied. Therefore, all implicit numerical methods which are commonly applied in FEM will not be appropriate. Based on the fact, explicit method will be applied. By taking advantage of explicit method, *i.e.* no iteration applied thus no convergence issue, final result will be efficiently obtained. Instead of using ABAQUS

Standard as people normally do, current simulation is done by using ABAQUS Explicit dynamic analysis. To simplify current analysis, inertial effect is excluded, *i.e.* quasi-static analysis was carried out. This is possible in ABAQUS Explicit dynamic analysis when user give relative long simulation time so that the inertial effect can be ignored. This can be easily checked by comparing the kinetic and strain energy of the whole model, *e.g.* if kinetic energy is much lower than strain energy it indicates the inertial effect is weak enough to be ignored.

Inspired by the locking phenomenon described in the last section, I decided to study the reason why it can happen. It should be noted that the locking happened during the study of rigid origami model is always be accompanied with relative large energy in linear spring, *i.e.* only with certain amount of breaking of the rigidity of the model can locking happen. Based on the observation, it is reasonable for me to consider non-rigid origami when studying locking phenomenon. In order to enable locking, plasticity should be introduced. The initial geometry of the paper-made origami based structure is shown in Fig. 4.1A and its corresponding numerical model is shown in Fig. 4.1B. Instead of making each face rigid as done in previous section, the whole model is now considered to be deformable. To simplify, the simplest plasticity model, linear plasticity model, was applied to the material of the whole model. Quasi-static analysis was carried out by using ABAQUS Explicit dynamic. Proper mass scaling was applied to make the simulation more efficient. The comparison of the kinetic energy and strain energy is shown in Fig. 4.2. It is clear that the kinetic energy is much lower than the strain energy, which indicates the inertial effect can be ignored and the simulation can be treated as quasi-

static. As shown in Fig. 4.1B, one end of the model is fixed while displacement boundary load is applied on the other.

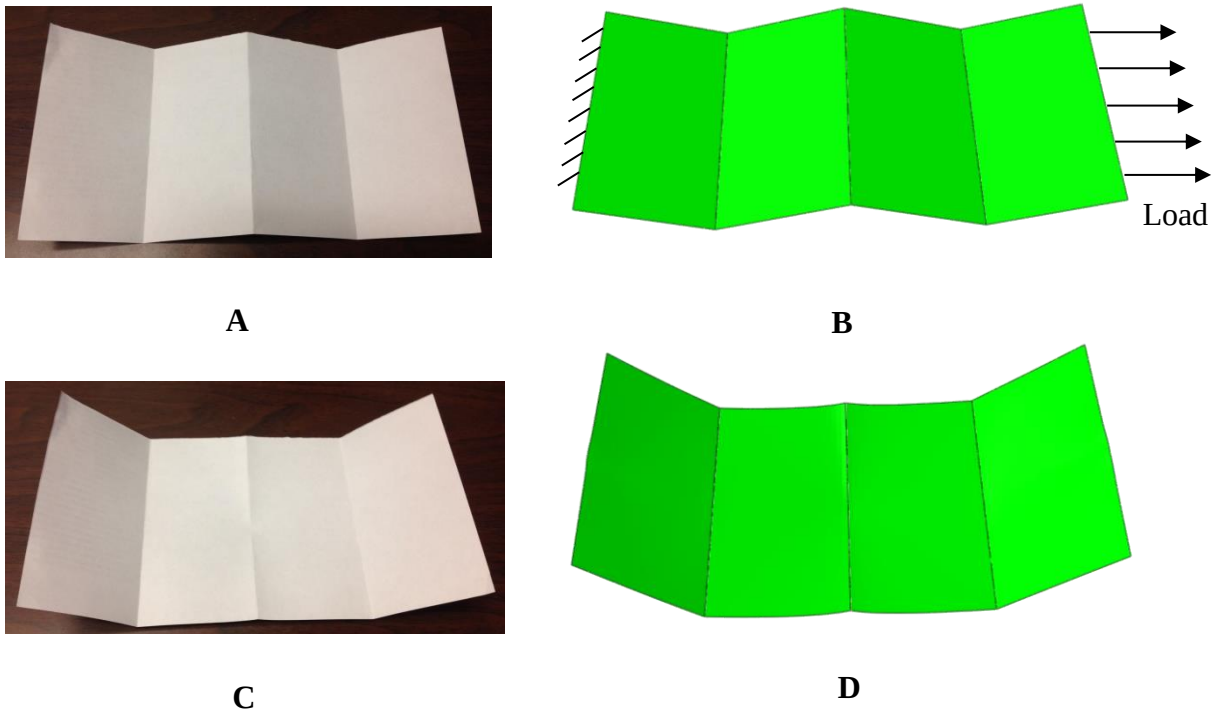

Fig. 4.1. Comparison of the experiment and simulation results. (**A**) Initial state of origami from experiment. (**B**) Initial state of origami from simulation. (**C**) Quasi-stable state of origami from experiment. (**D**) Quasi-stable state of origami from simulation. It can be seen here the results from experiment and from FEA are almost the same. This validates the accuracy of the introduction of plasticity into origami modelling.

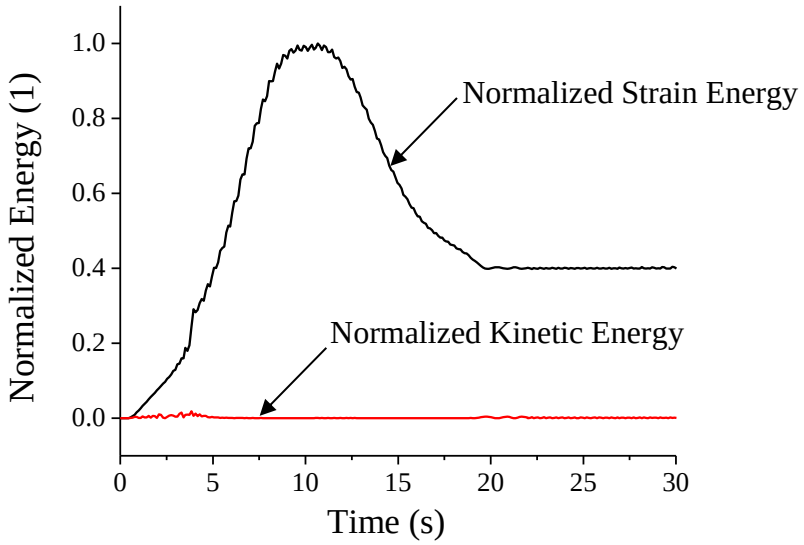

Fig. 4.2. Comparison of normalized kinetic energy and strain energy.

The initial and deformed structure from experiment and simulation is shown in Fig. 4.1. It can be found that no matter in initial state or in deformed state the resulted geometries are almost the same, which indicates introducing plasticity model is reasonable, *i.e.* the locking mechanism is a result of plasticity.

CHAPTER 5 : MICROSCALE ORIGAMI BASED STRUCTURES—FINITE ELEMENT ANALYSIS GUIDED DESIGN

After the study of macroscale origami based structures shown in Chapter 2, Chapter 3 and Chapter 4, I begin to focus of the study of micro scale origami based structures. In this chapter, a new method to fabricate microscale origami is proposed. This method is based on the buckling of thin-film which is bonded with predesigned walls on a soft substrate. Due to the fact that there is a large amount of design parameter, numerical simulation will be necessary. By using FEA as the tool for numerical analysis, the design and optimization of the wall patterns can be much more efficient. The results from experiment shown in this chapter further validate the FEA results, which indicates the accuracy of FEA. Please note I only design the manufacture process in this section. The actual physical experiments were done by Zeming Song. Some of the experiment results are shown here for the purpose to illustrate the basic idea and used to compare with my FEA results.

Although numerous effort has been paid on design and optimize buckling of ribbon-liked kirigami based structures (thin film structures involves cutting and folding) [42-47] to form 3D complex structures, few has even consider the buckling of origami based structures (thin film structures involves folding only). Here I demonstrate a new strategy to fabricate microscale origami using Si nanomembrances (NMs) as the materials which was previously impossible by using conventional fabrication methods. In the current approach, Si NMs are supported by elevated polydimethylsiloxane (PDMS) walls on top of a PDMS substrate. Thus the Si NMs are suspended. Upon relaxation of the pre-stretch applied on the PDMS substrates, the suspended Si NMs buckle with the pre-patterned

wall as the support and constraints to form designated microscale Si origami. Thus the final microscale origami patterns with 3D complex structures are controlled by the patterning of the elevated wall. Because the microscale characteristics of the origami architectures and the continuum feature of the NMs, the microscale origami may lead to multiple breakthroughs, such as in electromagnetics. Applications include microscale grating, thermal invisible device, and low observable (stealth) structures.

The methodology is illustrated in Fig. 5.1. An elastomeric substrate PDMS (Sylgard 184, Dow Corning) is mold cast to a shape with pre-patterned, elevated walls on top of a stab, followed by biaxial or uniaxial pre-stretch (from L to $L+\Delta L_1$ and $L+\Delta L_2$ along the two perpendicular in-plane directions), which can be achieved by mechanical means or heating. The characteristic sizes of the elevated walls are on the order of 10–200 μm. The pre-stretched PDMS is subjected to ultraviolet/ozone treatment in order to form activated hydroxyl groups for bonding. Because the PDMS walls are elevated, they thus provide selective bonding sites. Then a Si NM, derived from the device layer of a silicon-on-insulator (SOI) wafer, is brought to contact with the patterned PDMS. Specifically, the elevated PDMS walls provide supports to Si NM and thus Si NM is suspended. Because of the surface treatment, condensation reactions occur at room temperature between the elevated PDMS walls and the native oxide surfaces of Si NMs[25,48,49]. Si NMs then can be exfoliated from the SOI wafer and adhered to the elevated PDMS walls. Once the pre-stretch exceeds a certain critical level, relaxation of the pre-stretch suspended Si NMs enables its buckling and forms predesigned origami patterns. The buckling is the result of releasing the membrane energy through the out-of-plane deformation via mainly bending and sometime twisting. The resulted origami

patterns are defined by two factors: (1) the shape of the pre-patterned, elevated walls, and (2) the nature of pre-stretch (i.e., biaxial with different pre-stretches in two directions vs. equi-biaxial pre-stretch). The first factor determines the type of the origami and later tunes the patterns.

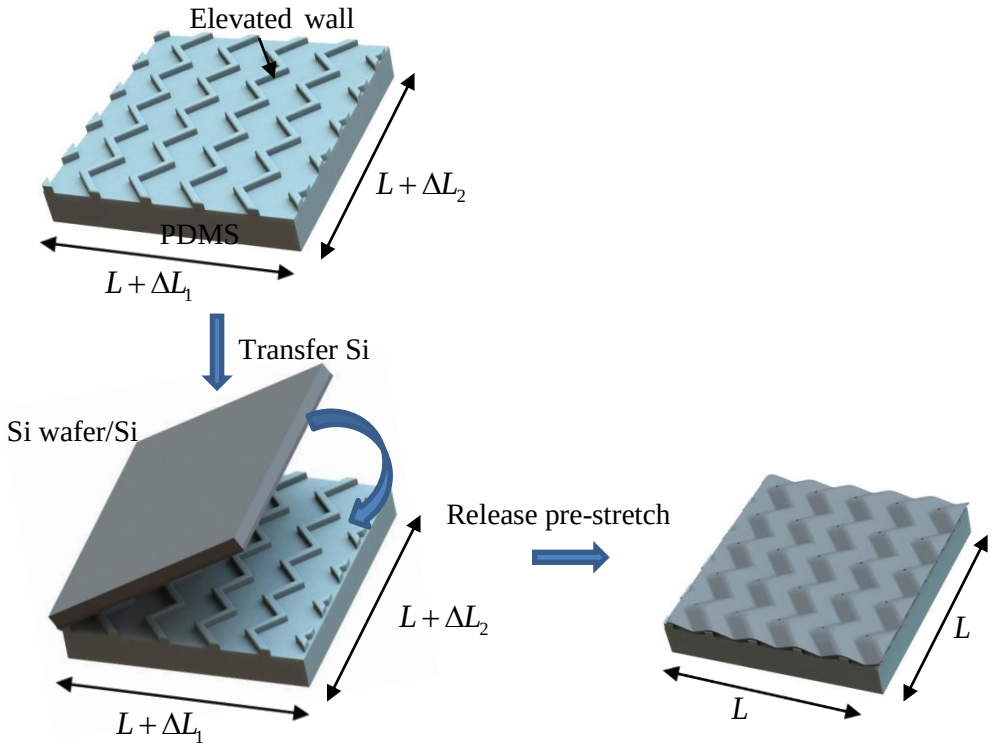

Fig. 5.1. Schematic illustration of using elevated PDMS walls to suspend Si NM and releasing the pre-stretch to generate designated microscale origami patterns[50]. Here the elevated PDMS walls have been pre-patterned for the Miura-ori pattern

The finite element analysis (FEA) was conducted using commercial finite element software package ABAQUS, and consists of two steps. The first step, mode analysis, or

pre-buckling analysis, is carried out by calculating the eigenvalues of the model under the given loads and boundary conditions. The loads applied are simply in-plane equi-biaxial compressions which are equivalent to the uniform shrinkage due to the uniform decrease of temperature of the whole model. After the calculation, possible buckling shapes can be obtained. Then the static analysis, or post-buckling analysis, can be carried out since the post-buckling process is slow enough to be regarded as quasi-static. Same loads as above are applied in this step. The buckling modes obtained from previous step can be added to the initial geometry as the imperfection to trigger the buckling of the model. Finally, the stress and strain distribution of the buckling model can be obtained.

As a specific example using the pre-patterned walls with shapes illustrated in Fig. 5.1, a Miura-ori pattern[51] can be obtained. Fig. 5.2A shows a photography of a Si NM Miura-ori pattern generated using this approach, where the thickness of the Si NM is 300 nm and the equi-biaxial pre-strain of 3.6% was introduced by heating the PDMS from room temperature to 120^{o}C. The detailed geometry of the pre-patterned PDMS wall is given in s Fig. A4, A and B. It is apparent that in a 2.2 mm $\times$ 2.2 mm area this Si NM Miura-ori pattern replicates the paper-based Miura-ori, given by the inset of Fig. 5.2A. The observable difference is that the sharp "mountain" creases in paper-based Miura-ori are replaced by the flat PDMS walls in the Si NM Miura-ori, because the downwards out-of-plane buckling occurs and the elevated PDMS walls actually serve as “mountain” supports for the Si NMs. The “valley” creases are not as sharp as paper-based pattern because of, as stated by the minimum total potential energy principle, much lower energy state of relative smooth crease is usually preferred by the deformed system. It is emphasized here that using this origami inspired methodology, a planar structure is

transferred to a 3D architecture across an entirely continuum film, rather than discretized ribbons[52]. Fig. 5.2B provides the optical profilometer images of the Si NM Miura-ori pattern. It is observed that the Si NM has apparent deformation at the vertices of the elevated wall (marked by the red triangle) in Fig. 5.2B, which suggests a localized and possibly large strain. To compare the experiments with calculated stress and strain during buckling, finite element analysis (FEA) was conducted. A unit cell of the Si NM is simulated in the FEA (Fig. A9, A and B give illustration of an ideal Miura-ori unit cell in Appendix G), which consists of four parallelograms. For simplicity, PDMS walls are not explicitly included and just implicitly appear as boundary conditions to the Si NMs. Using the equi-biaxial pre-strain of 3.6%, the FEA results (Fig. 5.3) show a simulated Miura-ori pattern with good agreement with that observed in experiments. The good alignment between FEA and experiments suggests that FEA can be utilized to design the origami patterned generated by buckling. FEA results show that the maximum principal strain 0.87% appears at the vertex of the "mountain" creases, which is less than the 1% fracture strain of single crystalline Si. Fig. 5.4, A, B and C show the line-cut comparison between the experiments, FEA results, and analytical expression of rigorous Miura-pattern. For Miura-ori pattern, the closed loop solution can be obtained (detailed in the Appendix G) because it has only one degree of freedom. Use n to denote the number of creases at one vertex and thus n =4 for Miura-ori. For ideally rigid origami (e.g., Miura-ori) where all facets are rigid and only the creases deform during folding, it is known that there are n-3 degrees of freedoms[38,53]; thus Miura-ori has only one degree of freedom. It is observed that the generated Si NM origami agrees reasonably well with both the analytical and FEA results. The major discrepancies occur at the "mountain" vertices

since the analytical solution and FEA results are based on zero size of creases while the experiments have finite size of the elevated PDMS walls.

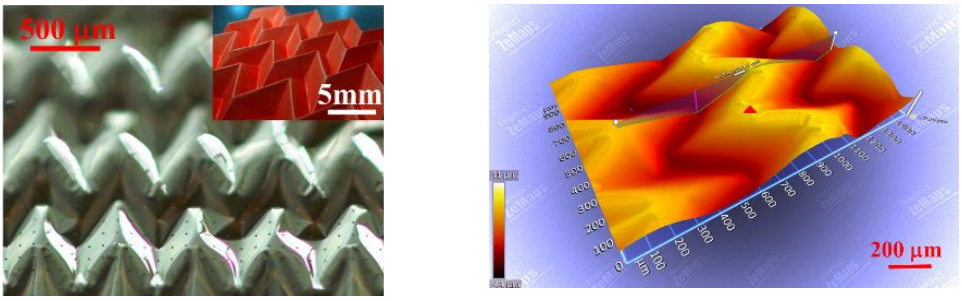

A **B**

Fig. 5.2. Silicon (Si) nanomembrane (NM) Miura-ori pattern obtained from physical experiment[50]. (**A**) A photography of a Si NM Miura-ori pattern. The inset shows a paper-based Miura-ori pattern for comparison. (**B**) An optical profilometer image shows the Si NM Miura-ori pattern. The line cut measurement was performed.

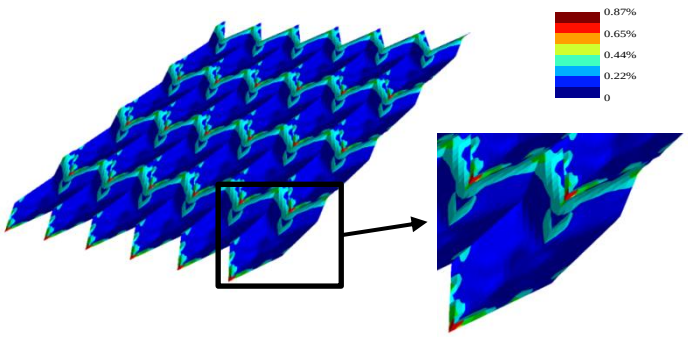

Fig. 5.3. Finite element analysis (FEA) results of Si NM Miura-ori pattern. The contour plot is for the principal strain of buckled Si NM[50].

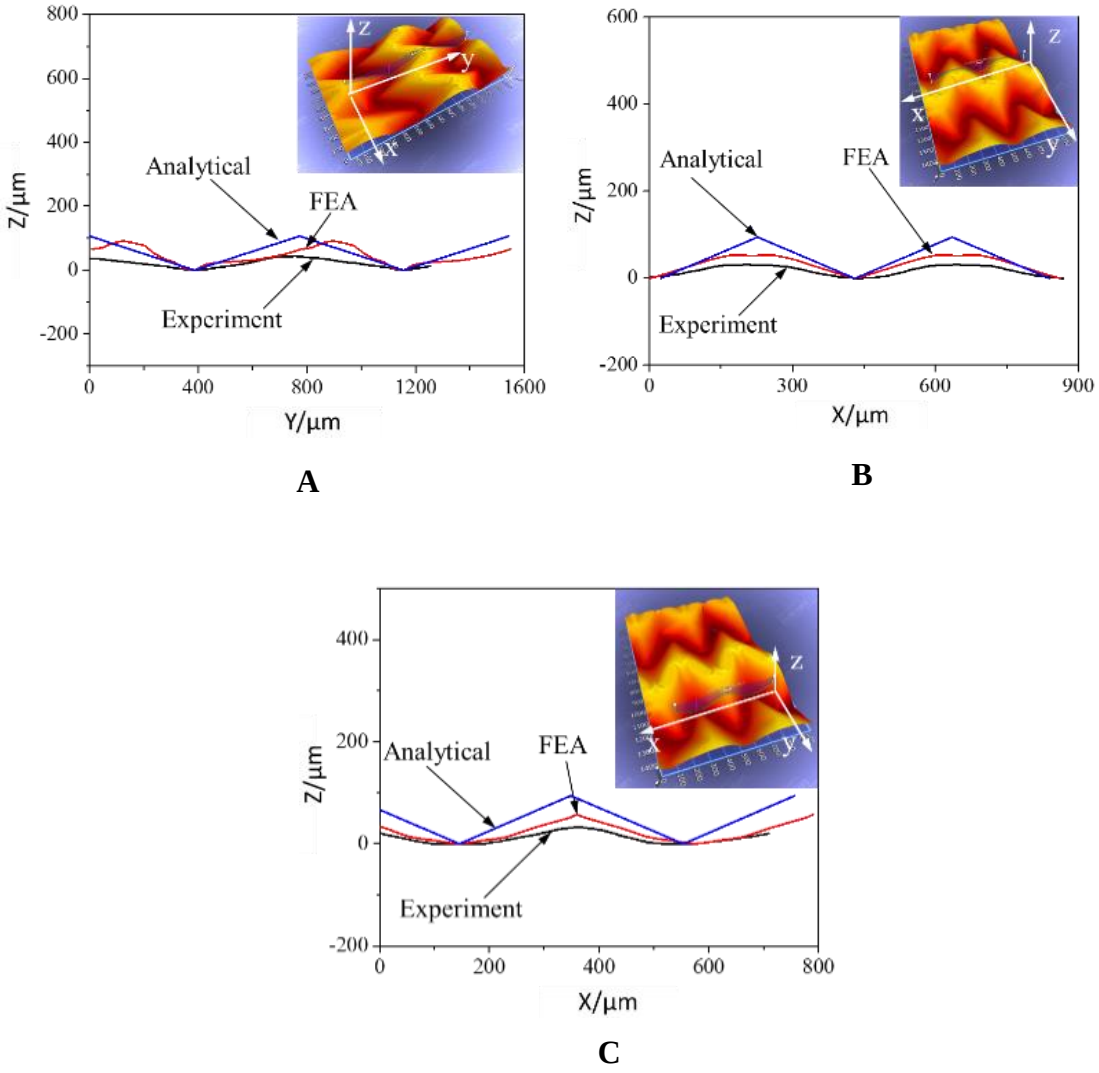

Fig. 5.4. Line cut comparisons between the experiment, FEA, and analytical solution. The inset shows an image of optical profilometer, in which the line cut profile was measured in experiment[50]. The measured directions are: (**A**) "mountain"-"valley"-"mountain" cut along y-direction, (**B**) along the mid-point of "mountain" creases, and (**C**) "mountain"-"valley"-"mountain" cut along x-direction.

Wide range and more complicated Si NM origami patterns can be realized, with the inspiration from the paper-based origami. The logic is to vary the shape of the elevated PDMS walls. As there are significant variations of paper-based origami, the first extension from Fig. 5.2A (Miura-ori with one degree of freedom) is an origami pattern with three degrees of freedoms. Fig. 5.5A shows a photography of a Si NM origami with water bomb pattern, or the nickname "magic ball" pattern, through the relaxation of equi-biaxial 3.6% pre-strain via thermal expansion of the PDMS. The detailed shape and geometry of the elevated PDMS walls to form this pattern are given in the Fig. A5, A and B. Great similarity is observed when compared with the paper-based "magic ball" pattern (inset of Fig. 5.5A). However, a discrepancy is also noticed and in fact related to the methodology of generating microscale origami using elevated PDMS walls. For ideal "magic ball" pattern (as detailed in the Appendix G), the "mountain" creases always form a curved geometry and cannot stay flat unless at the completed collapsed state, which is different from the Si NM origami (Fig. 5.5A) where the "mountain" creases (i.e., elevated PDMS walls) are on the flat state. The reason is that Si NM is not ideal rigid and facets are allowed to deform.

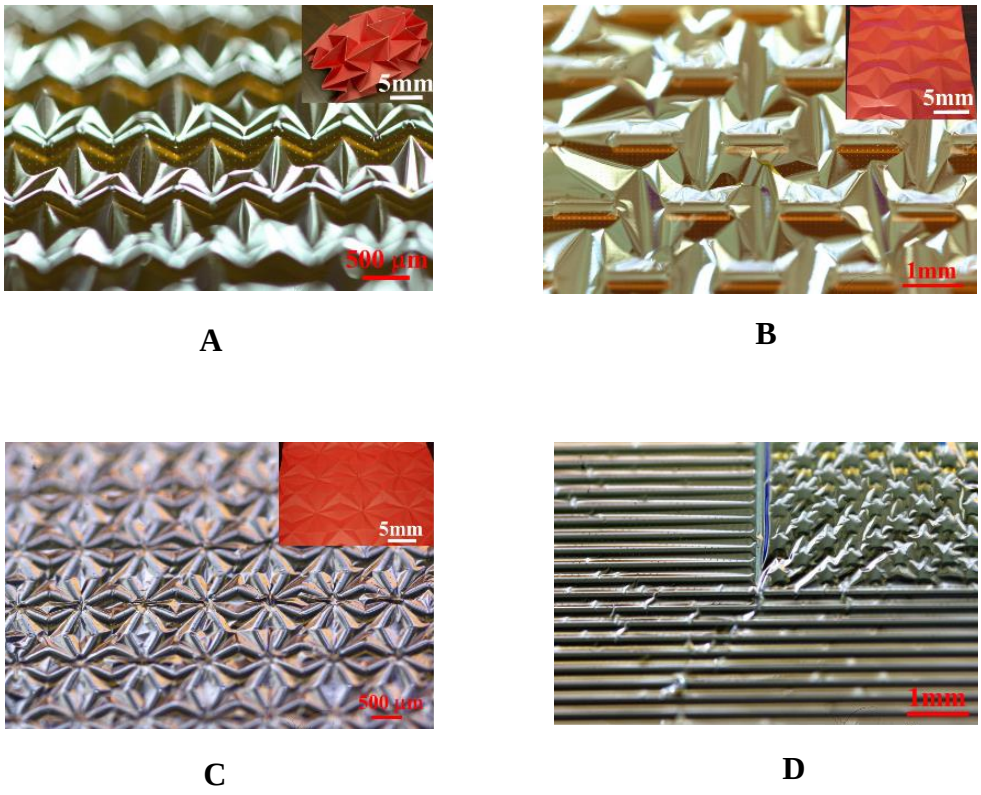

Fig. 5.5. Demonstration of other silicon (Si) nanomembrane (NM) origami patterns with different characteristics[50]. (**A**) A photography of a Si NM "magic ball" pattern. The inset shows a paper-based Miura-ori pattern for comparison. (**B**) A photography of a Si NM non-rigidly foldable pattern. (**C**) A photography of a Si NM star pattern. (**D**) A photography of a Si NM US Flag pattern.

Fig. 5.5B provide more Si NM origami patterns that, by theory[38,53], cannot be rigidly folded while can be achieved using the present methodology. Fig. 5.5B presents the photography of a non-rigidly foldable pattern using staggered PDMS walls given in the Fig. A6, A and B. Very sharp creases are observed. Related to this pattern that it is not rigid foldable at all vertices, some patterns are rigid foldable at the unit cell level but not at the assembled level, such as the star pattern shown in Fig. 5.5C. The shape and geometry of the PDMS walls are given in the Fig. A7, A and B. In this pattern, the unit cell is a star, which is rigid foldable. However, when two stars are assembled, their boundaries are not compatible. Composite and non-periodic patterns can be generated by combing multiply patterns, such as the mimicked US Flag shown in Fig. 5.5D consisting of stars and stripes. Detailed shape and geometry of US Flag pattern are given in the Fig. A7, A, B and C.

In this section, I report a new methodology to create 3D origami patterns out of Si NMs using pre-stretched and pre-patterned PDMS substrates. The key parameter here is the shape of the pre-patterned PDMS walls. This approach is complementary to a recent work that is able to achieve 2D origami shapes where the creases are pre-defined by cutting, i.e., the concept of kirigami[54,55]. We demonstrated that this approach is able to mimic paper-based origami patterns and even modifies the paper-based origami for some non-rigidly foldable structures. Though the demonstrations are based on Si NWs, richer materials, such as metal and composites can be adopted to generate complex 3D architectures. We believe that the combination of origami-based microscale 3D architectures and antenna will lead to a breakthrough on physically and geometrically reconfigurable systems.

CHAPTER 6 : FAILURE ANALYSIS OF KIRIGAMI LITHIUM-ION BATTERIES CONSIDERING USING FEA

After the study of origami based structures (details shown from Chapter 2 to Chapter 5), the kirigami based structures, which involves more degree of freedom, will be studied. In this chapter, the failure mechanisms of kirigami based lithium-ion battery will be introduced. As cutting is necessary for fabrication of kirigami based structures, initial crack cannot be avoided. Plasticity is another issue if sharp crease is introduced during folding of the structure. So, the deformation of kirigami based structures will be coupled with the competition of the two mechanisms. The one which costs lower energy will be preferred the structure. By using FEA and classical theories, different geometry can be test so that the one with robust structure can be obtained.

Simulation is done by using ABAQUS and a simplified model is shown in Fig. 6.1, where two pre-existing cracks are presumably caused by initial folding and/or cutting and located at the present positions when a pair of concentrated moment M is applied at the end of the strip with length L and width H. The concentrated moment M is used to characterize the applied stretching deformation that causes bending about the folding creases. Angle θ is used to denote the relative positions of two strips with $\theta = 0$ for the initial folded position. When the moment M is applied, there exist two modes of deformation. The first mode causes the growth of the pre-existing cracks from a to $a + \Delta a$, while maintaining the angle θ unchanged, which refers as "crack growth". The second mode leads to plastic deformation of the thin foil at the vicinity of the fold by altering θ to $\theta + \Delta\theta$, which is referred to as "plastic rolling".

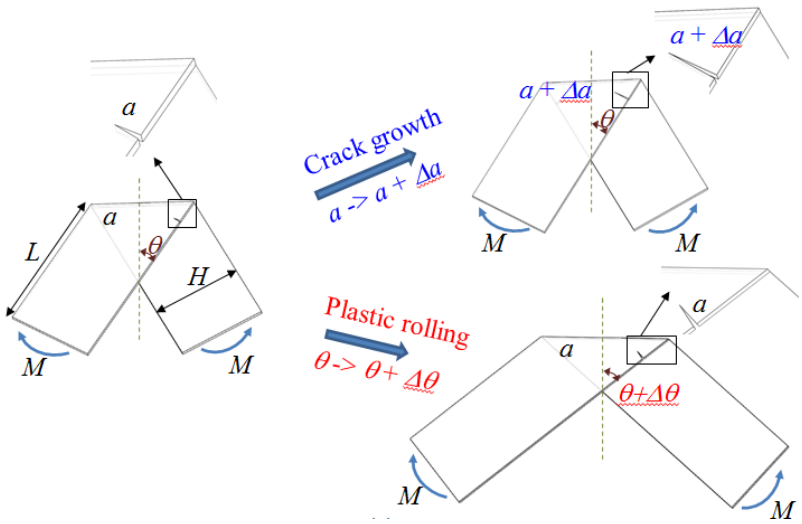

Fig. 6.1. Introduction of the deformation mechanisms[3]. The crack growth introduces the extension of the crack length a while the plastic rolling introduce nothing but normal folding process.

The critical condition for "crack growth" is given by the modified Griffith's criterion for linear elastic material[56]. Griffith applied the result from Inglis that, as shown in Fig. 6.2, the potential caused by the internal strain and external applied load can be written as:

$$\Pi = \Pi_0 - \frac{\pi\sigma^2 a^2 B}{E} \tag{49}$$

here, Π_0 is the potential energy for the uncrack plate, B is the thickness of the plate, σ is the constant stress applied far from crack, a is half of the length of crack, E is Young's modulus.

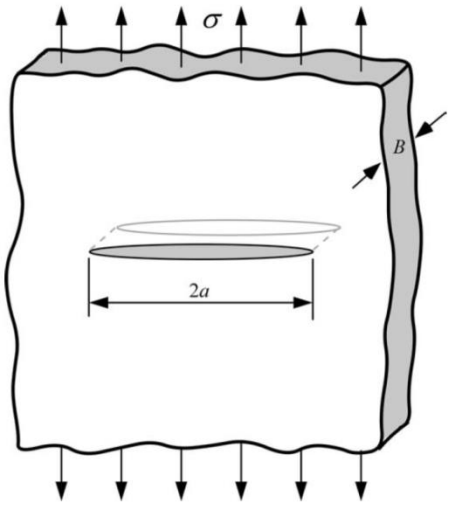

Fig. 6.2. Model of Griffith's facture analysis[56]. The model is simplified with $2a$ be the existing crack length, σ be the uniformly distributed load applied far from the crack.

Then, by Griffith energy balance, the total energy for the equilibrium with crack will have a minimum value, *i.e.*

$$\frac{dW_{total}}{dA_c} = \frac{d\Pi}{dA_c} + \frac{dW_s}{dA_c} = 0$$
$$W_s = 2A_c\gamma \tag{50}$$

here W_{total} is the total energy, A_c is the area of crack, W_s work required to create new surface, γ [unit: Newton/meter] is the surface energy of the material. By using Equation (50), the driving force, or the release of the elastic energy due to the propagation of cracks can be obtained as:

$$-\frac{d\Pi}{dA_c} = \pi\sigma^2 a / E = 2\gamma \tag{51}$$

For the current study, the model may not follow the conclusion from simple linear elastic Griffith model. It is necessary to introduce a modification to better understand the problem. Here, in Equation (51), instead of π, a non-dimensional geometrical factor *A* that depends on angle θ, *i.e.*, $A = A(\theta)$ is introduced. It is used to account the effect of different geometry. So the driving force applied in current calculation is:

$$-\frac{d\Pi}{dA_c} = A\sigma^2 a / E = 2\gamma \tag{52}$$

here σ is the normal traction applied on the crack surface and related to the moment *M* by Euler–Bernoulli beam theory $\sigma = \frac{(H/2)M}{H^3/12} = 6M/H^2$; and γ [unit: Newton/meter] is the surface energy. To obtain the value of the surface energy of the material, the J-integral is calculated. In the theory of facture mechanics for nonlinear elastic materials, the relation $J = -\frac{d\Pi}{dA_c}$ is commonly used. To obtain J-integral, FEA is applied. The geometry of the FEA model is shown in Fig. 6.3. Numerical integration along the elements on a circle with the crack tip as its center is done. The values of E, a and σ are fixed while θ changes from 0 to $\pi/3$. For different angle θ different value of J-integral can be obtained. By using the relationship $J = -\frac{d\Pi}{dA_c} = A\sigma^2 a / E$, the value of A for the corresponding J can be obtained. Finally, the function $A = A(\theta)$ can be obtained. Combing all the derivation above, the critical moment for "crack growth" is given by:

$$M_{cr}^{\text{crack growth}} = H^2\sqrt{E\gamma/(2Aa)}/3 \tag{53}$$

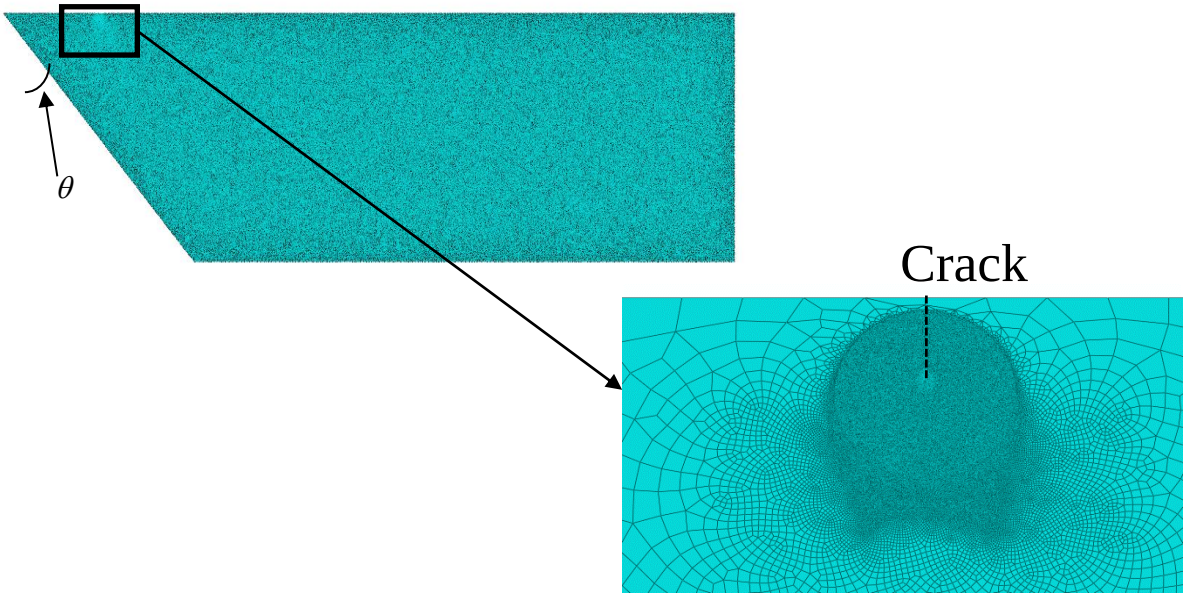

Fig. 6.3. Finite element model for the fracture analysis[3]. The existing crack is highlighted by the dash line. A zoom in view near the crack is shown on the lower right corner. The angle to characterize the geometry is denoted as θ.

For "plastic rolling", the rate of energy dissipation due to the plastic deformation during the rolling about the creases provides the resistance. During the plastic rolling (*i.e.*, the angle θ changes), the plastic zone is highlighted by the shaded area as shown in Fig. 6.4. The area of the plastic zone is $H^2\tan\theta/4$. So the critical moment $M_{cr}^{\text{plastic rolling}}$ for plastic rolling can be obtained by the following:

$$M_{cr}^{\text{plastic rolling}} = \partial\Pi^{\text{plastic rolling}}/\partial\theta = \partial\left(\beta H^2\tan\theta/4\right)/\partial\theta = \beta H^2\left(1+\tan^2\theta\right)/2 \tag{54}$$

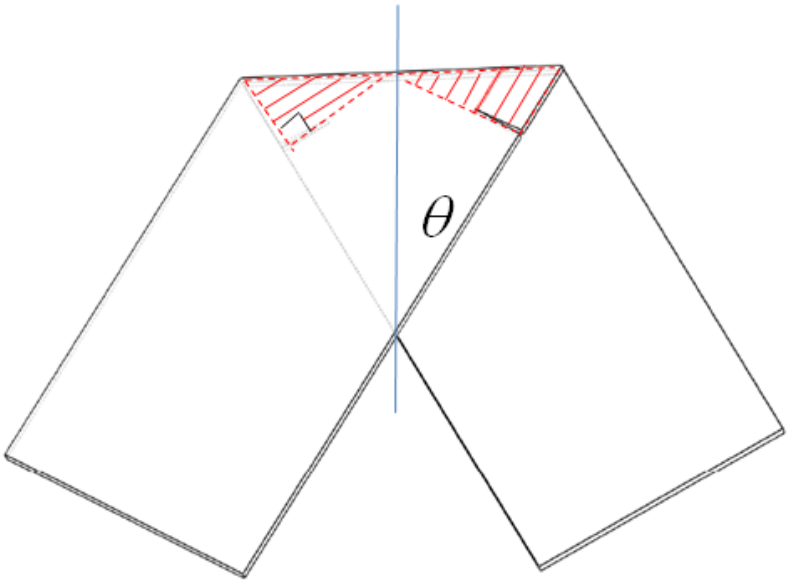

Fig. 6.4. Plastic zone generated during plastic rolling[3]. The plastic zone is highlighted as the shaded area.

Here the driving force is the rate of release of potential energy due to the increase of θ, given by $M/2$. β [unit: Newton/meter^2] is the dissipated energy per unit area due to plastic rolling, which is related to the extent of the plastic deformation (*i.e.*, hard crease versus soft crease) and can be associated with the yield stress of plastic materials. It was calculated by the simulation of folding a thin foil by a prescribed folding thickness. This problem was modeled by bending a thin film around a rigid circular die (as shown in Fig. 6.5). It is used as an analogy of the real folding process, in which the diameter of the rigid circular die corresponds to the folding thickness. The material parameters of Al were used in the analysis. Contact was defined between the deformable thin foil and the

rigid die. 1,571 B22 (3-node quadratic beam) elements are used in the analysis. Once the thin foil enters the plastic zone, the plastic energy density can then be calculated.

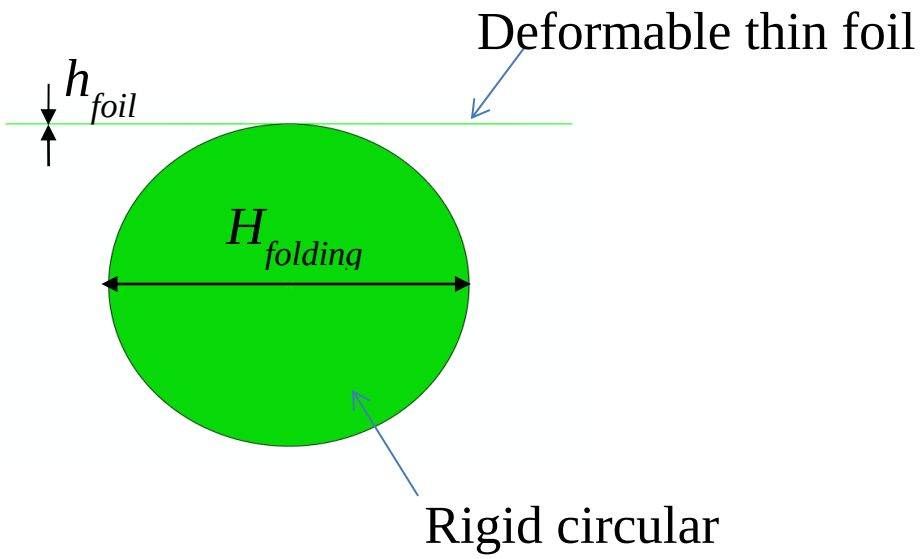

Fig. 6.5. FEA model for the calculation of the energy dissipation density due plastic rolling for different folding situation[3]. $H_{folding}$ is the diameter of the rigid die and h_f is the thickness of the thin foil.

When M is applied, the smaller one between $M_{cr}^{\text{crack growth}}$ and $M_{cr}^{\text{plastic rolling}}$ is activated as the critical moment during deformation, which leads to either "crack growth" mode, when $M_{cr}^{\text{crack growth}} < M_{cr}^{\text{plastic rolling}}$, or "plastic rolling" mode, when $M_{cr}^{\text{plastic rolling}} < M_{cr}^{\text{crack growth}}$.

Finite element simulations were conducted using commercial package ABAQUS to analyze these two deformation modes. Because in a lithium-ion battery (LIB), Al foil tends to crack due to its lowest fracture toughness, the material parameters of Al were used in the analysis, with the surface energy $\gamma = 0.868N/m$, elastic modulus $E = 69GPa$, and Poisson's ratio $\nu = 0.33$[57,58]. The geometry is H = 3 mm, and L = 10

mm to match with the experiments. The pre-existing crack is assumed small as compared with the width *H*. β, dissipated plastic energy per area, is calculated by folding a 10 μm-thick Al foil (the same thickness as that used in LIB) with different folding radius via finite element simulations. Thus the plot of β and ratio between the folding thickness and foil thickness $H_{folding} / h_{foil}$ can be obtained, which is shown in Fig. 6.6. It is found that as the ratio $H_{folding} / h_{foil}$ increases, β decreases.

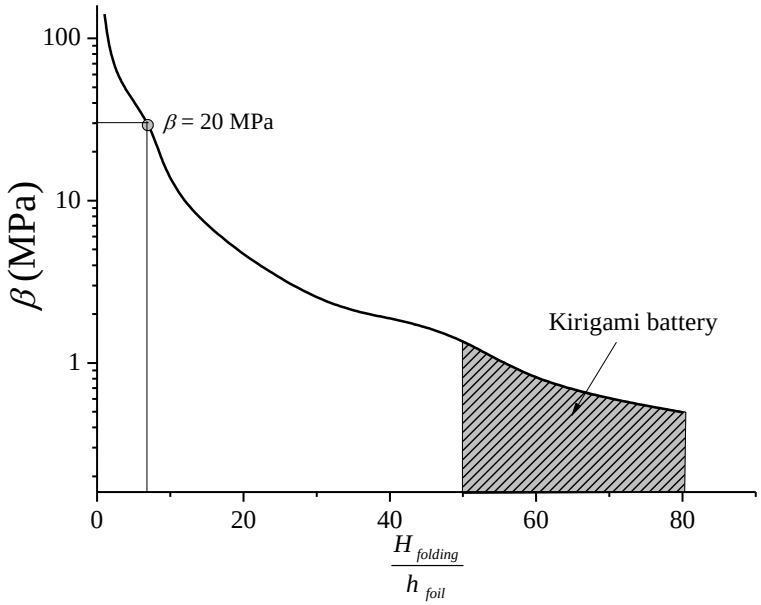

Fig. 6.6. The dissipated plastic energy per area (β) as a function of the extent of the folding crease that is characterized by the ratio between folding thickness $H_{folding}$ and foil thickness h_{foil} [3].

Figure 6.7 shows the "safe zone" (*i.e.*, $M_{cr}^{\text{crack growth}} / M_{cr}^{\text{plastic rolling}} > 1$) and the "fracture zone" (*i.e.*, $M_{cr}^{\text{crack growth}} / M_{cr}^{\text{plastic rolling}} < 1$) as a function of θ for various *a* and β. For example, *a* =

0.03 mm (*i.e.*, 1% of *H*, the width of strip) and β = 20 MPa, corresponding in creating a sharp crease of a 10 μm-thick Al foil with bending diameter of 70 μm (see Fig. 6.6), "safe mode" is activated for all angle of θ. The results also show that for a larger β (or equivalently shaper crease) or *a* (*i.e.*, larger initial crack), "fracture mode" tends to occur. For the real battery setup, Al foil is $10\mu m$ in thickness, while the entire battery cell is $500\mu m \sim 800\mu m$ in thickness depending on the mass loading of the active materials, which gives the ratio $H_{folding} / h_{foil}$ about 50 to 80. Within this range, Fig. 6.6 shows that β is on the order of 1 MPa, which indicates that it is always the scenario to activate the "safe mode". Thus this analysis verifies that the robust electrochemical and mechanical performance of the kirigami LIB is due to the activated "safe mode".

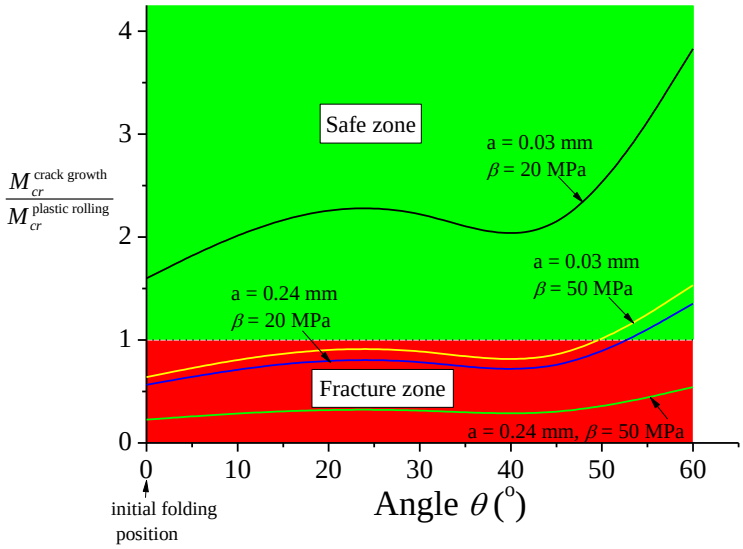

Fig. 6.7. Theoretical analysis of kirigami crack growth versus plastic rolling[3]. (**A**) Illustration of the two deformation modes, *i.e.* crack growth and plastic rolling. (**B**) "Safe zone" and "fracture zone" that are characterized by the ratio of critical moments, *i.e.*, $M_{cr}^{\text{crack growth}} / M_{cr}^{\text{plastic rolling}}$, as a function of angle θ, for various a and β.

CHAPTER 7 : STRETCHABILITY OF ARCHIMEDEAN SPIRAL BASED INTERCONNECTION DESIGN

In this chapter, a new interconnection pattern is designed for large stretchability. The contour line for the interconnection is called Archimedean spiral. Instead of using periodic patterns with high in-plane curvature as in conventional designs, current design is non-periodic with relative low in-plane curvature. To illustrate the outstanding stretchability of the pattern, stretchability of two of the most commonly seen patterns for the interconnection are compared with it under the same constraints. The new design is proved to provide great improvement on stretchability.

For a typical island-interconnect structure, at the unstrained state, the islands should occupy the majority of the in-plane area to increase the areal coverage. Without losing generality, a 2 mm $\times$ 2 mm island and a 1 mm gap between islands are considered, where a 2 mm $\times$ 2 mm island size is consistent with the size of some small chips and the areal coverage can achieve over 45%. Thus the area can be filled in by interconnects is 2 mm $\times$ 1 mm. In this area, one interconnect or multiply interconnects can be placed. From the consideration of electrical conductivity, multiply interconnects have the merit since the breaking of one interconnect does not cause the electrical failure of the entire structure. Thus it is considered to place four identical interconnects in the gap and each interconnect occupies no more than 0.5 mm (height) $\times$ 1 mm (width). Another constraint to fairly compare the stretchability among different interconnects is that the same cross-sectional area and in-plane contour length should be used and thus the electrical resistance among different interconnects are the same. With these constraints in placed, three different interconnects are studied (See Fig. 7.1).

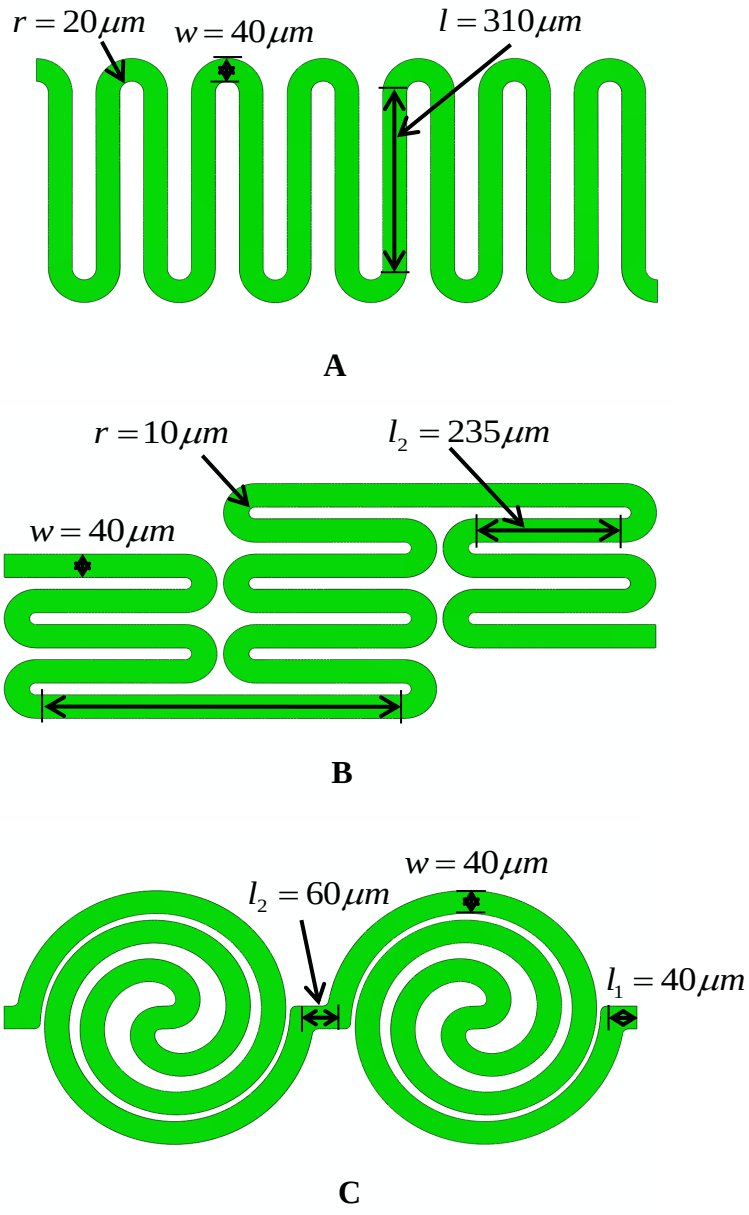

Fig. 7.1. Geometry with dimensions for three interconnections[4]. (**A**) Geometry and dimension of serpentine pattern. (**B**) Geometry and dimension of fractal pattern. (**C**) Geometry and dimension of Archimedean spiral pattern.

The in-plane shapes and the dimensions of the three interconnects patterns are shown in Fig. 7.1, A, B and C, with names of regular serpentine, self-similar serpentine and Archimedean spiral, respectively. The regular serpentine has been extensively used as interconnects and the self-similar serpentine was studied very recently and found to be more stretchable under different constraints [22]. Here this new pattern is proposed, Archimedean spiral. The patterns have the same thickness of 1 μm and the same strip width of 40 μm. The radius used in the regular and semi-similar serpentines is 20 μm and 10 μm, respectively. Other geometrical parameters are designed to satisfy the constraints as discussed in the previous section. In addition to the parameter shown in Fig. 7.1, the Archimedean spiral is prescribed by an analytical function in the polar coordinate as $r = \pm 60\theta^{1/1.7}$, $\theta = [0, 3\pi]$, and thus all three patterns have approximately the same span of 1000 μm in *x*-direction, the same height of 400 μm in *y*-direction and the approximately same contour length of 5,650 μm. The interconnections are modelled as copper. The Young's modulus E is $119GPa$ and the Poisson's ratio ν is 0.34 [22]. Plasticity is considered and described by $\sigma = E\varepsilon_Y + E_p\varepsilon_p^n$ with ε_Y = 0.3% as the yield strain [22], E_p = 530 MPa, and n = 0.44 [59].

Finite element package ABAQUS is used to conduct the analysis. Buckling analysis is carried out to obtain the first 10 buckling modes followed by importing these 10 buckling modes with random weight factors as imperfections. Then the prescribed displacement is applied at the rightmost end to stretch the interconnections while the leftmost end is fixed. At certain loading step, the prescribed displacement is removed to

study if the deformation is recoverable. 20-node quadratic elements with reduced integration (C3D20R) are used in the analysis and the mesh convergence is ensured.

Fig. 7.2 to 7.4 show elastic stretchability of the three patterns (Fig. 7.1) under the constraints of the same in-plane span and contour length. Here the elastic stretchability is defined as at this critical strain the interconnection enters the plastic zone, *i.e.*, the maximum equivalent strain exceeds the yield strain. The capability of restoration when the stretch is removed was also studied. Thus both the deformed state at the critical strain and the released state when the stretch is removed are shown for the three patterns, with the color map showing the equivalent plastic strain. To compare, the two states (deformed and released) at the half way of the critical strain are also given, which is still at the elastic range and thus the deformation is fully recoverable.

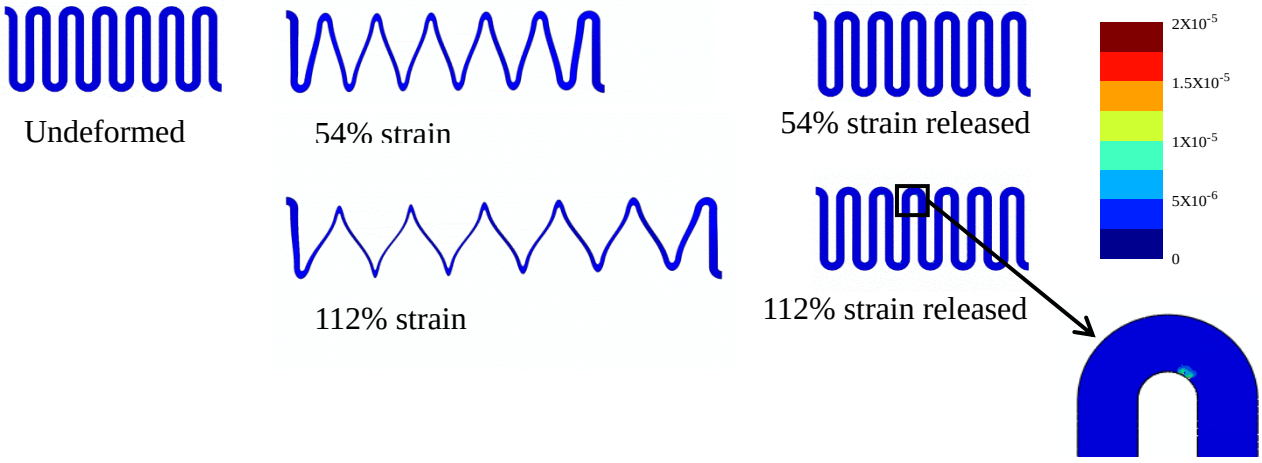

Fig. 7.2. Deformed and undeformed shapes of the three interconnect structures[4]. (**A**) 54% and 112% strain are applied on the serpentine structure (Fig. 7.1A) and followed by strain relaxation. For 112% applied strain, plasticity begins to happen. The zoom-in view for one of the strain concentration location is shown.

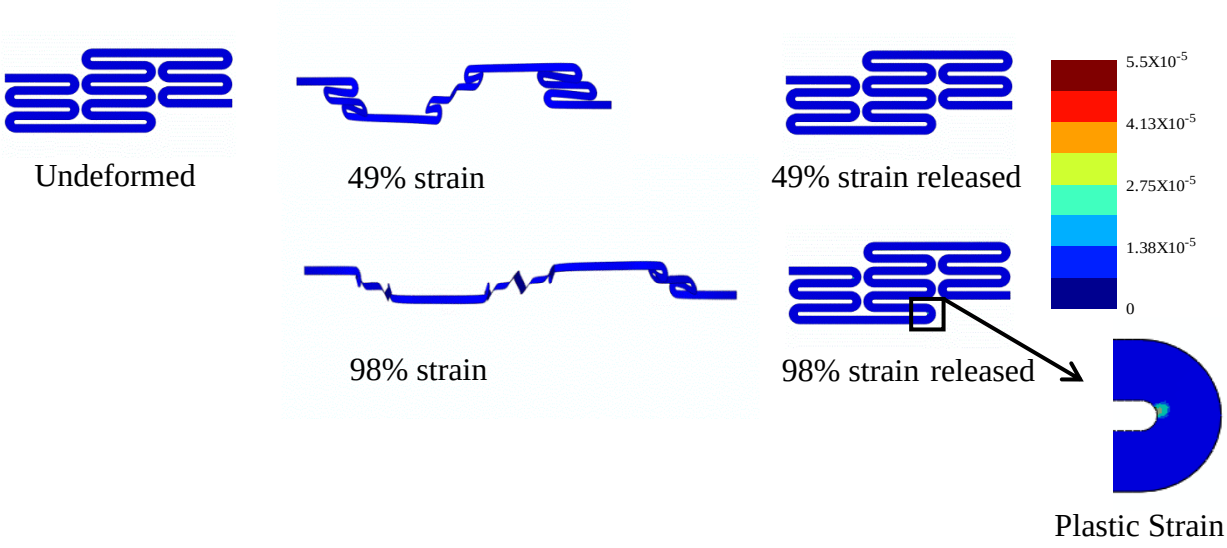

Fig. 7.3. 49% and 98% strain are applied on the semi-similar serpentine structure (Fig. 7.1B) and followed by strain relaxation[4]. For 98% applied strain, plasticity begins to happen. The zoom-in view for one of the strain concentration location is shown.

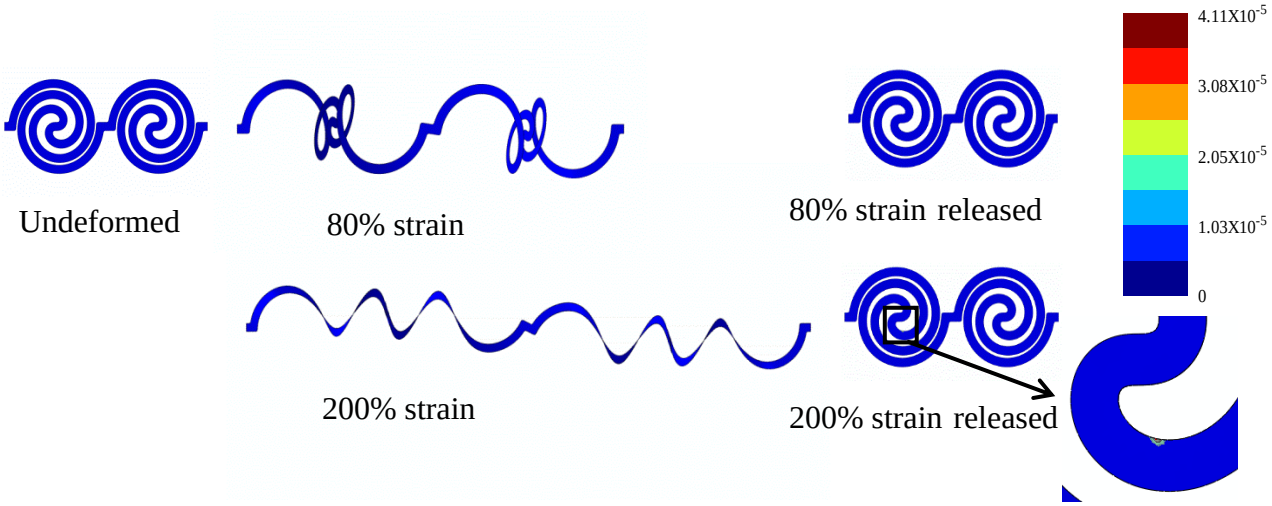

Fig. 7.4. 80% and 200% strain are applied on the Archimedean spiral structure (Fig. 7.1C) and followed by strain relaxation[4]. For 200% applied strain, plasticity begins to happen. The zoom-in view for one of the strain concentration location is shown. The color maps indicate the magnitude of the equivalent plastic strain.

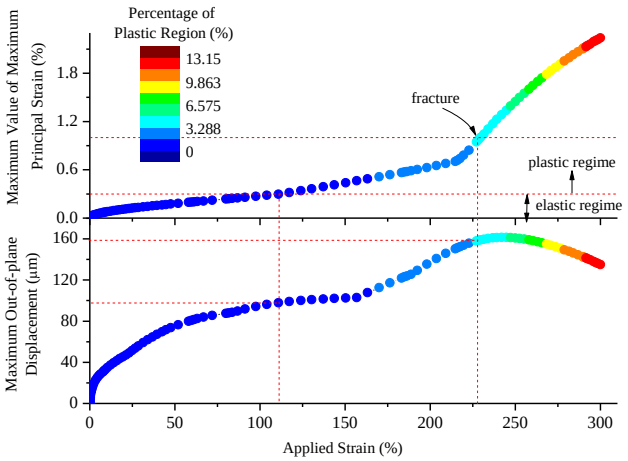

A

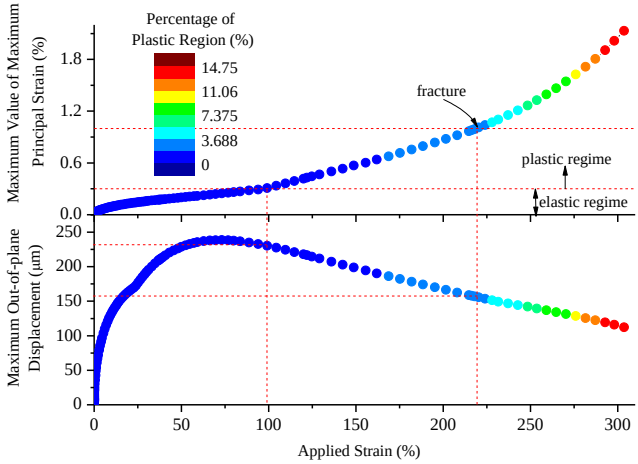

B

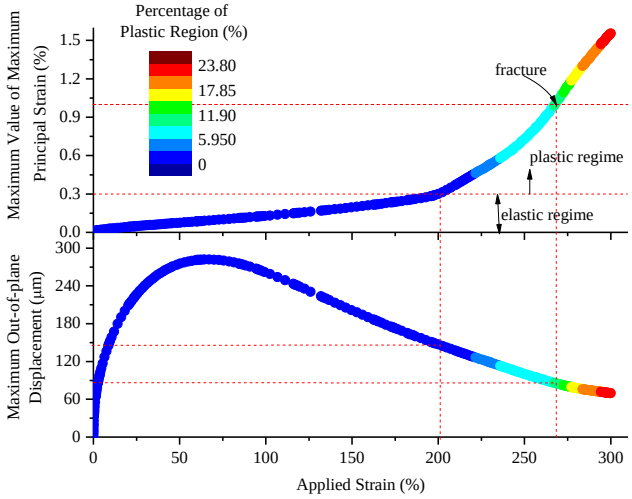

C

Fig. 7.5. The relationship between the maximum value of the maximum principal strain, maximum out-of-plane displacement and the applied strain with a color map indicating percentage of plastic zone[4]. (**A**) the serpentine structure, (**B**) the self-similar structure, and (**C**) the Archimedean spiral structure.

The results clearly show that the Archimedean spiral has the largest elastic stretchability, up to 200%, while the regular serpentine and the semi-similar serpentine have 112% and 98% elastic stretchability, respectively. The deformed states show that the in-plane stretching is companied by out-of-plane deformation (mainly twisting and bending) or in other words, the out-of-plane deformation compensates the in-plane deformation. Particularly for the Archimedean spiral structure, the unfolding-like deformation occurs to compensate the in-plane stretching. When the critical strain is released, the interconnects almost recover to the undeformed shapes, even when the plastic deformation has occurred, which is because at the critical point or little over the critical point, the regions that enter the plastic zone are very limited and the majority of the interconnects are still within the elastic domain. Not surprisingly, the plastic deformation is localized at the regions with large curvature. The reason that the comparison on elastic stretchability between the regular serpentine and the semi-similar serpentine is different from the previous study [22] is due to the different constraints.

Figure 7.5 further compares the stretchability of the three patterns. Here the stretchability is defined as the critical strain at which the maximum of the maximum principal strain exceeds the fracture strain, 1%. Fig. 7.5 also compares the out-of-plane deformation among these three patterns. The color map indicates the percentage of the materials with plastic deformation. The results conclude that the Archimedean spiral still has the largest stretchability, up to 270%, while the other two serpentine structures are very similar, with about 220% stretchability. The Archimedean spiral structure also has the greatest out-of-plane deformation when the outer ring of the spiral rotates to compensate the in-plane stretching. From the application perspective, smaller out-of-

plane deformation is desired in order to have denser stacking in the thickness direction. However the maximum out-of-plane deformation, 300 μm, is within the range of the thickness of a island or device, which will not affect the stacking density in the vertical direction. As the color map shows that the percentage of entering plastic deformation is rather small, on the order of 1%, which indicates that the structure has fairly good capability of restoring to the undeformed state even entering the plastic zone.

The comparisons shown in Fig. 7.2 to 7.5 seem to suggest that an uniform and small curvature may contribute to a greater stretchability under the constraints of same in-plane span and contour length. The regular and semi-similar serpentines have zero curvatures over the straight lines but also large curvatures at the junctions between straight lines. Because of the design limitations for the serpentine based structures, large curvatures are needed to have a large areal filling ratio. Thus the curvature for the serpentine based structure has to change from zero to a large curvature. To obtain a smooth and small curvature along the contour length, lessons can be sought from nature, which in fact motivated this work to study the spiral structures. One particular pattern is the golden spiral that can be found in many species, such as a nautilus shell, where the curvature evolves smoothly along the contour length. However, the golden spiral (expressed in $r = ae^{b\theta}$ in a polar coordinate system) cannot be directly applied as a stretchable interconnect because the spiral lines aggregate at the center of the spiral, in other words, the spacing between the spiral lines decreases as the spiral curves to the center, which leads to large curvatures and does not benefit the stretchability of the interconnects. Therefore, the Archimedean spiral (in general $r = \pm a\theta^t$ ($t < 1$) in a polar

coordinate system) is used to have a uniform and small curvature along the contour length.

However, the Archimedean spiral also has one limitation, which is the horizontal span and vertical span are very close; such that to fill in a non-square area (*e.g.*, 1 mm in width and 0.5 mm in height as in this Letter), two spirals have to be used. To make the spiral-based structure more versatile to fit in non-square area, a modified Archimedean spiral is used, as shown in Fig. 7.6A. The spirit of this modification is to adjust the ratio between the horizontal and vertical dimensions to fit the non-square area. The approach used here is to modify the original Archimedean spiral by multiplying with a smooth approximation to a step function of θ in polar coordinate system and then inserting straight lines to fit the in-plane area.

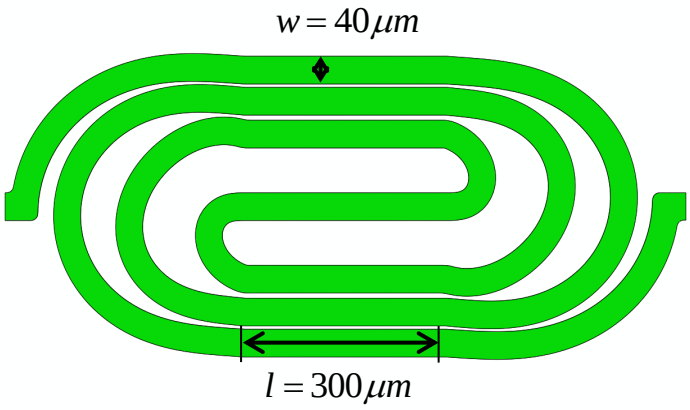

A

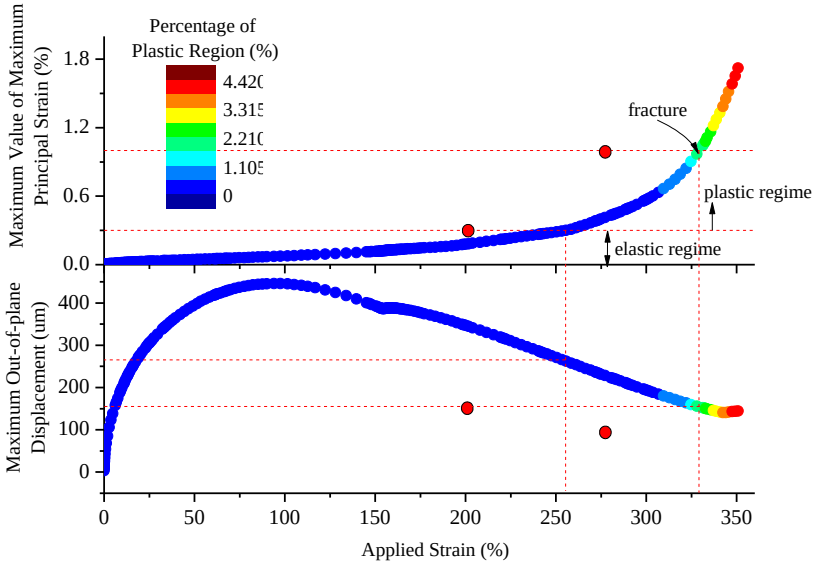

B

Fig. 7.6. Geometry and results for the modified Archimedean spiral design[4]. (**A**) In-plane geometry and dimensions of the modified Archimedean spiral design. (**B**) The relationship between the maximum value of the maximum principal strain, maximum out-of-plane displacement and the applied strain with a color map indicating percentage of plastic zone for the modified Archimedean spiral design. The red dots show the corresponding results for the original spiral design (Fig. 7.1C).

The stretchability of the modified Archimedean spiral was then studied by applying a prescribed displacement at one end while the other end is fixed and the results are shown in Fig. 7.6B. The same legend as that in Fig. 7.5 was used here and the results for the original spiral design were marked by the red dots. Clearly, Fig. 7.6B shows that the modified Archimedean spiral is more stretchable than the original spiral design, with over 250% elastic stretchability and 325% stretchability before fracture. The maximum out-of-plane displacement is about 450 μm and acceptable. The reason that the modified Archimedean spiral is more stretchable is because the newly added straight portions make the structure easier to generate out-of-plane deformation while at the same time does not introduce large curvatures.

CHAPTER 8 : SIDE PROJECT: SIMULATION OF HYDROCHLORIC ACID IN GELATIN

The content in this chapter illustrates another very important aspect of my research. It shows the simulation of deformation of gelatin in hydrochloric acid which will form a gel. During the deformation process, the diffusion will increase the volume of the gel and, at the same time, the chemical reaction between gelatin and hydrochloric acid will reduce the volume of the gel. I developed a 1D theory to explain the phenomenon. This is for the first time the theory is developed with chemical reaction coupling with diffusion and large deformation of a gel. The final result from the 1D theory for the deformation of gel is compared with experimental results. Good agreement of the two results indicates the accuracy of the newly developed 1D theory. Please note I only involved in the design of physical experiment shown in this chapter. The actual physical experiments were done by Xu Wang.

Numerous works have been carried out on the simulation of gel including large deformation[60], capillary force[61], mass diffusion[62-66], heat transfer[67,68], electrical field[69] and so on. However, few of them consider the effect of chemical reaction and its effect on the volume change on gel. Based on the fact, I decided to couple the chemical reaction into the deformation process of gel. This section summarizes the general derivation of the related theory and presents some of the primary results[70].

To begin the discussion, the experiment process should be briefly described. A gelatin sheet with dimensions of 160 μm (thickness) × 1,090 μm × 4,000 μm was used for the observation. The gelatin sheet was held vertically by a sponge stage in a glass dish

under an optical microscope in room temperature 25 $^{\circ}C$. The sponge stage was able to keep the gelatin sheet standing in the glass dish and impose mechanical constraints in the horizontal direction. To implement this in experiments, by surrounding the gelatin film with sponge, the sponge is able to confine the gelatin film horizontally, while leave the films relatively free to swell in the thickness direction. The simulated gastric fluid was composed of 2.0 g of sodium chloride and 3.2 g of purified pepsin (derived from porcine stomach mucosa, with an activity of 800 to 2,500 units per mg of protein) in 7.0 mL of hydrochloric acid (HCl) and water (1000 mL). This test solution has a pH of about 1.2. When the sponge was soaked with simulated gastric fluid and touched the gelatin sheet, it could be used to simulate the gelatin sheet in stomach environment. After the simulated gastric fluid was poured into the glass dish, swelling and digestion of the gelatin sheet were observed *in-situ* by microscopy (Nikon eclipse lv100). It was observed that a gelatin sheet with an initial cross-sectional area of 160 μm × 1,090 μm first swells due to the diffusion of the gastric fluid into the polymeric gelatin network, and then shrinks due to the digestion of gelatin and eventually becomes undetectable microscopically (Nikon eclipse lv100, 5X objective) after 2.5 hours. During this process (swelling → shrinking), because of the constraint in the horizontal direction, the maximum strain in the horizontal direction $\varepsilon_{horizontal}$ was only 17%, while its counterpart in the thickness direction $\varepsilon_{thickness}$ was 261%. This quasi-one-dimensional constrained digestion process can be understood by a theoretical model that considers the coupling of mass diffusion, chemical reaction, and extremely large mechanical deformation.

A theoretical model was developed to characterize the digestive process. This model considers the coupling of mass diffusion, chemical reaction as well as the

nonlinear mechanical behavior. The mixture of gelatin and HCl forms a gel, with the former as polymeric network and later as solvent. During the digestive process, the HCl will have chemical reaction with gelatin. This in general complex chemical reaction will cause the reduction of gelatin network, which will lead to the reduction of the gel volume. To characterize the digestive process, classical gel model with coupled diffusion and large deformation[60,62] will be applied and the first order reaction will be introduced to account for the volume reduction caused by chemical reaction.

The general time-dependent diffusion equation with Fickian first law is used to model the diffusion of HCl in gelatin, *i.e.*

$$\frac{d}{dt}\int_V C dV + \int_a j_i n_i da = r\,, \tag{55}$$

$$j_i = cD\frac{\partial \overline{\mu}}{\partial x_i}, \tag{56}$$

where C and c are the nominal and true concentration of HCl in gel, V is the initial volume of gel, $\mathbf{j}$ is true flux of HCl into the gel, a is current area of gel, $\mathbf{n}$ is the normal vector of a surface in the current state, r is the source of HCl generation, the subscript i can vary from 1 to 3.

The first-order chemical reaction model is applied here as the source of HCl generation, *i.e.*

$$r = \int_V kC dV \tag{57}$$

where k is the first-order reaction constant[71].

For nonlinear solid mechanics part, the normalized free energy can be written as

$$\bar{W}\left(\mathbf{F}^{diff},C\right)=\frac{W\left(\mathbf{F}^{diff},C\right)}{RT/v}=\frac{W_s\left(\mathbf{F}^{diff}\right)+W_m\left(C\right)}{RT/v}$$
$$=\frac{1}{2}nv\left[F_{iK}^{diff}F_{iK}^{diff}-3-2\ln\left(\det\mathbf{F}^{diff}\right)\right]+RT\left[C\ln\left(\frac{Cv}{1+BC}\right)+\frac{\chi C}{1+BC}\right] \tag{58}$$

Here The deformation gradient $\mathbf{F}=\partial\mathbf{x}/\partial\mathbf{X}$ is decomposed into the mechanical stretch part and chemical reaction part using polar decomposition, *i.e.*, $\mathbf{F}=\mathbf{F}^{diff}\cdot\mathbf{F}^{rec}$, where $\mathbf{F}^{diff}$ is the diffusion induced deformation and $\mathbf{F}^{rec}$ represents the chemical reaction induced deformation. $\mathbf{F}^{diff}$ stretches the polymeric network, and $\mathbf{F}^{rec}$ eliminate materials (*i.e.*, digestion). $W_s\left(\mathbf{F}^{diff}\right)$ and $W_m\left(C\right)$ are the stretch energy (depending on $\mathbf{F}^{diff}$) and mixing energy (depending on nominal concentration *C*), respectively, R is the gas constant and T is temperature of the gel. χ is the dimensionless parameter that relates to the enthalpy of mixing. n is the molar number of chain divided by the dry volume of gel with a unit of mol/m^3. The incompressibility of all the particles is assumed, so that the following can be obtained:

$$1+Cv-kCtn_AV_A=1+\left(v-ktn_AV_A\right)C=1+BC=\det\mathbf{F} \tag{59}$$

$$1+Cv=\det\mathbf{F}^{diff} \tag{60}$$

where v and V_A are the molar volume of HCl and gelatin, respectively, n_A is the molar ratio between the reactant A (gelatin) and the solvent (HCl) in the chemical reaction balance and t is the total simulation time.

Substitute Eq. (59) into Eq. (58) and use the Legendre transformation, the following can be obtained:

$$\hat{W}\left(\mathbf{F}^{diff},\mathbf{F},\mu\right)=\bar{W}\left(\mathbf{F}^{diff},C\right)-\mu C=\bar{W}'\left(\mathbf{F}^{diff},\mathbf{F}\right)-\mu\left(\det\mathbf{F}^{diff}-1\right)/v \tag{61}$$

where $\hat{W}$ is defined as a function of $\mathbf{F}^{diff}$, $\mathbf{F}$ and μ.

Notice here, due to the chemical reaction, the reduction of the material which affects the reference volume needs to be considered. So the relation can be obtained as:

$$\hat{W}\left(\mathbf{F}^{diff},\mathbf{F},\mu\right)V' = \tilde{W}\left(\mathbf{F}^{diff},\mathbf{F},\mu\right)V \tag{62}$$

where $V' = V\det\mathbf{F}^{rec}$ is the reduced volume of gel considering the effect of chemical reaction and $\tilde{W}\left(\mathbf{F}^{diff},\mathbf{F},\mu\right)$ is the modified free energy. As hyperelastic model is applied to calculate the large deformation behavior of the gel, the normalized nominal stress can be obtained:

$$\frac{v\mathbf{s}\left(\mathbf{F}^{diff},\mathbf{F},t\right)}{RT} = \frac{\partial\tilde{W}\left(\mathbf{F}^{diff},\mathbf{F},t\right)}{\partial\mathbf{F}^{diff}} \tag{63}$$

As described before in the experiment part, the change of the in-plane stretch ratio is very small compared to the out-of-plane one, a 1D model is developed based on the general 3D model mentioned above. Thus the deformation gradient can be written as:

$$\mathbf{F} = \mathbf{F}_c\mathbf{F}_r = \begin{pmatrix}\lambda_{1c} & 0 & 0\\ 0 & \lambda_{2c} & 0\\ 0 & 0 & \lambda_{3c}\end{pmatrix}\begin{pmatrix}\lambda_{1r} & 0 & 0\\ 0 & \lambda_{2r} & 0\\ 0 & 0 & \lambda_{3r}\end{pmatrix} = \begin{pmatrix}1 & 0 & 0\\ 0 & 1 & 0\\ 0 & 0 & \lambda_{3c}\end{pmatrix}\begin{pmatrix}1 & 0 & 0\\ 0 & 1 & 0\\ 0 & 0 & \lambda_{3r}\end{pmatrix} = \begin{pmatrix}1 & 0 & 0\\ 0 & 1 & 0\\ 0 & 0 & \lambda_3\end{pmatrix} \tag{64}$$

where the in-plane stretch ratios due to diffusion and chemical reaction are fixed to one. $\lambda_3 = \lambda_{thickness}$ will be the only value to be calculated in the following analysis.

Combing Eq. (55) to (64), the time-dependent partial differential equation (PDE) of the out-of-plane stretch ratio λ_3 can be obtained as:

$$\frac{1}{\lambda_1^2\lambda_3}\lambda_1^2\frac{\partial\lambda_3}{\partial t} = \frac{\partial}{\partial x_3}\left[\frac{D\left(\lambda_1^2\lambda_3-1\right)}{\lambda_1^2\lambda_3}\frac{\partial\bar{\mu}}{\partial x_3}\right] - \frac{k\left(\lambda_1^2\lambda_3-1\right)}{\lambda_1^2\lambda_3}\left(1+\frac{n_AV_A}{B}\right) \tag{65}$$

where

$$\bar{\mu}(X_3,t)=\frac{UP}{DOWN}=\frac{\begin{array}{l}3\dfrac{\partial\lambda_{3r}}{\partial\lambda_3}\left\{\dfrac{1}{2}nB\left[2\lambda_1^2+\dfrac{\lambda_3^2}{\lambda_{3r}^2}-3-2\ln\left(\dfrac{\lambda_1^2\lambda_3}{\lambda_{3r}}\right)\right]+\left(\lambda_1^2\lambda_3-1\right)\ln\left(\dfrac{\lambda_1^2\lambda_3-1}{B\lambda_1^2\lambda_3}v\right)+\dfrac{\lambda_1^2\lambda_3-1}{\lambda_1^2\lambda_3}\chi_1\right\}\\ +\lambda_{3r}\left\{nB\left[\dfrac{v}{B\lambda_1^2}+\dfrac{v^2\lambda_3}{B^2}-\dfrac{v^2}{B^2\lambda_1^2}-\dfrac{\lambda_1^2v}{B+\left(\lambda_1^2\lambda_3-1\right)v}\right]+\dfrac{1}{\lambda_3}+\lambda_1^2\ln\left(\dfrac{\left(\lambda_1^2\lambda_3-1\right)v}{B\lambda_1^2\lambda_3}\right)+\dfrac{\chi_1}{\lambda_1^2\lambda_3^2}\right\}\end{array}}{3\left(\lambda_1^2\lambda_3-1\right)\dfrac{\partial\lambda_{3r}}{\partial\lambda_3}+\lambda_1^2\lambda_{3r}}$$

,

$$\frac{\partial\bar{\mu}}{\partial x_3}=\frac{1}{DOWN}\frac{\partial UP}{\partial x_3}-\frac{UP}{DOWN^2}\frac{\partial DOWN}{\partial x_3},$$

$$\frac{\partial UP}{\partial x_3}=\frac{\partial\lambda_3}{\partial x_3}\left\{\begin{array}{l}3\dfrac{\partial^2\lambda_{3r}}{\partial\lambda_3^2}\left\{\dfrac{1}{2}nB\left[2\lambda_1^2+\dfrac{\lambda_3^2}{\lambda_{3r}^2}-3-2\ln\left(\dfrac{\lambda_1^2\lambda_3}{\lambda_{3r}}\right)\right]+\left(\lambda_1^2\lambda_3-1\right)\ln\left(\dfrac{\lambda_1^2\lambda_3-1}{B\lambda_1^2\lambda_3}v\right)+\dfrac{\lambda_1^2\lambda_3-1}{\lambda_1^2\lambda_3}\chi_1\right\}\\ +4\dfrac{\partial\lambda_{3r}}{\partial\lambda_3}\left\{nB\left[\dfrac{v}{B\lambda_1^2}+\dfrac{v^2\lambda_3}{B^2}-\dfrac{v^2}{B^2\lambda_1^2}-\dfrac{\lambda_1^2v}{B+\left(\lambda_1^2\lambda_3-1\right)v}\right]+\dfrac{1}{\lambda_3}+\lambda_1^2\ln\left(\dfrac{\left(\lambda_1^2\lambda_3-1\right)v}{B\lambda_1^2\lambda_3}\right)+\dfrac{\chi_1}{\lambda_1^2\lambda_3^2}\right\}\\ +\lambda_{3r}\left\{nB\left[\dfrac{v^2}{B^2}+\dfrac{\lambda_1^4v^2}{\left[B+\left(\lambda_1^2\lambda_3-1\right)v\right]^2}\right]-\dfrac{1}{\lambda_3^2}+\dfrac{\lambda_1^2}{\left(\lambda_1^2\lambda_3-1\right)\lambda_3}-\dfrac{2\chi_1}{\lambda_1^2\lambda_3^3}\right\}\end{array}\right\}$$

,

$$\frac{\partial DOWN}{\partial x_3}=\frac{\partial\lambda_3}{\partial x_3}\left\{4\lambda_1^2\frac{\partial\lambda_{3r}}{\partial\lambda_3}+3\left(\lambda_1^2\lambda_3-1\right)\frac{\partial^2\lambda_{3r}}{\partial\lambda_3^2}\right\}.$$

The PDE shown above is solved by using commercial software COMSOL. The module of coefficient form PDE is used. The geometry of the model is only one straight line with a length of $160\mu m$. For material properties, shear modulus $nRT=33.3kPa$ and the value of $RT/v=4\times10^7Pa$, $v=1\times10^{-5}m^3/mol$ are firstly obtained[62,72,73]. To calculate the free swelling of gel without considering the effect of chemical reaction, the incompressible condition needs to be modified as: $1+Cv=\det(\mathbf{F})$, *i.e.* $B=v$.

Substituting it to the Eq. (65) and using the experiment data for the stretch ratio of 400%, $\chi_1 = 0.554$ can be obtained. Diffusivity $D = 8\times10^{-10} m^2/s$ is obtained through fitting the short-time-range data for the stretch ratio $\lambda_{thickness}$ from experiment due to the lack of exist data. The first-order reaction constant $k = 8\times10^{-5}/s$ is obtained by fitting the long-time-range data for the stretch ratio $\lambda_{thickness}$ from experiment due to the difficulty on measuring it from experiment. For boundary conditions, the flux of one side is fixed to be zero, *i.e.* $\frac{\partial \bar{\mu}}{\partial x_3} = 0$. The chemical potential is fixed to be zero on the other side, *i.e.* $\bar{\mu} = 0$. After solving the PDE, the curve of the simulation for the stretch ratio $\lambda^s_{thickness}$, which is shown in Fig. 9.1, can be obtained.

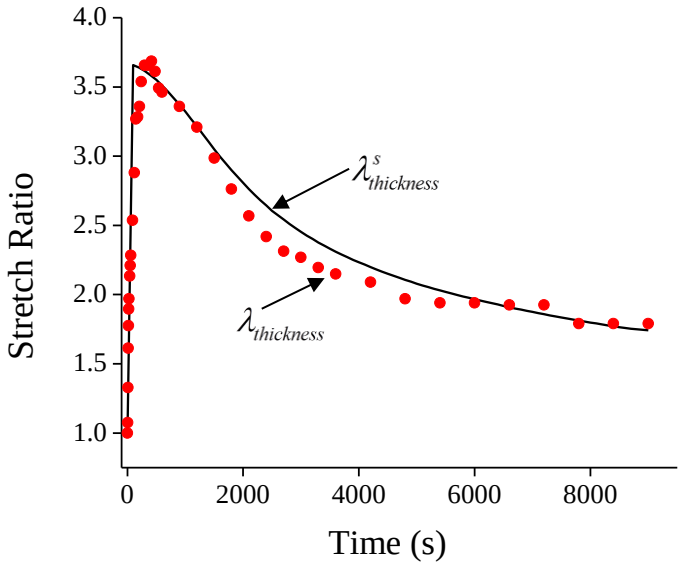

Fig. 8.1. Comparison of experimental and FEA result for the out-of-plane (in the direction of thickness) stretch ratio of the gel[70]. Here the red dots stand for the experimental data and the black solid stand for the data from analytical expression

derived form the 1D theory. The symbol $\lambda^{s}_{thickness}$ stands for stretch ratio from simulation and the symbol $\lambda_{thickness}$ stands for stretch ratio from experiment.

CHAPTER 9 : CONCLUSIONS

My research starts from relative simple single degree of freedom origami pattern: Miura-ori. In the theoretical analysis for the Poisson's ratio, the non-periodic nature of Miura-ori, which is often ignored by other related theories, has been included. By the introduction of the non-periodic feature, the in-plane Poisson's ratio, which was long believed to be always negative, is shown can change from negative to positive. This effect will be more obvious when the pattern is with few periods. Geometric explanation is given to better understand the phenomenon. Current analytical solution can be readily utilized as a guide for design of general Miura-ori pattern.

After the study of relative simple origami based structure, more complex origami pattern with multi-degree of freedom, the water bomb, is studied. Based on the idea of atomic-scale finite element method (AFEM), a non-local finite element method (NFEM) and its corresponding ABAQUS user subroutine are developed to study the non-local effect of origami patterns. I also develop a general vector based method to derive the dihedral angles in rigid origami by using necessary nodal coordinates. For the current study, water bomb is used as an example to illustrate the power of the NFEM. The simulation result matches the real water bomb based structures very well. To study other origami patterns, only minor changes on the element definition are needed.

Then my study focus turns to non-rigid origami based structures. By including plasticity of material, which is long ignored by others in their simulation of origami, in the modelling of origami based structures, very local phenomenon called locking can be captured. By using dynamics explicit algorithm, final results can be obtained with

sufficient efficiency and accuracy. The final results suggest plasticity should be included in the simulation of origami based structures.

After the study of macroscale origami based structures, the microscale origami catches my attention. A new fabrication approach for the manufacture of microscale origami is proposed. By introducing the predesigned elevated wall on soft substrate and buckling of the thin film attached to the wall, a variety of microscale 3D complex origami pattern can be obtained. Comparison of FEA and experiment results proves the accuracy of current numerical analysis. Therefore, FEA can be readily applied as a tool to guide the design and optimization of the origami based structures.

Kirigami based structure, compared with origami based ones, provides much more degree of freedom. However, initial crack introduced during the fabrication process is an issue for this type of structures. To model a kirigami based lithium-ion battery, plastic deformation and the fracture mechanism are considered. By using a new method combines FEA and classical theories, the geometric factors of the model can be tested numerically. Therefore, the features of kirigami based structure can be readily designed according to final result of simulation.

Finally, in order to make use of the advantage of kirigami, a new design of interconnection is proposed. Based on the observation of existing designs, an innovative Archimedean spiral kirigami pattern is applied to the design of the interconnection. By carry out the buckling analysis via FEA, the new non-periodic design with smaller in-plane curvature is proved to have much higher stretchability compared to the conventional periodic ones. Finally, a modified spiral pattern is also obtained based on

the understanding of the large deformation behavior of the interconnection. The modified pattern broadens the application of current design and provides even higher stretchability.

In the side project, the numerical calculation of HCl in gelatin couples the diffusion, chemical reaction and extremely large deformation behaviors. It is for the first time the influence of chemical reaction on the gel volume is considered in the gel simulation. From the comparison of the experimental and simulation results, very good match can be observed, which indicates the current 1D model is sufficient to capture all the necessary characteristics of the physical phenomenon while still ensure the high efficiency of numerical calculation.

By developing all the above theoretical and numerical models, I believe the understanding of origami and kirigami based structures, which are now more and more involved in our daily life, can go to the next level.

CHAPTER 10 : FUTURE WORK

For origami, more detailed geometry and the material behavior of the creases in the origami pattern can be formulated with higher accuracy. Introducing the cross section, *i.e.* the thickness of the pattern, will help to develop the concept of strain and stress and thus make the FEA more accurate. Introducing the effect of imperfection in the dynamics behaviors for origami will make the study relate more to practical applications. For the kirigami, model of crack can be refined to make it more accurate. For the HCl in gelatin, a 3D model can be developed to calculate general 3D case. The model of the chemical reaction can be improved to better fit the experiment results.

REFERENCES

1 Cheng Lv, Deepakshyam Krishnaraju, Goran Konjevod, Hongyu Yu, and Hanqing Jiang, 2014. Origami based mechanical metamaterials. *Scientific reports* **4**, 5979.

2 B Liu, Y Huang, H Jiang, S Qu, and KC Hwang, 2004. The atomic-scale finite element method. *Computer methods in applied mechanics and engineering* **193** (17), 1849-1864.

3 Zeming Song, Xu Wang, Cheng Lv, Yonghao An, Mengbing Liang, Teng Ma, David He, Ying-Jie Zheng, Shi-Qing Huang, and Hongyu Yu, 2015. Kirigami-based stretchable lithium-ion batteries. *Scientific reports* **5**, 10988.

4 Cheng Lv, Hongyu Yu, and Hanqing Jiang, 2014. Archimedean spiral design for extremely stretchable interconnects. *Extreme Mechanics Letters* **1**, 29-34.

5 Jonathan P Gardner, John C Mather, Mark Clampin, Rene Doyon, Matthew A Greenhouse, Heidi B Hammel, John B Hutchings, Peter Jakobsen, Simon J Lilly, and Knox S Long, 2006. The james webb space telescope. *Space Science Reviews* **123** (4), 485-606.

6 Christoffer Cromvik and Kenneth Eriksson, *Airbag folding based on origami mathematics*, presented at the Origami4: Fourth International Meeting of Origami Science, Mathematics, and Education, 2006, pp. 129-139.

7 Kaori Kuribayashi, Koichi Tsuchiya, Zhong You, Dacian Tomus, Minoru Umemoto, Takahiro Ito, and Masahiro Sasaki, 2006. Self-deployable origami stent grafts as a biomedical application of Ni-rich TiNi shape memory alloy foil. *Materials Science and Engineering: A* **419** (1), 131-137.

8 Rui Tang, Hai Huang, Hongen Tu, Hanshuang Liang, Mengbing Liang, Zeming Song, Yong Xu, Hanqing Jiang, and Hongyu Yu, 2014. Origami-enabled deformable silicon solar cells. *Applied Physics Letters* **104** (8), 083501.

9 Zeming Song, Teng Ma, Rui Tang, Qian Cheng, Xu Wang, Deepakshyam Krishnaraju, Rahul Panat, Candace K Chan, Hongyu Yu, and Hanqing Jiang, 2014. Origami lithium-ion batteries. *Nature communications* **5**, 3140.

10 Z. Yan, F. Zhang, J. C. Wang, F. Liu, X. L. Guo, K. W. Nan, Q. Lin, M. Y. Gao, D. Q. Xiao, Y. Shi, Y. T. Qiu, H. W. Luan, J. H. Kim, Y. Q. Wang, H. Y. Luo, M. D. Han, Y. G. Huang, Y. H. Zhang, and J. A. Rogers, 2016. Controlled Mechanical Buckling for Origami-Inspired Construction of 3D Microstructures in Advanced Materials. *Advanced Functional Materials* **26** (16), 2629-2639.

11 E. Hawkes, B. An, N. M. Benbernou, H. Tanaka, S. Kim, E. D. Demaine, D. Rus, and R. J. Wood, 2010. Programmable matter by folding. *Proc. Natl. Acad. Sci. U. S. A.* **107** (28), 12441-12445.

12 M. A. Dias, J. A. Hanna, and C. D. Santangelo, 2011. Programmed buckling by controlled lateral swelling in a thin elastic sheet. *Phys. Rev. E* **84** (3), 036603.

13 L. Ionov, 2011. Soft microorigami: self-folding polymer films. *Soft Matter* **7** (15), 6786-6791.

14 Y. Liu, J. K. Boyles, J. Genzer, and M. D. Dickey, 2012. Self-folding of polymer sheets using local light absorption. *Soft Matter* **8** (6), 1764-1769.

15 J. Kim, J. A. Hanna, M. Byun, C. D. Santangelo, and R. C. Hayward, 2012. Designing Responsive Buckled Surfaces by Halftone Gel Lithography. *Science* **335** (6073), 1201-1205.

16 J. Kim, J. A. Hanna, R. C. Hayward, and C. D. Santangelo, 2012. Thermally responsive rolling of thin gel strips with discrete variations in swelling. *Soft Matter* **8** (8), 2375-2381.

17 J. Ryu, M. D'Amato, X. D. Cui, K. N. Long, H. J. Qi, and M. L. Dunn, 2012. Photo-origami-Bending and folding polymers with light. *Applied Physics Letters* **100** (16), 161908.

18 Johannes TB Overvelde, Twan A de Jong, Yanina Shevchenko, Sergio A Becerra, George M Whitesides, James C Weaver, Chuck Hoberman, and Katia Bertoldi, 2016. A three-dimensional actuated origami-inspired transformable metamaterial with multiple degrees of freedom. *Nature communications* **7**, 10929.

19 Jesse L Silverberg, Arthur A Evans, Lauren McLeod, Ryan C Hayward, Thomas Hull, Christian D Santangelo, and Itai Cohen, 2014. Using origami design principles to fold reprogrammable mechanical metamaterials. *Science* **345** (6197), 647-650.

20 Jesse L Silverberg, Jun-Hee Na, Arthur A Evans, Bin Liu, Thomas C Hull, Christian D Santangelo, Robert J Lang, Ryan C Hayward, and Itai Cohen, 2015. Origami structures with a critical transition to bistability arising from hidden degrees of freedom. *Nature materials* **14** (4), 389-393.

21 F Lechenault and M Adda-Bedia, 2015. Generic Bistability in Creased Conical Surfaces. *Physical review letters* **115** (23), 235501.

22 Sheng Xu, Yihui Zhang, Jiung Cho, Juhwan Lee, Xian Huang, Lin Jia, Jonathan A Fan, Yewang Su, Jessica Su, and Huigang Zhang, 2013. Stretchable batteries

with self-similar serpentine interconnects and integrated wireless recharging systems. *Nature communications* **4**, 1543.

23 Dae-Hyeong Kim, Jizhou Song, Won Mook Choi, Hoon-Sik Kim, Rak-Hwan Kim, Zhuangjian Liu, Yonggang Y Huang, Keh-Chih Hwang, Yong-wei Zhang, and John A Rogers, 2008. Materials and noncoplanar mesh designs for integrated circuits with linear elastic responses to extreme mechanical deformations. *Proceedings of the National Academy of Sciences* **105** (48), 18675-18680.

24 Sheng Xu, Yihui Zhang, Lin Jia, Kyle E Mathewson, Kyung-In Jang, Jeonghyun Kim, Haoran Fu, Xian Huang, Pranav Chava, and Renhan Wang, 2014. Soft microfluidic assemblies of sensors, circuits, and radios for the skin. *Science* **344** (6179), 70-74.

25 Dahl-Young Khang, Hanqing Jiang, Young Huang, and John A Rogers, 2006. A stretchable form of single-crystal silicon for high-performance electronics on rubber substrates. *Science* **311** (5758), 208-212.

26 Robert J Lang and Thomas C Hull, 2005. Origami design secrets: mathematical methods for an ancient art. *The Mathematical Intelligencer* **27** (2), 92-95.

27 Robert J Lang, *A computational algorithm for origami design*, presented at the Proceedings of the twelfth annual symposium on Computational geometry, 1996, pp. 98-105.

28 E Cerda and L Mahadevan, *Confined developable elastic surfaces: cylinders, cones and the Elastica*, presented at the Proceedings of the Royal Society of London A: Mathematical, Physical and Engineering Sciences, 2005, pp. 671-700.

29 Marcelo A Dias and Christian D Santangelo, 2012. The shape and mechanics of curved-fold origami structures. *EPL (Europhysics Letters)* **100** (5), 54005.

30 Marcelo A Dias, Levi H Dudte, L Mahadevan, and Christian D Santangelo, 2012. Geometric mechanics of curved crease origami. *Physical review letters* **109** (11), 114301.

31 Shannon A Zirbel, Robert J Lang, Mark W Thomson, Deborah A Sigel, Phillip E Walkemeyer, Brian P Trease, Spencer P Magleby, and Larry L Howell, 2013. Accommodating thickness in origami-based deployable arrays. *Journal of Mechanical Design* **135** (11), 111005.

32 Tomohiro Tachi, 2011. Rigid-foldable thick origami. *Origami* **5**, 253-264.

33 Zachary Abel, Jason Cantarella, Erik D Demaine, David Eppstein, Thomas C Hull, Jason S Ku, Robert J Lang, and Tomohiro Tachi, 2015. Rigid origami vertices: conditions and forcing sets. *arXiv preprint arXiv:1507.01644*.

34 Levi H Dudte, Etienne Vouga, Tomohiro Tachi, and L Mahadevan, 2016. Programming curvature using origami tessellations. *Nature materials*, 583-588.

35 Tomohiro Tachi, *Freeform Origami Tessellations by Generalizing Resch's Patterns*, presented at the ASME 2013 International Design Engineering Technical Conferences and Computers and Information in Engineering Conference, 2013, pp. V06BT07A025-V006BT007A025.

36 ZY Wei, ZV Guo, Levi Dudte, HY Liang, and L Mahadevan, 2013. Geometric mechanics of periodic pleated origami. *Physical review letters* **110** (21), 215501.

37 Klaus-Jürgen Bathe, *Finite element procedures*. (Klaus-Jurgen Bathe, 2006).

38 Thomas C Hull, 2002. Modelling the folding of paper into three dimensions using affine transformations. *Linear Algebra and its applications* **348** (1), 273-282.

39 Thomas Hull, *Origami^{3}*. (CRC Press, 2002).

40 Mark Schenk and Simon D Guest, 2013. Geometry of Miura-folded metamaterials. *Proceedings of the National Academy of Sciences* **110** (9), 3276-3281.

41 Tomohiro Tachi, 2009. Simulation of rigid origami. *Origami* **4**, 175-187.

42 Shuodao Wang, Jianliang Xiao, Jizhou Song, Heung Cho Ko, Keh-Chih Hwang, Yonggang Huang, and John A Rogers, 2010. Mechanics of curvilinear electronics. *Soft Matter* **6** (22), 5757-5763.

43 Dae-Hyeong Kim, Jianliang Xiao, Jizhou Song, Yonggang Huang, and John A Rogers, 2010. Stretchable, curvilinear electronics based on inorganic materials. *Advanced Materials* **22** (19), 2108-2124.

44 Benoît Huyghe, Hendrik Rogier, Jan Vanfleteren, and Fabrice Axisa, 2008. Design and manufacturing of stretchable high-frequency interconnects. *IEEE Transactions on Advanced Packaging* **31** (4), 802-808.

45 Yung-Yu Hsu, Mario Gonzalez, Frederick Bossuyt, Jan Vanfleteren, and Ingrid De Wolf, 2011. Polyimide-enhanced stretchable interconnects: design, fabrication, and characterization. *IEEE Transactions on electron devices* **58** (8), 2680-2688.

46 Rak-Hwan Kim, Myung-Ho Bae, Dae Gon Kim, Huanyu Cheng, Bong Hoon Kim, Dae-Hyeong Kim, Ming Li, Jian Wu, Frank Du, and Hoon-Sik Kim, 2011. Stretchable, transparent graphene interconnects for arrays of microscale inorganic light emitting diodes on rubber substrates. *Nano letters* **11** (9), 3881-3886.

47 Mario Gonzalez, Fabrice Axisa, Mathieu Vanden Bulcke, Dominique Brosteaux, Bart Vandevelde, and Jan Vanfleteren, 2008. Design of metal interconnects for stretchable electronic circuits. *Microelectronics Reliability* **48** (6), 825-832.

48 David C Duffy, J Cooper McDonald, Olivier JA Schueller, and George M Whitesides, 1998. Rapid prototyping of microfluidic systems in poly (dimethylsiloxane). *Analytical chemistry* **70** (23), 4974-4984.

49 Yugang Sun, Won Mook Choi, Hanqing Jiang, Yonggang Y Huang, and John A Rogers, 2006. Controlled buckling of semiconductor nanoribbons for stretchable electronics. *Nature nanotechnology* **1** (3), 201-207.

50 Zeming Song, Cheng Lv, Mengbing Liang, Varittha Sanphuang, Kedi Wu, Bin Chen, Zhi Zhao, Jing Bai, Xu Wang, John L. Volakis, Liping Wang, Ximin He, Yu Yao, Sefaattin Tongay, and Hanqing Jiang, Microscale Silicon Origami. *Submitted for pulication*.

51 Koryo Miura, 1985. Method of packaging and deployment of large membranes in space. *title The Institute of Space and Astronautical Science report* **618**, 1.

52 Sheng Xu, Zheng Yan, Kyung-In Jang, Wen Huang, Haoran Fu, Jeonghyun Kim, Zijun Wei, Matthew Flavin, Joselle McCracken, and Renhan Wang, 2015. Assembly of micro/nanomaterials into complex, three-dimensional architectures by compressive buckling. *Science* **347** (6218), 154-159.

53 Sarah-Marie Belcastro and Thomas C Hull, *A mathematical model for non-flat origami*, presented at the Origami3: Proc. the 3rd International Meeting of Origami Mathematics, Science, and Education, 2002, pp. 39-51.

54 Yihui Zhang, Zheng Yan, Kewang Nan, Dongqing Xiao, Yuhao Liu, Haiwen Luan, Haoran Fu, Xizhu Wang, Qinglin Yang, and Jiechen Wang, 2015. A mechanically driven form of Kirigami as a route to 3D mesostructures in micro/nanomembranes. *Proceedings of the National Academy of Sciences* **112** (38), 11757-11764.

55 Zheng Yan, Fan Zhang, Jiechen Wang, Fei Liu, Xuelin Guo, Kewang Nan, Qing Lin, Mingye Gao, Dongqing Xiao, and Yan Shi, 2016. Controlled Mechanical Buckling for Origami-Inspired Construction of 3D Microstructures in Advanced Materials. *Advanced Functional Materials* **26** (16), 2629-2639.

56 Ted L Anderson and TL Anderson, *Fracture mechanics: fundamentals and applications*. (CRC press, 2005).

57 J. K. Wessel, *The handbook of advanced materials: enabling new designs*. (John Wiley & Sons, 2004).

58 I Bainbridge, F. and J. A. Taylor, 2013. The Surface Tension of Pure Aluminum and Aluminum Alloys. *Metallurgical and Materials Transactions A* **44** (8), 3901-3909.

59 William D Callister, 2005. Fundamentals of materials science and engineering.

60 Jiaping Zhang, Xuanhe Zhao, Zhigang Suo, and Hanqing Jiang, 2009. A finite element method for transient analysis of concurrent large deformation and mass transport in gels. *Journal of Applied Physics* **105** (9), 093522.

61 O Coussy, J, *Poromechanics*. (Wiley & Sons, New York, 2004).

62 Wei Hong, Xuanhe Zhao, Jinxiong Zhou, and Zhigang Suo, 2008. A theory of coupled diffusion and large deformation in polymeric gels. *Journal of the Mechanics and Physics of Solids* **56** (5), 1779-1793.

63 Min Kyoo Kang and Rui Huang, 2010. A variational approach and finite element implementation for swelling of polymeric hydrogels under geometric constraints. *Journal of Applied Mechanics* **77** (6), 061004.

64 Wei Hong, Zishun Liu, and Zhigang Suo, 2009. Inhomogeneous swelling of a gel in equilibrium with a solvent and mechanical load. *International Journal of Solids and Structures* **46** (17), 3282-3289.

65 Wei Hong, Xuanhe Zhao, and Zhigang Suo, 2009. Formation of creases on the surfaces of elastomers and gels. *Applied Physics Letters* **95** (11), 111901.

66 Xiao Wang and Wei Hong, *A visco-poroelastic theory for polymeric gels*, presented at the Proc. R. Soc. A, 2012, pp. 3824-3841.

67 Shawn A Chester and Lallit Anand, 2011. A thermo-mechanically coupled theory for fluid permeation in elastomeric materials: application to thermally responsive gels. *Journal of the Mechanics and Physics of Solids* **59** (10), 1978-2006.

68 Manuel Quesada-Pérez, José Alberto Maroto-Centeno, and Alberto Martín-Molina, 2012. Effect of the counterion valence on the behavior of thermo-sensitive gels and microgels: A monte carlo simulation study. *Macromolecules* **45** (21), 8872-8879.

69 Manuel Quesada-Pérez, José Alberto Maroto-Centeno, Jacqueline Forcada, and Roque Hidalgo-Alvarez, 2011. Gel swelling theories: the classical formalism and recent approaches. *Soft Matter* **7** (22), 10536-10547.

70 Xu Wang, Wenwen Xu, Prithwish Chatterjee, Cheng Lv, John Popovich, Zeming Song, Lenore Dai, M Yashar S Kalani, Shelley E Haydel, and Hanqing Jiang, 2016. Food-Materials-Based Edible Supercapacitors. *Advanced Materials Technologies* **1** (3), 1600059.

71 Suk-Won Hwang, Hu Tao, Dae-Hyeong Kim, Huanyu Cheng, Jun-Kyul Song, Elliott Rill, Mark A Brenckle, Bruce Panilaitis, Sang Min Won, and Yun-Soung Kim, 2012. A physically transient form of silicon electronics. *Science* **337** (6102), 1640-1644.

72 Alireza Karimi, Mahdi Navidbakhsh, Hossein Yousefi, and Mansour Alizadeh, 2014. An experimental study on the elastic modulus of gelatin hydrogels using different stress–strain definitions. *Journal of Thermoplastic Composite Materials*, 0892705714533377.

73 JL Kavanagh, Thierry Menand, and Katherine A Daniels, 2013. Gelatine as a crustal analogue: Determining elastic properties for modelling magmatic intrusions. *Tectonophysics* **582**, 101-111.

APPENDIX A

CALCULATION OF DIHEDRAL ANGLE BASED ON NODAL COORDINATES-SITUATION 1

The illustration of the situation can be shown in Fig. A1:

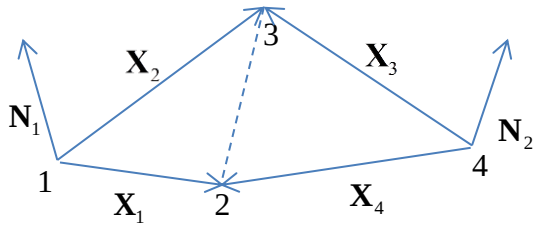

Fig. A1. The simplified model to illustrate idea of vector product applied for two adjacent faces in origami for situation 1. The vectors along edges of origami are noted as $\mathbf{X}_i$ with i changes from 1 to 4. All the vertices are numbered from 1 to 4. The normal vectors of the faces are noted as $\mathbf{N}_i$ with i changes from 1 to 2.

Firstly, the following general derivation can be obtained:

The angle between plane 1-2-3 and plane 2-3-4 is set to be α.

$$\alpha = \arccos\left(\cos\alpha\right) \tag{A1}$$

$$\cos\alpha = \frac{-\mathbf{N}_1 \cdot \mathbf{N}_2}{\left|\mathbf{N}_1\right|\left|\mathbf{N}_2\right|} \tag{A2}$$

where $\mathbf{N}_1$ and $\mathbf{N}_2$ are the normal vectors of the two adjacent faces. They can be obtained by the vector product as shown below:

$$\mathbf{N}_1 = \mathbf{X}_1 \times \mathbf{X}_2 \tag{A3}$$

$$\mathbf{N}_2 = \mathbf{X}_3 \times \mathbf{X}_4 \tag{A4}$$

where

$$\mathbf{X}_1 = \left[x_2 - x_1, y_2 - y_1, z_2 - z_1\right]$$

$$\mathbf{X}_2 = \left[x_3 - x_1, y_3 - y_1, z_3 - z_1\right]$$

$$\mathbf{X}_3 = \left[x_3 - x_4, y_3 - y_4, z_3 - z_4\right]$$

$$\mathbf{X}_4 = \left[x_2 - x_4, y_2 - y_4, z_2 - z_4 \right]$$

here x_i , y_i and z_i are the coordinates of the node i on three directions.

Then the following derivative can be obtained based on the content mentioned above:

First Derivative:

$$\frac{\partial \alpha}{\partial x_{mn}} = \frac{\partial \alpha}{\partial \cos \alpha} \frac{\partial \cos \alpha}{\partial N_{ij}} \frac{\partial N_{ij}}{\partial X_{kl}} \frac{\partial X_{kl}}{\partial x_{mn}} \tag{A5}$$

Here, it should be noted i is number of the normal vector which can change from 1 to 2, j is the direction of the normal vector which can change from 1 to 3, k is number of the in-plane vector which can change from 1 to 4, l is direction of the in-plane vector which can change from 1 to 3, m is number of the node which can change from 1 to 4, n is direction of the node which can change from 1 to 3.

Then the following is the derivation of the components of the equation above:

Part 1:

$$\frac{\partial \alpha}{\partial \cos \alpha} = -\frac{1}{\sqrt{1 - \cos^2 \alpha}} \tag{A6}$$

Part 2:

$$\frac{\partial \cos \alpha}{\partial N_{ij}}$$

For $i = 1$, the following can be obtained:

$$\frac{\partial \cos\alpha}{\partial N_{1j}} = -\frac{N_{2j}}{|\mathbf{N}_1||\mathbf{N}_2|} + \frac{N_{1j}}{|\mathbf{N}_1|^3|\mathbf{N}_2|}\mathbf{N}_1 \cdot \mathbf{N}_2 = -\frac{N_{2j}}{|\mathbf{N}_1||\mathbf{N}_2|} + \frac{N_{1j}}{|\mathbf{N}_1|^2}\cos\alpha \tag{A7}$$

For $i = 2$, the following can be obtained:

$$\frac{\partial \cos\alpha}{\partial N_{2j}} = -\frac{N_{1j}}{|\mathbf{N}_1||\mathbf{N}_2|} + \frac{N_{2j}}{|\mathbf{N}_1||\mathbf{N}_2|^3}\mathbf{N}_1 \cdot \mathbf{N}_2 = -\frac{N_{1j}}{|\mathbf{N}_1||\mathbf{N}_2|} + \frac{N_{2j}}{|\mathbf{N}_2|^2}\cos\alpha \tag{A8}$$

Part 3:

$$\frac{\partial N_{ij}}{\partial X_{kl}}$$

Using the index notation, the following can be obtained:

$$\begin{aligned} N_{1j} &= \varepsilon_{jpq} X_{1p} X_{2q} \\ \Rightarrow \frac{\partial N_{1j}}{\partial X_{1l}} &= \varepsilon_{jpq} \delta_{lp} X_{2q} \\ \Rightarrow \frac{\partial N_{1j}}{\partial X_{1l}} &= \varepsilon_{jlq} X_{2q} \end{aligned} \tag{A9}$$

So the following can be obtained:

$$\frac{\partial N_{1j}}{\partial X_{2l}} = \varepsilon_{jpl} X_{1p}$$

$$\frac{\partial N_{2j}}{\partial X_{3l}} = \varepsilon_{jlq} X_{4q}$$

$$\frac{\partial N_{2j}}{\partial X_{4l}} = \varepsilon_{jpl} X_{3p}$$

If $i = 1,\ k \neq 1,2$ or $i = 2,\ \mathrm{k} \neq 3,4$,

$$\frac{\partial N_{ij}}{\partial X_{kl}} = 0$$

Part 4:

$$\frac{\partial X_{kl}}{\partial x_{mn}}$$

If $n \neq l$, then $\frac{\partial X_{kl}}{\partial x_{mn}} = 0$.

If $n = l$, then, for $k = 1$, if $m = 1$, $\frac{\partial X_{kl}}{\partial x_{mn}} = -1$, if $m = 2$, $\frac{\partial X_{kl}}{\partial x_{mn}} = 1$

for $k = 2$, if $m = 1$, $\frac{\partial X_{kl}}{\partial x_{mn}} = -1$, if $m = 3$, $\frac{\partial X_{kl}}{\partial x_{mn}} = 1$

for $k = 3$, if $m = 4$, $\frac{\partial X_{kl}}{\partial x_{mn}} = -1$, if $m = 3$, $\frac{\partial X_{kl}}{\partial x_{mn}} = 1$

for $k = 4$, if $m = 4$, $\frac{\partial X_{kl}}{\partial x_{mn}} = -1$, if $m = 2$, $\frac{\partial X_{kl}}{\partial x_{mn}} = 1$

In the rest situation, $\frac{\partial X_{kl}}{\partial x_{mn}} = 0$.

Second Derivative

$$\frac{\partial^2\alpha}{\partial x_{1m}\partial x_{np}}=\frac{\partial^2\alpha}{\partial\cos\alpha^2}\left(\frac{\partial\cos\alpha}{\partial N_{ij}}\frac{\partial N_{ij}}{\partial X_{kl}}\frac{\partial X_{kl}}{\partial x_{1m}}\right)\left(\frac{\partial\cos\alpha}{\partial N_{uv}}\frac{\partial N_{uv}}{\partial X_{xy}}\frac{\partial X_{xy}}{\partial x_{np}}\right)$$
$$+\frac{\partial\alpha}{\partial\cos\alpha}\left(\frac{\partial^2\cos\alpha}{\partial N_{ij}\partial N_{uv}}\frac{\partial N_{ij}}{\partial X_{kl}}\frac{\partial X_{kl}}{\partial x_{1m}}\frac{\partial N_{uv}}{\partial X_{xy}}\frac{\partial X_{xy}}{\partial x_{np}}\right)$$
$$+\frac{\partial\alpha}{\partial\cos\alpha}\left(\frac{\partial\cos\alpha}{\partial N_{ij}}\frac{\partial^2 N_{ij}}{\partial X_{kl}\partial X_{uv}}\frac{\partial X_{kl}}{\partial x_{1m}}\frac{\partial X_{uv}}{\partial x_{np}}\right) \tag{A10}$$
$$+\frac{\partial\alpha}{\partial\cos\alpha}\left(\frac{\partial\cos\alpha}{\partial N_{ij}}\frac{\partial N_{ij}}{\partial X_{kl}}\frac{\partial^2 X_{kl}}{\partial x_{1m}\partial x_{np}}\right)$$

Here, it should be noted i and u are from 1 to 2, j and v are from 1 to 3, k and x are from 1 to 4, l and y are from 1 to 3, n is from 1 to 4, m and p are from 1 to 3.

Then the following is the derivation of some of the components of the equation above:

Part 1:

$$\frac{\partial^2\alpha}{\partial\cos\alpha^2}=-\frac{\cos\alpha}{\left(1-\cos^2\alpha\right)^{3/2}} \tag{A11}$$

Part 2:

$$\frac{\partial^2\cos\alpha}{\partial N_{ij}\partial N_{uv}}$$

For $i=1$ and $u=1$, the following can be obtained:

$$\frac{\partial^2\cos\alpha}{\partial N_{1j}\partial N_{1v}}=\frac{N_{2j}N_{1v}}{\left|\mathbf{N}_1\right|^3\left|\mathbf{N}_2\right|}+\frac{\delta_{jv}}{\left|\mathbf{N}_1\right|^3\left|\mathbf{N}_2\right|}\mathbf{N}_1\cdot\mathbf{N}_2+\frac{N_{1j}N_{2v}}{\left|\mathbf{N}_1\right|^3\left|\mathbf{N}_2\right|}-3\frac{N_{1j}N_{1v}}{\left|\mathbf{N}_1\right|^5\left|\mathbf{N}_2\right|}\mathbf{N}_1\cdot\mathbf{N}_2$$
$$=\frac{N_{2j}N_{1v}}{\left|\mathbf{N}_1\right|^3\left|\mathbf{N}_2\right|}-\frac{\delta_{jv}}{\left|\mathbf{N}_1\right|^2}\cos\alpha+\frac{N_{1j}N_{2v}}{\left|\mathbf{N}_1\right|^3\left|\mathbf{N}_2\right|}+3\frac{N_{1j}N_{1v}}{\left|\mathbf{N}_1\right|^4}\cos\alpha \tag{A12}$$

For $i=1$ and $u=2$, the following can be obtained:

$$\begin{aligned}\frac{\partial^2 \cos\alpha}{\partial N_{1j}\partial N_{2v}} &= -\frac{\delta_{jv}}{|\mathbf{N}_1||\mathbf{N}_2|}+\frac{N_{2j}N_{2v}}{|\mathbf{N}_1||\mathbf{N}_2|^3}-\frac{N_{1j}N_{2v}}{|\mathbf{N}_1|^3|\mathbf{N}_2|^3}\mathbf{N}_1\cdot\mathbf{N}_2+\frac{N_{1j}N_{1v}}{|\mathbf{N}_1|^3|\mathbf{N}_2|} \\ &= -\frac{\delta_{jv}}{|\mathbf{N}_1||\mathbf{N}_2|}+\frac{N_{2j}N_{2v}}{|\mathbf{N}_1||\mathbf{N}_2|^3}+\frac{N_{1j}N_{2v}}{|\mathbf{N}_1|^2|\mathbf{N}_2|^2}\cos\alpha+\frac{N_{1j}N_{1v}}{|\mathbf{N}_1|^3|\mathbf{N}_2|}\end{aligned} \tag{A13}$$

For $i=2$ and $u=1$, the following can be obtained:

$$\begin{aligned}\frac{\partial^2 \cos\alpha}{\partial N_{2j}\partial N_{1v}} &= -\frac{\delta_{jv}}{|\mathbf{N}_1||\mathbf{N}_2|}+\frac{N_{1j}N_{1v}}{|\mathbf{N}_1|^3|\mathbf{N}_2|}-\frac{N_{2j}N_{1v}}{|\mathbf{N}_1|^3|\mathbf{N}_2|^3}\mathbf{N}_1\cdot\mathbf{N}_2+\frac{N_{2j}N_{2v}}{|\mathbf{N}_1||\mathbf{N}_2|^3} \\ &= -\frac{\delta_{jv}}{|\mathbf{N}_1||\mathbf{N}_2|}+\frac{N_{1j}N_{1v}}{|\mathbf{N}_1|^3|\mathbf{N}_2|}+\frac{N_{2j}N_{1v}}{|\mathbf{N}_1|^2|\mathbf{N}_2|^2}\cos\alpha+\frac{N_{2j}N_{2v}}{|\mathbf{N}_1||\mathbf{N}_2|^3}\end{aligned} \tag{A14}$$

For $i=2$ and $u=2$, the following can be obtained:

$$\begin{aligned}\frac{\partial^2 \cos\alpha}{\partial N_{2j}\partial N_{2v}} &= \frac{N_{1j}N_{2v}}{|\mathbf{N}_1||\mathbf{N}_2|^3}+\frac{\delta_{jv}}{|\mathbf{N}_1||\mathbf{N}_2|^3}\mathbf{N}_1\cdot\mathbf{N}_2+\frac{N_{2j}N_{1v}}{|\mathbf{N}_1||\mathbf{N}_2|^3}-3\frac{N_{2j}N_{2v}}{|\mathbf{N}_1||\mathbf{N}_2|^5}\mathbf{N}_1\cdot\mathbf{N}_2 \\ &= \frac{N_{1j}N_{2v}}{|\mathbf{N}_1||\mathbf{N}_2|^3}-\frac{\delta_{jv}}{|\mathbf{N}_2|^2}\cos\alpha+\frac{N_{2j}N_{1v}}{|\mathbf{N}_1||\mathbf{N}_2|^3}+3\frac{N_{2j}N_{2v}}{|\mathbf{N}_2|^4}\cos\alpha\end{aligned} \tag{A15}$$

Part 3:

$$\frac{\partial^2 N_{ij}}{\partial X_{kl}\partial X_{uv}}$$

Using the previous conclusion for $\frac{\partial N_{ij}}{\partial X_{kl}}$, the following can be obtained by using the index notation:

$$\frac{\partial^2 N_{1j}}{\partial X_{1l}\partial X_{2v}} = \varepsilon_{jlq}\delta_{qv} = \varepsilon_{jlv} \tag{A16}$$

So the following can be obtained:

$$\frac{\partial^2 N_{1j}}{\partial X_{2l}\partial X_{1v}} = \varepsilon_{jpl}\delta_{pv} = \varepsilon_{jvl}$$

$$\frac{\partial^2 N_{2j}}{\partial X_{3l}\partial X_{4v}} = \varepsilon_{jlq}\delta_{qv} = \varepsilon_{jlv}$$

$$\frac{\partial^2 N_{2j}}{\partial X_{4l}\partial X_{3v}} = \varepsilon_{jpl}\delta_{pv} = \varepsilon_{jvl}$$

For other situation, $\frac{\partial^2 N_{ij}}{\partial X_{kl}\partial X_{uv}} = 0$

Part 4:

$$\frac{\partial^2 X_{kl}}{\partial x_{1m}\partial x_{np}} = 0 \qquad \text{(A17)}$$

APPENDIX B

CALCULATION OF DIHEDRAL ANGLE BASED ON NODAL COORDINATES-SITUATION 2

The situation can be shown in Fig. A2:

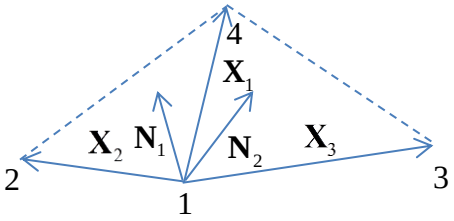

Fig. A2. The simplified model to illustrate idea of vector product applied for two adjacent faces in origami for situation 1. The vectors along edges of origami is are noted as $\mathbf{X}_i$ with i changes from 1 to 3. All the vertices are numbered from 1 to 4. The normal vectors of the faces are noted as $\mathbf{N}_i$ with i changes from 1 to 2.

Firstly, the following general derivation should clear:

The angle between plane 1-2-4 and plane 1-3-4 is set to be α.

$$\alpha = \arccos\left(\cos\alpha\right) \tag{A18}$$

$$\cos\alpha = \frac{-\mathbf{N}_1 \cdot \mathbf{N}_2}{\left|\mathbf{N}_1\right|\left|\mathbf{N}_2\right|} \tag{A19}$$

$$\mathbf{N}_1 = \mathbf{X}_1 \times \mathbf{X}_2 \tag{A20}$$

$$\mathbf{N}_2 = \mathbf{X}_3 \times \mathbf{X}_1 \tag{A21}$$

where

$$\mathbf{X}_1 = \left[x_4 - x_1, y_4 - y_1, z_4 - z_1\right]$$

$$\mathbf{X}_2 = \left[x_2 - x_1, y_2 - y_1, z_2 - z_1\right]$$

$$\mathbf{X}_3 = \left[x_3 - x_1, y_3 - y_1, z_3 - z_1\right]$$

Then the rest of derivations are similar to the ones above.

APPENDIX C

CALCULATE DERIVATIVES OF ENERGY FOR SPRING ELEMENT OF NFEM

In the SUBROUTINE, I need to define $\frac{\partial r}{\partial x_i}$ and $\frac{\partial^2 r}{\partial x_i \partial x_j}$.

Note here, x_i can be $x_1, y_1, z_1, x_2, y_2, z_2$

As the distance between two adjacent nodes is:

$$r = \sqrt{(x_1 - x_2)^2 + (y_1 - y_2)^2 + (z_1 - z_2)^2} \tag{A22}$$

In the program, the definitions of DR1 and DDR2 will be necessary. And it is clear that taking the derivative with respect to a coordinate of node "2" will have a negative sign before the derivative with respect to the same coordinate of node "1", *i.e.* $\frac{\partial r}{\partial x_2} = -\frac{\partial r}{\partial x_1}$.

And the following can be obtained as an example for the general case:

$$\begin{aligned}
\frac{\partial r}{\partial x_1} &= \frac{\partial}{\partial x_1}\left(\sqrt{(x_1 - x_2)^2 + (y_1 - y_2)^2 + (z_1 - z_2)^2}\right) \\
&= \frac{1}{2}\frac{1}{\sqrt{(x_1 - x_2)^2 + (y_1 - y_2)^2 + (z_1 - z_2)^2}} 2(x_1 - x_2) \\
&= \frac{(x_1 - x_2)}{\sqrt{(x_1 - x_2)^2 + (y_1 - y_2)^2 + (z_1 - z_2)^2}} \\
&= \frac{(x_1 - x_2)}{r}
\end{aligned} \tag{A23}$$

For the second derivative, two different cases exist. One is the derivative with respect to two different coordinate and the other is the one with respect two same coordinate. The following are the two examples for the two cases:

$$\begin{aligned}\frac{\partial^2 r}{\partial x_1^2} &= \frac{\partial}{\partial x_1}\left(\frac{x_1 - x_2}{r}\right) \\ &= \frac{1}{r} - \left(x_1 - x_2\right)\frac{1}{r^2}\frac{\partial r}{\partial x_1} \\ &= \frac{1}{r} - \left(x_1 - x_2\right)\frac{1}{r^2}\frac{x_1 - x_2}{r} \\ &= \frac{1}{r} - \left(x_1 - x_2\right)^2\frac{1}{r^3}\end{aligned} \tag{A24}$$

$$\begin{aligned}\frac{\partial^2 r}{\partial x_1 \partial y_1} &= \frac{\partial}{\partial y_1}\left(\frac{x_1 - x_2}{r}\right) \\ &= -\left(x_1 - x_2\right)\frac{1}{r^2}\frac{\partial r}{\partial y_1} \\ &= -\left(x_1 - x_2\right)\frac{1}{r^2}\frac{y_1 - y_2}{r} \\ &= -\left(x_1 - x_2\right)\left(y_1 - y_2\right)\frac{1}{r^3}\end{aligned} \tag{A25}$$

And the examples of the derivative of the energy can be shown as followed:

First derivative:

$$\begin{aligned}\frac{\partial V}{\partial x_1} &= \frac{\partial}{\partial x_1}\left(\frac{1}{2}k\left(r - r_0\right)^2\right) \\ &= k\left(r - r_0\right)\frac{\partial r}{\partial x_1} \\ &= k\left(r - r_0\right)\frac{\left(x_1 - x_2\right)}{r} \\ &= DR1 \cdot \left(x_1 - x_2\right)\end{aligned} \tag{A26}$$

Second derivative:

$$\begin{aligned}
\frac{\partial^2 V}{\partial x_1^2} &= \frac{\partial}{\partial x_1}\left[k\left(r-r_0\right)\frac{\partial r}{\partial x_1}\right] \\
&= k\left(\frac{\partial r}{\partial x_1}\right)^2 + k\left(r-r_0\right)\frac{\partial^2 r}{\partial x_1^2} \\
&= k\frac{\left(x_1-x_2\right)^2}{r^2} + k\left(r-r_0\right)\left[\frac{1}{r} - \left(x_1-x_2\right)^2\frac{1}{r^3}\right] \\
&= \frac{k\left(r-r_0\right)}{r} + kr_0\left(x_1-x_2\right)^2\frac{1}{r^3} \\
&= DR1 + DDR2\left(x_1-x_2\right)^2
\end{aligned} \tag{A27}$$

$$\begin{aligned}
\frac{\partial^2 V}{\partial x_1 \partial y_1} &= \frac{\partial}{\partial y_1}\left[k\left(r-r_0\right)\frac{\partial r}{\partial x_1}\right] \\
&= k\frac{\partial r}{\partial x_1}\frac{\partial r}{\partial y_1} + k\left(r-r_0\right)\frac{\partial^2 r}{\partial x_1 \partial y_1} \\
&= k\frac{\left(x_1-x_2\right)\left(y_1-y_2\right)}{r^2} + k\left(r-r_0\right)\left[-\left(x_1-x_2\right)\left(y_1-y_2\right)\frac{1}{r^3}\right] \\
&= kr_0\left(x_1-x_2\right)\left(y_1-y_2\right)\frac{1}{r^3} \\
&= DDR2\left(x_1-x_2\right)\left(y_1-y_2\right)
\end{aligned} \tag{A28}$$

APPENDIX D

NUMBER OF TYPE 1 AND TYPE 2 ELEMENT FOR NFEM

As shown in Fig. A3, different element types are defined according to the different connection of nodes. For each of element, nodes are numbered from 1 to 13. Different stiffness values are given to the rotational springs along creases according to the different kind of dihedral angles. For each of the situation and the corresponding stiffness value, the numbers of the necessary nodes to determine the corresponding dihedral angle are summarized on the right side of each figure. This number rules will be very useful for the development of UEL for NFEM.

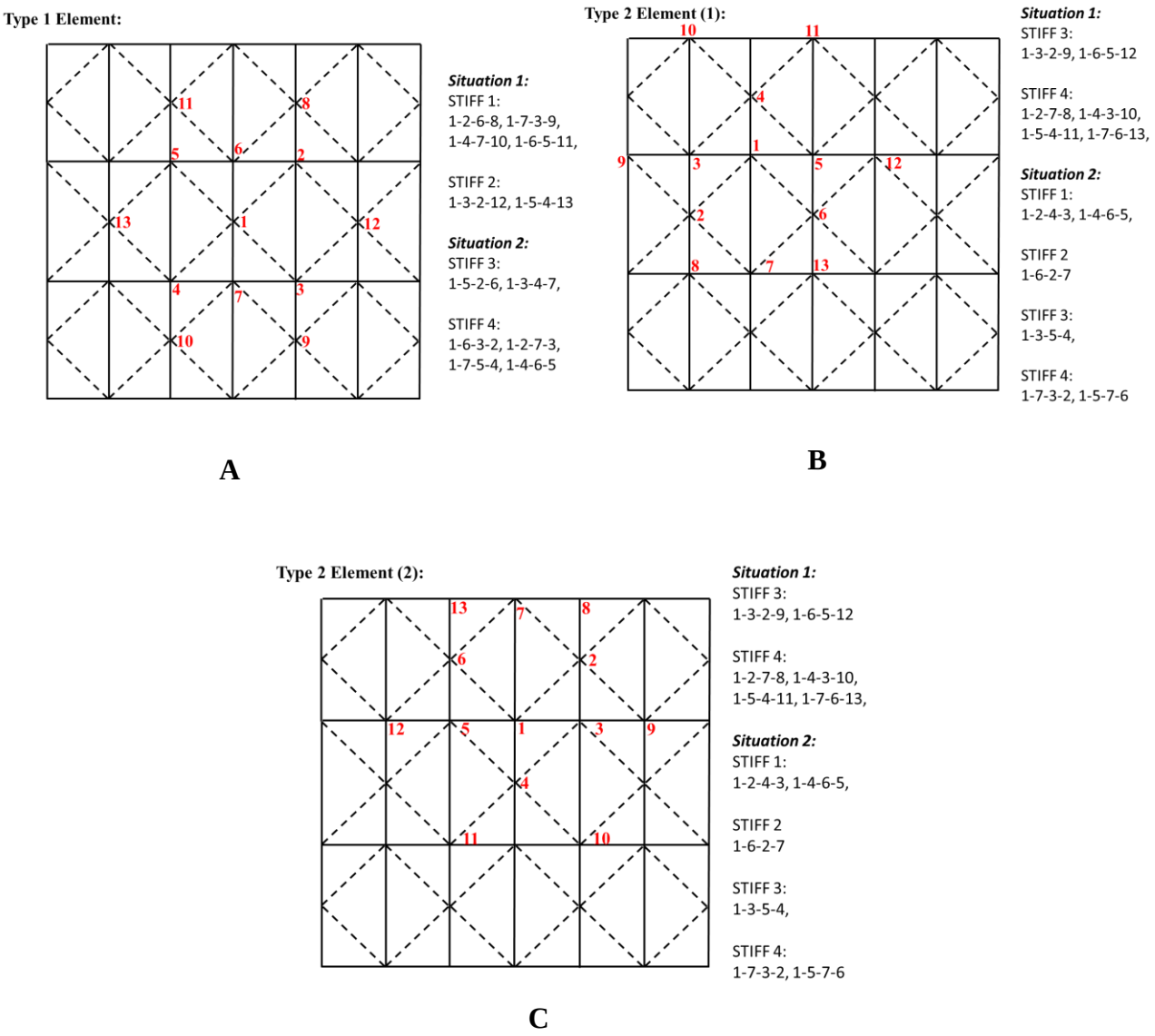

Fig. A3. Water bomb crease pattern with definitions of different NFEM element types. (**A**) For element type 1. (**B**) For element type 2 (1). (**C**) For element type 2 (2). Here the latter two types of element only have difference on their directions. The red numbers shows the local nodal number in each element. Each kind of stiffness value is assigned according to the geometry of the involved faces. Dash lines indicate valley creases and solid lines indicate mountain creases.

APPENDIX E

NFEM USER SUBROUTINE UEL FOR WATER BOMB SIMULATION

```
CCCCCCCCCCCCCCCCCCCCCCCCCCCCCCCCCCCCCCCCCCCCCCCCCCCCCCCCCCCCCCCCCCCCCCCCCC
C     SUBROUTINE USED TO DEFINE NFEM ELEMENT PROPERTY
CCCCCCCCCCCCCCCCCCCCCCCCCCCCCCCCCCCCCCCCCCCCCCCCCCCCCCCCCCCCCCCCCCCCCCCCCC
      SUBROUTINE UEL(RHS,AMATRX,SVARS,ENERGY,NDOFEL,NRHS,NSVARS,
     1 PROPS,NPROPS,COORDS,MCRD,NNODE,U,DU,V,A,JTYPE,TIME,DTIME,
     2 KSTEP,KINC,JELEM,PARAMS,NDLOAD,JDLTYP,ADLMAG,PREDEF,NPREDF,
     3 LFLAGS,MLVARX,DDLMAG,MDLOAD,PNEWDT,JPROPS,NJPROP,PERIOD)
C
C**********************************************************************
C     The description of unit:
C     energy : 10^(-3) J=1N*1mm
C     length : 1 mm
C     force  : 1 N
C**********************************************************************
       IMPLICIT DOUBLE PRECISION (A-H, O-Z)
       PARAMETER ( NTOTPART = 480, NTOTEL = 1408)
        DIMENSION RHS(MLVARX,*),AMATRX(NDOFEL,NDOFEL),PROPS(*),
     1 SVARS(NSVARS),ENERGY(8),COORDS(MCRD,NNODE),U(NDOFEL),
     2 DU(MLVARX,*),V(NDOFEL),A(NDOFEL),TIME(2),PARAMS(*),
     3 JDLTYP(MDLOAD,*),ADLMAG(MDLOAD,*),DDLMAG(MDLOAD,*),
     4 PREDEF(2,NPREDF,NNODE),LFLAGS(*),JPROPS(*)
C-----  The above is the standard input in the USER-ELEMENT in ABAQUS.
C**********************ELEMENT USER VARIABLE**********************
C NODEL=39:number of degree of freedom in the element
C NRHS=1
C MCRD=3
C NNODE=13: number of nodes on the element
C NTOTPART: total vertices for simulation
C NTOTEL  : total number of elements for simulation

        REAL*8 EX(13,3),EK(39,39),EF(3)
        REAL*8 SPRINGEX(2,3),SPRINGEX0(2,3),SPRINGEK(6,6),SPRINGEF(6)
        DIMENSION ANGLE_SUB(2,1256,4,6)
        INTEGER NELE(13),NRANGE
        COMMON ITIME,ICALL
        COMMON ETTOT,ESPR
        COMMON ANGLE(2,1256,4,6)
        REAL*8 MASS

C----- NRANGE  : the number of node in a row of mesh
C----- EX  : the coordinates of current increment for this element
C----- EK  : stiffness matrix. The left-top 3*3 is the stiffness of
center vertex, and the 3*27 and 27*3 have be divided by 2 because the
C other half contribution comes from another elements.
C      EK = partial ^2 energy / partial (x) partial (x)
C----- EF  : force due to the unequilibrium vertex postions.
C      EF = partial energy / partial (x)
C----- NELE : local vertex array. The arrangement refers to the
drawing.
C      NELE(1) = 1 always
C      If else is 1, say, NELE(j) =1, then that means there is no
vertex.
```

```
C      ITIME : identifier to initiate energy and used to check if
current iteraction should end.
C      ICALL : identifier to indicate if it is first iteration.

         OPEN(2000, FILE='D:\ASUchenglv\Origami\Magic_Ball\Deformation\
     &coors.TXT')
         OPEN(105, FILE='D:\ASUchenglv\Origami\Magic_Ball\Deformation\
     &energy.dat')
        OPEN(6000, FILE='D:\ASUchenglv\Origami\Magic_Ball\warning.dat')
         OPEN(4000,
FILE='D:\ASUchenglv\Origami\Magic_Ball\eq_angle.dat')
C       Create file coor.txt to store the current coordinates of every
C       node. Create file energy.txt to store the total energys of the
C       whole model. Create file warning.dat to check the large
C       deformation of linear spring element. Read file eq_angle.dat to
C       obtain the equilibrium angles of evergy dihedral angle.

C*********************************************************************
C       Read equilibrium values for every dihedral angle
C*********************************************************************
        IF(ICALL.EQ.0) THEN
          DO I=1,3904
            READ(4000,*) N1,N2,N3,N4,ANGLE_EQ
                ANGLE(N1,N2,N3,N4)=ANGLE_EQ
          ENDDO
        ENDIF

C*********************************************************************
C       Initiate values
C*********************************************************************
        ANGLE_SUB=ANGLE
        ICALL=1
        AMATRX = 0.D0
        MASS = 1.D0
        ADJUST_K = 0.d0
        NRANGE = 32
        IF(ITIME.EQ.0) THEN
          ETTOT = 0.D0
          ESPR = 0.D0
        ENDIF
        DO K1 = 1,NDOFEL
          DO KRHS = 1,NRHS
                  RHS(K1,KRHS) = 0.D0
          ENDDO
        ENDDO

C*********************************************************************
C*********************************************************************
C       Loop for the first element type
C*********************************************************************
C*********************************************************************
        IF (JTYPE.EQ.1) THEN
```

```
C*********************************************************************
C       Update coordinates
C*********************************************************************
          DO INODE = 1,NNODE
                DO IMCRD = 1,MCRD
                  IPOSN = 3*(INODE-1)+IMCRD
                  EX(INODE,IMCRD) = COORDS(IMCRD,INODE)+U(IPOSN)
                ENDDO
          ENDDO

C*********************************************************************
C       Loop to decide whether the node exist or not
C*********************************************************************
          NELE = 1      !initiate NELE array
          DO INODE = 2,NNODE
                DIS = DSQRT((EX(INODE,1)-EX(1,1))**2.DO
     &             +(EX(INODE,2)-EX(1,2))**2.DO+(EX(INODE,3)-
EX(1,3))**2.DO)
                IF (DIS.LT.1.D-7) THEN
                  NELE(INODE) = 1
                ELSE
                  NELE(INODE) = INODE
                ENDIF
          ENDDO

C*********************************************************************
C       Update EK and EF
C*********************************************************************
          CALL CALEMEF(EX,NELE,EK,EF,ETTOT,JELEM,JTYPE,ANGLE_SUB)

        ENDIF
C*********************************************************************
C*********************************************************************
C       End loop for the first element type
C*********************************************************************
C*********************************************************************


C*********************************************************************
C*********************************************************************
C       Loop for the second element type
C*********************************************************************
C*********************************************************************
        IF (JTYPE.EQ.2) THEN

C*********************************************************************
C       Update coordinates
C*********************************************************************
          DO INODE = 1,NNODE
                DO IMCRD = 1,MCRD
                  IPOSN = 3*(INODE-1)+IMCRD
```

```
                  EX(INODE,IMCRD) = COORDS(IMCRD,INODE)+U(IPOSN)
                ENDDO
            ENDDO

C*********************************************************************
C       Loop to decide whether the node exist or not
C*********************************************************************
            NELE = 1      !initiate NELE array
            DO INODE = 2,NNODE
                  DIS = DSQRT((EX(INODE,1)-EX(1,1))**2.DO
     &               +(EX(INODE,2)-EX(1,2))**2.DO+(EX(INODE,3)-
EX(1,3))**2.DO)
                  IF (DIS.LT.1.D-7) THEN
                    NELE(INODE) = 1
                  ELSE
                    NELE(INODE) = INODE
                  ENDIF
            ENDDO

C*********************************************************************
C       Update EK, EF and ETTOT
C*********************************************************************
            CALL CALEMEF(EX,NELE,EK,EF,ETTOT,JELEM,JTYPE,ANGLE_SUB)

          ENDIF
C*********************************************************************
C*********************************************************************
C       End loop for the second element type
C*********************************************************************
C*********************************************************************


C*********************************************************************
C*********************************************************************
C       Loop for the third, fourth and fifth element type
C*********************************************************************
C*********************************************************************
          IF (JTYPE.EQ.3.OR.JTYPE.EQ.4.OR.JTYPE.EQ.5)THEN

C*********************************************************************
C       Update coordinates
C*********************************************************************
              DO INODE = 1,NNODE
                DO IMCRD = 1,MCRD
                    IPOSN = IMCRD+3*(INODE-1)
                    SPRINGEX(INODE,IMCRD) = COORDS(IMCRD,INODE)+U(IPOSN)
                    SPRINGEXO(INODE,IMCRD) = COORDS(IMCRD,INODE)
                ENDDO
              ENDDO

C*********************************************************************
C       Update SPRINGEK, SPRINGEF and ESPR
```

```
C*********************************************************************
            CALL
SPRINGEMEF(JTYPE,SPRINGEX,SPRINGEXO,SPRINGEK,SPRINGEF,ESPR,
     &            jelem)

        ENDIF
C*********************************************************************
C*********************************************************************
C       End loop for the third, fourth and fifth element type
C*********************************************************************
C*********************************************************************

C*********************************************************************
C*********************************************************************
C       For static analysis
C*********************************************************************
C*********************************************************************
        IF (LFLAGS(1).EQ.1.OR.LFLAGS(1).EQ.2) THEN

C*********************************************************************
C       Assign value to RHS and AMATRIX for the first element type
C*********************************************************************
           IF (JTYPE.EQ.1) THEN
             RHS(1,1) = -EF(1)     !3 translational degrees of freedom
             RHS(2,1) = -EF(2)
             RHS(3,1) = -EF(3)
             DO K1 = 1,NDOFEL
                 DO K2 = 1,NDOFEL
                   AMATRX(K2,K1) = EK(K2,K1)
                 ENDDO
             ENDDO

C*********************************************************************
C       Add adjust factor to AMATRIX to help converge
C*********************************************************************
              amatrx(1,1) = amatrx(1,1) + ADJUST_K
              amatrx(2,2) = amatrx(2,2) + ADJUST_K
              amatrx(3,3) = amatrx(3,3) + ADJUST_K

C*********************************************************************
C       Output current coordinates to file coor.txt
C*********************************************************************
              WRITE(2000,2000) JELEM,EX(1,1),EX(1,2),EX(1,3)
2000          FORMAT(I8,',',f30.20,',',f30.20,',',f30.20)
           ENDIF

C*********************************************************************
C       Assign value to RHS and AMATRIX for the second element type
C*********************************************************************
           IF(JTYPE.EQ.2) THEN
             RHS(1,1) = -EF(1)     !3 translational degrees of freedom
             RHS(2,1) = -EF(2)
```

```
              RHS(3,1) = -EF(3)
              DO K1 = 1,NDOFEL
                  DO K2 = 1,NDOFEL
                    AMATRX(K2,K1) = EK(K2,K1)
                  ENDDO
              ENDDO

C**********************************************************************
C       Add adjust factor to AMATRIX to help converge
C**********************************************************************
              amatrx(1,1) = amatrx(1,1) + ADJUST_K
              amatrx(2,2) = amatrx(2,2) + ADJUST_K
              amatrx(3,3) = amatrx(3,3) + ADJUST_K

C**********************************************************************
C       Output current coordinates to file coor.txt
C**********************************************************************
                WRITE(2000,2000) JELEM,EX(1,1),EX(1,2),EX(1,3)
            ENDIF

C**********************************************************************
C       Assign value to RHS and AMATRIX for the third, fourth and fifth
C       element type
C**********************************************************************
            IF(JTYPE.EQ.3.OR.JTYPE.EQ.4.OR.JTYPE.EQ.5) THEN
              RHS(1,1) = -SPRINGEF(1)
              RHS(2,1) = -SPRINGEF(2) !6 degrees of freedom
              RHS(3,1) = -SPRINGEF(3) !(3 translational + 3 rotational)
              RHS(4,1) = -SPRINGEF(4)
              RHS(5,1) = -SPRINGEF(5)
              RHS(6,1) = -SPRINGEF(6)
              DO K1 = 1,NDOFEL
                  DO K2 = 1,NDOFEL
                    AMATRX(K2,K1) = SPRINGEK(K2,K1)
                  ENDDO
              ENDDO
            ENDIF
        ENDIF
C**********************************************************************
C**********************************************************************
C       End for static analysis
C**********************************************************************
C**********************************************************************


C**********************************************************************
C**********************************************************************
C       For eigenvalue analysis
C**********************************************************************
C**********************************************************************
        IF(LFLAGS(1).EQ.41) THEN
```

```
C***********************************************************************
C       Define current stiffness matrix AMATRIX
C***********************************************************************
            IF(LFLAGS(3).EQ.2) THEN
              IF(JTYPE.EQ.1) THEN
                  DO K1=1,NDOFEL
                    DO K2=1,NDOFEL
                        AMATRX(K2,K1)=EK(K2,K1)
                    ENDDO
                  ENDDO
              ENDIF
              IF(JTYPE.EQ.2) THEN
                  DO K1=1,NDOFEL
                    DO K2=1,NDOFEL
                        AMATRX(K2,K1)=SPRINGEK(K2,K1)
                    ENDDO
                ENDDO
              ENDIF
            ENDIF

C***********************************************************************
C       Define current mass matrix AMATRIX
C***********************************************************************
            IF(LFLAGS(3).EQ.4) THEN
              IF(JTYPE.EQ.1) THEN
                  DO K1=1,3
                    AMATRX(K1,K1)=MASS
                  ENDDO
              ENDIF
              IF(JTYPE.EQ.2) THEN
                  DO K1=1,NDOFEL
                    AMATRX(K1,K1)=MASS
                  ENDDO
              ENDIF
            ENDIF

        ENDIF
C***********************************************************************
C***********************************************************************
C       End for eigenvalue analysis
C***********************************************************************
C***********************************************************************


C***********************************************************************
C       Operation at the end of each iteration
C***********************************************************************
        ITIME=ITIME+1
        IF(ITIME.EQ.NTOTEL) THEN     !marks completion of 1 loadstep
            WRITE(105,*) ETTOT,ESPR  !total energys written in the file
            ITIME=0
            REWIND(2000)             !coors and warning are rewound
```

```
            REWIND(6000)
          ENDIF


          RETURN
          END
CCCCCCCCCCCCCCCCCCCCCCCCCCCCCCCCCCCCCCCCCCCCCCCCCCCCCCCCCCCCCCCCCCCCCCCCCCCCCCC


CCCCCCCCCCCCCCCCCCCCCCCCCCCCCCCCCCCCCCCCCCCCCCCCCCCCCCCCCCCCCCCCCCCCCCCCCCCCCCC
C     SUBROUTINE USED TO DEFINE PROPERTY FOR LINEAR SPRING ELEMENT
CCCCCCCCCCCCCCCCCCCCCCCCCCCCCCCCCCCCCCCCCCCCCCCCCCCCCCCCCCCCCCCCCCCCCCCCCCCCCCC
      SUBROUTINE SPRINGEMEF(JTYPE,SPRINGEX,SPRINGEXO,SPRINGEK,SPRINGEF
     &      ,ESPR,NEE)
C*********************************************************************
C     FUNCTION:
C     INPUT:
C       BY ENTRANCE:SPRINGEX(2,3),SPRINGEXO(2,3),JTYPE,NEE
C     OUTPUT:
C       BY EXIT:SPRINGEK(6,6),SPRINGEF(6),ESPR
C*********************************************************************

       IMPLICIT DOUBLE PRECISION (A-H, O-Z)
         REAL*8 SPRINGEX(2,3),SPRINGEXO(2,3),SPRINGEK(6,6),SPRINGEF(6)

         STIFF=1.0D4   !Stiffness of spring element

         X1=SPRINGEX(1,1)
         Y1=SPRINGEX(1,2)
         Z1=SPRINGEX(1,3)
         X2=SPRINGEX(2,1)
         Y2=SPRINGEX(2,2)
         Z2=SPRINGEX(2,3)

C*********************************************************************
C        Decide the equilibrium length of spring element
C*********************************************************************
         R=DSQRT((X2-X1)**2.D0+(Y2-Y1)**2.D0+(Z2-Z1)**2.D0)
         IF(JTYPE.EQ.3) THEN
           R0=1.0D1
         ELSEIF(JTYPE.EQ.4) THEN
           R0=DSQRT(2.D0)*1.0D1
         ELSEIF(JTYPE.EQ.5) THEN
           R0=2.0D1
         ENDIF

C*********************************************************************
C        Calculate ESPR. And calculate DR1, DDR2 which are useful to
C        calculate first and second derivative of R with respective to x
C*********************************************************************
         ESPR=ESPR+0.5D0*STIFF*(R-R0)**2.D0
         DR1=STIFF*(1.D0-R0/R)
```

```
        DDR2=STIFF*R0/R**3.D0

C***********************************************************************
C       Check if the length change of the spring element more than 0.1%
C***********************************************************************
        IF(DABS(((R-R0)/R0)*100).GE.0.1) THEN
          WRITE(6000,*) NEE,R,((R-R0)/R0)*100
        ENDIF

C***********************************************************************
C       Calculate SPRINGEF and SPRINGEK, see details in APPENDIX C
C***********************************************************************
        SPRINGEF(1)=DR1*(X1-X2)
        SPRINGEF(2)=DR1*(Y1-Y2)
        SPRINGEF(3)=DR1*(Z1-Z2)
        SPRINGEF(4)=-DR1*(X1-X2)
        SPRINGEF(5)=-DR1*(Y1-Y2)
        SPRINGEF(6)=-DR1*(Z1-Z2)

        SPRINGEK(1,1)=DDR2*(X1-X2)*(X1-X2)+DR1
        SPRINGEK(1,2)=DDR2*(X1-X2)*(Y1-Y2)
        SPRINGEK(1,3)=DDR2*(X1-X2)*(Z1-Z2)
        SPRINGEK(1,4)=-SPRINGEK(1,1)
        SPRINGEK(1,5)=-SPRINGEK(1,2)
        SPRINGEK(1,6)=-SPRINGEK(1,3)

        SPRINGEK(2,1)=SPRINGEK(1,2)
        SPRINGEK(2,2)=DDR2*(Y1-Y2)*(Y1-Y2)+DR1
        SPRINGEK(2,3)=DDR2*(Y1-Y2)*(Z1-Z2)
        SPRINGEK(2,4)=-SPRINGEK(2,1)
        SPRINGEK(2,5)=-SPRINGEK(2,2)
        SPRINGEK(2,6)=-SPRINGEK(2,3)

        SPRINGEK(3,1)=SPRINGEK(1,3)
        SPRINGEK(3,2)=SPRINGEK(2,3)
        SPRINGEK(3,3)=DDR2*(Z1-Z2)*(Z1-Z2)+DR1
        SPRINGEK(3,4)=-SPRINGEK(3,1)
        SPRINGEK(3,5)=-SPRINGEK(3,2)
        SPRINGEK(3,6)=-SPRINGEK(3,3)

        SPRINGEK(4,1)=SPRINGEK(1,4)   ! symmetry takes care from hereon
        SPRINGEK(4,2)=SPRINGEK(2,4)
        SPRINGEK(4,3)=SPRINGEK(3,4)
        SPRINGEK(4,4)=-SPRINGEK(4,1)
        SPRINGEK(4,5)=-SPRINGEK(4,2)
        SPRINGEK(4,6)=-SPRINGEK(4,3)

        SPRINGEK(5,1)=SPRINGEK(1,5)
        SPRINGEK(5,2)=SPRINGEK(2,5)
        SPRINGEK(5,3)=SPRINGEK(3,5)
        SPRINGEK(5,4)=-SPRINGEK(5,1)
        SPRINGEK(5,5)=-SPRINGEK(5,2)
```

```
        SPRINGEK(5,6)=-SPRINGEK(5,3)

        SPRINGEK(6,1)=SPRINGEK(1,6)
        SPRINGEK(6,2)=SPRINGEK(2,6)
        SPRINGEK(6,3)=SPRINGEK(3,6)
        SPRINGEK(6,4)=-SPRINGEK(6,1)
        SPRINGEK(6,5)=-SPRINGEK(6,2)
        SPRINGEK(6,6)=-SPRINGEK(6,3)

        END
CCCCCCCCCCCCCCCCCCCCCCCCCCCCCCCCCCCCCCCCCCCCCCCCCCCCCCCCCCCCCCCCCCCCCCC


CCCCCCCCCCCCCCCCCCCCCCCCCCCCCCCCCCCCCCCCCCCCCCCCCCCCCCCCCCCCCCCCCCCCCCC
C     SUBROUTINE USED TO DEFINE PROPERTY FOR ROTATIONAL SPRING ELEMENT
CCCCCCCCCCCCCCCCCCCCCCCCCCCCCCCCCCCCCCCCCCCCCCCCCCCCCCCCCCCCCCCCCCCCCCC
      SUBROUTINE CALEMEF(EX,NELE,EK,EF,ETTOT,JELEM,JTYPE,ANGLE_SUB)
C********************************************************************
C    FUNCTION:
C    INPUT:
C      BY ENTRANCE:EX(13,3),NELE(13),JELEM,JTYPE
C    OUTPUT:
C      BY EXIT:EK(39,39),EF(39),ETTOT,ANGLE_SUB(2,1256,4,6)
C********************************************************************
      IMPLICIT DOUBLE PRECISION (A-H, O-Z)
        REAL*8 EX(13,3),EK(39,39),EF(3),ASTIFF(4),ANGLE_SUB(2,1256,4,6)
        REAL*8 X(4,3),PVPX(3),PPVPXPX(3,4,3),PCPN(2,3)
        INTEGER NELE(13),NN(3)
        DIMENSION NAORDER(2,2,4,12),NRANGE(2),N2(2,6),N3(2,6),N4(2,6)

        PI=DACOS(-1.D0)
        EK=0.D0
        EF=0.D0
        ET=0.D0
        ASTIFF(1)=1.D1       !ASTIFF stores stiffness values for
        ASTIFF(2)=1.D1       !different rotational springs
        ASTIFF(3)=1.D1
        ASTIFF(4)=1.D1

        NAORDER(1,1,1,1)=2   !Meaning of the index (elem type,
        NAORDER(1,1,1,2)=6   !situation num, stiff num, angle num)
        NAORDER(1,1,1,3)=8   !see details in APPENDIX D
        NAORDER(1,1,1,4)=7
        NAORDER(1,1,1,5)=3
        NAORDER(1,1,1,6)=9
        NAORDER(1,1,1,7)=4
        NAORDER(1,1,1,8)=7
        NAORDER(1,1,1,9)=10
        NAORDER(1,1,1,10)=6
        NAORDER(1,1,1,11)=5
        NAORDER(1,1,1,12)=11
```

```
NAORDER(1,1,2,1)=3
NAORDER(1,1,2,2)=2
NAORDER(1,1,2,3)=12
NAORDER(1,1,2,4)=5
NAORDER(1,1,2,5)=4
NAORDER(1,1,2,6)=13

NAORDER(1,2,3,1)=5
NAORDER(1,2,3,2)=2
NAORDER(1,2,3,3)=6
NAORDER(1,2,3,4)=3
NAORDER(1,2,3,5)=4
NAORDER(1,2,3,6)=7

NAORDER(1,2,4,1)=6
NAORDER(1,2,4,2)=3
NAORDER(1,2,4,3)=2
NAORDER(1,2,4,4)=2
NAORDER(1,2,4,5)=7
NAORDER(1,2,4,6)=3
NAORDER(1,2,4,7)=7
NAORDER(1,2,4,8)=5
NAORDER(1,2,4,9)=4
NAORDER(1,2,4,10)=4
NAORDER(1,2,4,11)=6
NAORDER(1,2,4,12)=5

NAORDER(2,1,3,1)=3
NAORDER(2,1,3,2)=2
NAORDER(2,1,3,3)=9
NAORDER(2,1,3,4)=6
NAORDER(2,1,3,5)=5
NAORDER(2,1,3,6)=12

NAORDER(2,1,4,1)=2
NAORDER(2,1,4,2)=7
NAORDER(2,1,4,3)=8
NAORDER(2,1,4,4)=4
NAORDER(2,1,4,5)=3
NAORDER(2,1,4,6)=10
NAORDER(2,1,4,7)=5
NAORDER(2,1,4,8)=4
NAORDER(2,1,4,9)=11
NAORDER(2,1,4,10)=7
NAORDER(2,1,4,11)=6
NAORDER(2,1,4,12)=13

NAORDER(2,2,1,1)=2
NAORDER(2,2,1,2)=4
NAORDER(2,2,1,3)=3
NAORDER(2,2,1,4)=4
NAORDER(2,2,1,5)=6
```

```
NAORDER(2,2,1,6)=5

NAORDER(2,2,2,1)=6
NAORDER(2,2,2,2)=2
NAORDER(2,2,2,3)=7

NAORDER(2,2,3,1)=3
NAORDER(2,2,3,2)=5
NAORDER(2,2,3,3)=4

NAORDER(2,2,4,1)=7
NAORDER(2,2,4,2)=3
NAORDER(2,2,4,3)=2
NAORDER(2,2,4,4)=5
NAORDER(2,2,4,5)=7
NAORDER(2,2,4,6)=6

NRANGE(1)=4  !number of situation combined with stiff
NRANGE(2)=6

N2(1,1)=1  !show which situation to use
N2(1,2)=1
N2(1,3)=2
N2(1,4)=2
N2(2,1)=1
N2(2,2)=1
N2(2,3)=2
N2(2,4)=2
N2(2,5)=2
N2(2,6)=2

N3(1,1)=1  !show which stiff to use
N3(1,2)=2
N3(1,3)=3
N3(1,4)=4
N3(2,1)=3
N3(2,2)=4
N3(2,3)=1
N3(2,4)=2
N3(2,5)=3
N3(2,6)=4

N4(1,1)=4  !number of angle for each stiff
N4(1,2)=2
N4(1,3)=2
N4(1,4)=4
N4(2,1)=2
N4(2,2)=4
N4(2,3)=2
N4(2,4)=1
N4(2,5)=1
N4(2,6)=2
```

```
        DO M=1,NRANGE(JTYPE)
          DO N=1,N4(JTYPE,M)
            J=N2(JTYPE,M)
            K=N3(JTYPE,M)
            L=N*3-2
            NN(1)=NAORDER(JTYPE,J,K,L)
            NN(2)=NAORDER(JTYPE,J,K,L+1)
            NN(3)=NAORDER(JTYPE,J,K,L+2)
            IF(NELE(NN(1)).EQ.1) NN(1)=1
            IF(NELE(NN(2)).EQ.1) NN(2)=1
            IF(NELE(NN(3)).EQ.1) NN(3)=1
              IF(NN(1).NE.1.AND.NN(2).NE.1.AND.NN(3).NE.1) THEN
              X(1,:)=EX(1,:)
              DO II=1,3
                X(II+1,:)=EX(NN(II),:) !assigning coordinates to X
              ENDDO                    !corresponding to NN(II)
              STIFF=ASTIFF(K)
              IF(JTYPE.EQ.2.AND.M.EQ.5) THEN  !'NUMBER' is for the
                NUMBER=N+2   !correction of the output of 'N' for type
                             !2 elements
              ELSEIF(JTYPE.EQ.2.AND.M.EQ.6) THEN
                NUMBER=N+4
              ELSE
                NUMBER=N
              ENDIF
                    EANGLE=ANGLE_SUB(JTYPE,JELEM,K,NUMBER)
              CALL
DIFF(EANGLE,STIFF,J,K,NUMBER,X,PVPX,PPVPXPX,ET,JELEM,
     &                  JTYPE)   !passing index "J" and X. Getting back
PVPX, PPVPXPX and ET
              ETTOT=ETTOT+ET
              EF(:)=EF(:)+PVPX(:)
              DO L=1,3
                DO I=1,4
                  DO J=1,3
                    IF (I.EQ.1) THEN
                      EK(L,J)=EK(L,J)+PPVPXPX(L,I,J) !for central atom
                    ELSE
                      EK(L,3*(NN(I-1)-1)+J)=EK(L,3*(NN(I-1)-1)+J)
     &                                       +0.5*PPVPXPX(L,I,J)
                      EK(3*(NN(I-1)-1)+J,L)=EK(L,3*(NN(I-1)-1)+J)
                    ENDIF
                  ENDDO
                ENDDO
              ENDDO
            ENDIF
          ENDDO
        ENDDO
*********************************************************************
*The section above is to fill the stiffness matrix. The leftest upper *
```

```
*is the Partial V / (Partial X(1)_L) Partial (X(1)_J). The transversal*
*3*36 and vertical 36*3 are the                                        *
*         0.5 Partial V / (Partial (X(1)_L) Partial (X(I)_J)),         *
*and the corresponding tranpose, respectively.                          *
* The coefficient 0.5 is used to avoid the double count of energy      *
* contributions.                                                       *
************************************************************************

      RETURN
      END
CCCCCCCCCCCCCCCCCCCCCCCCCCCCCCCCCCCCCCCCCCCCCCCCCCCCCCCCCCCCCCCCCCCCCCCCCC


CCCCCCCCCCCCCCCCCCCCCCCCCCCCCCCCCCCCCCCCCCCCCCCCCCCCCCCCCCCCCCCCCCCCCCCCCC
C   SUBROUTINE USED TO CALCULATE NECESSARY DERIVATIVES OF STRAIN ENERGY
CCCCCCCCCCCCCCCCCCCCCCCCCCCCCCCCCCCCCCCCCCCCCCCCCCCCCCCCCCCCCCCCCCCCCCCCCC
      SUBROUTINE DIFF(EANGLE,STIFF,JNUM,KNUM,NNUM,X,PVPX,PPVPXPX,ET,
     &                JELEM,JTYPE)
C***********************************************************************
C     INPUT:
C       BY ENTRANCE:X(4,3),JNUM,KNUM,STIFF,EANGLE,JELEM,JTYPE
C
C     OUTPUT:
C       BY EXIT:PVPX(3),PPVPXPX(3,4,3),ET
C***********************************************************************
      IMPLICIT DOUBLE PRECISION (A-H, O-Z)
        REAL*8 X(4,3),PVPX(3),PAPX(4,3),PCPN(2,3),ANORMAL1(3),
     &             ANORMAL2(3),PNPX(2,3,4,3),X1(3),X2(3),X3(3),X4(3),
     &          PXPXS(4,3,4,3),PPVPXPX(3,4,3),PPCPNPN(2,3,2,3),
     &          PPNPXPX(2,3,4,3,4,3),PART1(3,4,3),PART2(3,4,3),
     &          PPAPXPX(3,4,3)

C***********************************************************************
C       Calculate current value of dihedral angle according to current
C       nodal coordinates
C***********************************************************************
        CALL ALPHASUB(JNUM,X,X1,X2,X3,X4,ANORMAL1,ANORMAL2,COS_ALPHA
     &                   ,ALPHA)

C***********************************************************************
C       Initiate necessary values
C***********************************************************************
        PNPX = 0.D0
        PAPX = 0.D0
        PART1 = 0.D0
        PART2 = 0.D0
        PPVPXPX = 0.D0

C***********************************************************************
C       Calculation of necessary values
C***********************************************************************
        PVPA = STIFF*(ALPHA-EANGLE)
```

```
        PAPC = -1.D0/DSQRT(1.D0-COS_ALPHA**2.D0)
        PPAPCPC = -COS_ALPHA/(1.D0-COS_ALPHA**2.D0)**(3.D0/2.D0)
        PPVPAPA = STIFF
        IF((JTYPE.EQ.1).AND.(KNUM.EQ.1.OR.KNUM.EQ.2)) THEN
          ET = 0.5D0*0.5D0*STIFF*(ALPHA-EANGLE)**2.D0
        ELSEIF((JTYPE.EQ.1).AND.(KNUM.EQ.3.OR.KNUM.EQ.4)) THEN
          ET = 0.5D0*STIFF*(ALPHA-EANGLE)**2.D0
        ELSE
          ET = 0.D0
        ENDIF
        DO I=1,2
          DO J=1,3
            IF (I.EQ.1) THEN
              PCPN(I,J) = -ANORMAL2(J)
     &                    /(ANORMFC(ANORMAL1)*ANORMFC(ANORMAL2))
     &                      -ANORMAL1(J)*COS_ALPHA
     &                    /(ANORMFC(ANORMAL1))**2.D0
            ELSE
              PCPN(I,J) = -ANORMAL1(J)
     &                    /(ANORMFC(ANORMAL1)*ANORMFC(ANORMAL2))
     &                      -ANORMAL2(J)*COS_ALPHA
     &                    /(ANORMFC(ANORMAL2))**2.D0
            ENDIF
          ENDDO
        ENDDO

C*********************************************************************
C Below is for situation 1
C*********************************************************************
        IF(JNUM.EQ.1) THEN
          DO I=1,2
            DO J=1,3
              DO K=1,4
                DO L=1,3
                  IF (I.EQ.1.AND.K.EQ.1) THEN
                    DO M=1,3
                      PNPX(I,J,K,L) = PNPX(I,J,K,L)+EPS(J,L,M)*X2(M)
                    ENDDO
                  ELSEIF (I.EQ.1.AND.K.EQ.2) THEN
                    DO M=1,3
                      PNPX(I,J,K,L) = PNPX(I,J,K,L)+EPS(J,M,L)*X1(M)
                    ENDDO
                  ELSEIF (I.EQ.2.AND.K.EQ.3) THEN
                    DO M=1,3
                      PNPX(I,J,K,L) = PNPX(I,J,K,L)+EPS(J,L,M)*X4(M)
                    ENDDO
                  ELSEIF (I.EQ.2.AND.K.EQ.4) THEN
                    DO M=1,3
                      PNPX(I,J,K,L) = PNPX(I,J,K,L)+EPS(J,M,L)*X3(M)
                    ENDDO
                  ELSE
                    PNPX(I,J,K,L) = 0
```

```
                ENDIF
              ENDDO
            ENDDO
          ENDDO
        ENDDO

        DO I=1,4
          DO J=1,3
            DO K=1,4
              DO L=1,3
                IF (J.NE.L) THEN
                  PXPXS(I,J,K,L) = 0
                ELSE
                  IF ((I.EQ.1.AND.K.EQ.1).OR.(I.EQ.2.AND.K.EQ.1).OR.
     &                 (I.EQ.3.AND.K.EQ.4).OR.(I.EQ.4.AND.K.EQ.4)) THEN
                    PXPXS(I,J,K,L) = -1
                  ELSEIF ((I.EQ.1.AND.K.EQ.2).OR.(I.EQ.2.AND.K.EQ.3)
     &                 .OR.(I.EQ.3.AND.K.EQ.3).OR.(I.EQ.4.AND.K.EQ.2))
THEN
                    PXPXS(I,J,K,L) = 1
                  ELSE
                    PXPXS(I,J,K,L) = 0
                  ENDIF
                ENDIF
              ENDDO
            ENDDO
          ENDDO
        ENDDO

        DO M=1,4
          DO N=1,3
            DO I=1,2
              DO J=1,3
                DO K=1,4
                  DO L=1,3
                    PAPX(M,N) =
PAPX(M,N)+PAPC*PCPN(I,J)*PNPX(I,J,K,L)
     &                                          *PXPXS(K,L,M,N)
                  ENDDO
                ENDDO
              ENDDO
            ENDDO
          ENDDO
        ENDDO

        PVPX(:) = PVPA*PAPX(1,:)

C*********************************************************************
C Below is for second derivative for situation 1
C*********************************************************************
        DO I=1,2
          DO J=1,3
```

```
                DO K=1,2
                  DO L=1,3
                    IF (I.EQ.1.AND.K.EQ.1) THEN
                      PPCPNPN(I,J,K,L)=ANORMAL2(J)*ANORMAL1(L)/
     &
(ANORMFC(ANORMAL1)**3.D0*ANORMFC(ANORMAL2))-
     &                  DELTA(J,L)*COS_ALPHA/ANORMFC(ANORMAL1)**2.D0+
     &                  ANORMAL1(J)*ANORMAL2(L)/
     &
(ANORMFC(ANORMAL1)**3.D0*ANORMFC(ANORMAL2))+
     &                  3*ANORMAL1(J)*ANORMAL1(L)*COS_ALPHA/
     &                  ANORMFC(ANORMAL1)**4.D0
                    ELSEIF (I.EQ.1.AND.K.EQ.2) THEN
                      PPCPNPN(I,J,K,L)=-DELTA(J,L)/
     &                           (ANORMFC(ANORMAL1)*ANORMFC(ANORMAL2))+
     &                  ANORMAL2(J)*ANORMAL2(L)/
     &                  (ANORMFC(ANORMAL1)*ANORMFC(ANORMAL2)**3.D0)+
     &                  ANORMAL1(J)*ANORMAL2(L)*COS_ALPHA/
     &
(ANORMFC(ANORMAL1)**2.D0*ANORMFC(ANORMAL2)**2.D0)+
     &                  ANORMAL1(J)*ANORMAL1(L)/
     &                  (ANORMFC(ANORMAL1)**3.D0*ANORMFC(ANORMAL2))
                    ELSEIF (I.EQ.2.AND.K.EQ.1) THEN
                      PPCPNPN(I,J,K,L)=-DELTA(J,L)/
     &                           (ANORMFC(ANORMAL1)*ANORMFC(ANORMAL2))+
     &                  ANORMAL1(J)*ANORMAL1(L)/
     &                  (ANORMFC(ANORMAL1)**3.D0*ANORMFC(ANORMAL2))+
     &                  ANORMAL2(J)*ANORMAL1(L)*COS_ALPHA/
     &
(ANORMFC(ANORMAL1)**2.D0*ANORMFC(ANORMAL2)**2.D0)+
     &                  ANORMAL2(J)*ANORMAL2(L)/
     &                  (ANORMFC(ANORMAL1)*ANORMFC(ANORMAL2)**3.D0)
                    ELSEIF (I.EQ.2.AND.K.EQ.2) THEN
                      PPCPNPN(I,J,K,L)=ANORMAL1(J)*ANORMAL2(L)/
     &
(ANORMFC(ANORMAL1)*ANORMFC(ANORMAL2)**3.D0)-
     &                  DELTA(J,L)*COS_ALPHA/ANORMFC(ANORMAL2)**2.D0+
     &                  ANORMAL2(J)*ANORMAL1(L)/
     &
(ANORMFC(ANORMAL1)*ANORMFC(ANORMAL2)**3.D0)+
     &                  3*ANORMAL2(J)*ANORMAL2(L)*COS_ALPHA/
     &                  ANORMFC(ANORMAL2)**4.D0
                    ENDIF
                  ENDDO
                ENDDO
              ENDDO
            ENDDO

            DO I=1,2
              DO J=1,3
                DO K=1,4
                  DO L=1,3
```

```
                    DO M=1,4
                      DO N=1,3
                        IF (I.EQ.1.AND.K.EQ.1.AND.M.EQ.2) THEN
                          PPNPXPX(I,J,K,L,M,N)=EPS(J,L,N)
                        ELSEIF (I.EQ.1.AND.K.EQ.2.AND.M.EQ.1) THEN
                          PPNPXPX(I,J,K,L,M,N)=EPS(J,N,L)
                        ELSEIF (I.EQ.2.AND.K.EQ.3.AND.M.EQ.4) THEN
                          PPNPXPX(I,J,K,L,M,N)=EPS(J,L,N)
                        ELSEIF (I.EQ.2.AND.K.EQ.4.AND.M.EQ.3) THEN
                          PPNPXPX(I,J,K,L,M,N)=EPS(J,N,L)
                        ELSE
                          PPNPXPX(I,J,K,L,M,N)=0.DO
                        ENDIF
                      ENDDO
                    ENDDO
                  ENDDO
                ENDDO
              ENDDO

              DO I=1,2
                DO J=1,3
                  DO K=1,4
                    DO L=1,3
                      DO M=1,3
                        DO II=1,2
                          DO JJ=1,3
                            DO KK=1,4
                              DO LL=1,3
                                DO MM=1,4
                                  DO NN=1,3

PART1(M,MM,NN)=PART1(M,MM,NN)+PPCPNPN(I,J,II,JJ)*PNPX(I,J,K,L)
     &                       *PXPXS(K,L,1,M)*PNPX(II,JJ,KK,LL)
     &                       *PXPXS(KK,LL,MM,NN)
                                  ENDDO
                                ENDDO
                              ENDDO
                            ENDDO
                          ENDDO
                        ENDDO
                      ENDDO
                    ENDDO
                  ENDDO
                ENDDO

              DO I=1,2
                DO J=1,3
                  DO K=1,4
                    DO L=1,3
                      DO M=1,3
```

```
                    DO II=1,4
                      DO JJ=1,3
                        DO KK=1,4
                          DO LL=1,3

PART2(M,KK,LL)=PART2(M,KK,LL)+PCPN(I,J)*PPNPXPX(I,J,K,L,II,JJ)
     &                    *PXPXS(K,L,1,M)*PXPXS(II,JJ,KK,LL)
                          ENDDO
                        ENDDO
                      ENDDO
                    ENDDO
                  ENDDO
                ENDDO
              ENDDO
            ENDDO

            DO I=1,3
              DO J=1,4
                DO K=1,3
                  PPAPXPX(I,J,K)=PPAPCPC*PAPX(1,I)*PAPX(J,K)/PAPC**2.D0+
     &                                PAPC*PART1(I,J,K)+PAPC*PART2(I,J,K)
                ENDDO
              ENDDO
            ENDDO

            DO I=1,3
              DO J=1,4
                DO K=1,3
                  PPVPXPX(I,J,K)=PPVPAPA*PAPX(1,I)*
     &                                PAPX(J,K)+PVPA*PPAPXPX(I,J,K)
                ENDDO
              ENDDO
            ENDDO

          ENDIF

CCCCCCCCCCCCCCCCCCCCCCCCCCCCCCCCCCCCCCCCCCCCCCCCCCCCCCCCCCCCCCCCCCCCCCCCCC
C
C Below is for situation 2
CCCCCCCCCCCCCCCCCCCCCCCCCCCCCCCCCCCCCCCCCCCCCCCCCCCCCCCCCCCCCCCCCCCCCCCCCC
C
          IF(JNUM.EQ.2) THEN
            DO I=1,2
              DO J=1,3
                DO K=1,3
                  DO L=1,3
                    IF (I.EQ.1.AND.K.EQ.1) THEN
                      DO M=1,3
                        PNPX(I,J,K,L) = PNPX(I,J,K,L)+EPS(J,L,M)*X2(M)
                      ENDDO
                    ELSEIF (I.EQ.1.AND.K.EQ.2) THEN
```

```
                  DO M=1,3
                    PNPX(I,J,K,L) = PNPX(I,J,K,L)+EPS(J,M,L)*X1(M)
                  ENDDO
                ELSEIF (I.EQ.2.AND.K.EQ.3) THEN
                  DO M=1,3
                    PNPX(I,J,K,L) = PNPX(I,J,K,L)+EPS(J,L,M)*X1(M)
                  ENDDO
                ELSEIF (I.EQ.2.AND.K.EQ.1) THEN
                  DO M=1,3
                    PNPX(I,J,K,L) = PNPX(I,J,K,L)+EPS(J,M,L)*X3(M)
                  ENDDO
                ELSE
                  PNPX(I,J,K,L) = 0
                ENDIF
              ENDDO
            ENDDO
          ENDDO
        ENDDO

        DO I=1,3
          DO J=1,3
            DO K=1,4
              DO L=1,3
                IF (J.NE.L) THEN
                  PXPXS(I,J,K,L) = 0
                ELSE
                  IF ((I.EQ.1.AND.K.EQ.1).OR.(I.EQ.2.AND.K.EQ.1).OR.
     &                 (I.EQ.3.AND.K.EQ.1)) THEN
                    PXPXS(I,J,K,L) = -1
                  ELSEIF ((I.EQ.1.AND.K.EQ.4).OR.(I.EQ.2.AND.K.EQ.2)
     &                 .OR.(I.EQ.3.AND.K.EQ.3)) THEN
                    PXPXS(I,J,K,L) = 1
                  ELSE
                    PXPXS(I,J,K,L) = 0
                  ENDIF
                ENDIF
              ENDDO
            ENDDO
          ENDDO
        ENDDO

        DO M=1,4
          DO N=1,3
            DO I=1,2
              DO J=1,3
                DO K=1,3
                  DO L=1,3
                    PAPX(M,N) =
PAPX(M,N)+PAPC*PCPN(I,J)*PNPX(I,J,K,L)
     &                                        *PXPXS(K,L,M,N)
                  ENDDO
                ENDDO
```

```
              ENDDO
            ENDDO
          ENDDO
        ENDDO

        PVPX(:) = PVPA*PAPX(1,:)

C*********************************************************************
C Below is for second derivative for situation 2
C*********************************************************************
        DO I=1,2
          DO J=1,3
            DO K=1,2
              DO L=1,3
                IF (I.EQ.1.AND.K.EQ.1) THEN
                  PPCPNPN(I,J,K,L)=ANORMAL2(J)*ANORMAL1(L)/
     &
(ANORMFC(ANORMAL1)**3.D0*ANORMFC(ANORMAL2))-
     &                DELTA(J,L)*COS_ALPHA/ANORMFC(ANORMAL1)**2.D0+
     &                ANORMAL1(J)*ANORMAL2(L)/
     &
(ANORMFC(ANORMAL1)**3.D0*ANORMFC(ANORMAL2))+
     &                3*ANORMAL1(J)*ANORMAL1(L)*COS_ALPHA/
     &                ANORMFC(ANORMAL1)**4.D0
                ELSEIF (I.EQ.1.AND.K.EQ.2) THEN
                  PPCPNPN(I,J,K,L)=-DELTA(J,L)/
     &                      (ANORMFC(ANORMAL1)*ANORMFC(ANORMAL2))+
     &                ANORMAL2(J)*ANORMAL2(L)/
     &                (ANORMFC(ANORMAL1)*ANORMFC(ANORMAL2)**3.D0)+
     &                ANORMAL1(J)*ANORMAL2(L)*COS_ALPHA/
     &
(ANORMFC(ANORMAL1)**2.D0*ANORMFC(ANORMAL2)**2.D0)+
     &                ANORMAL1(J)*ANORMAL1(L)/
     &                (ANORMFC(ANORMAL1)**3.D0*ANORMFC(ANORMAL2))
                ELSEIF (I.EQ.2.AND.K.EQ.1) THEN
                  PPCPNPN(I,J,K,L)=-DELTA(J,L)/
     &                      (ANORMFC(ANORMAL1)*ANORMFC(ANORMAL2))+
     &                ANORMAL1(J)*ANORMAL1(L)/
     &                (ANORMFC(ANORMAL1)**3.D0*ANORMFC(ANORMAL2))+
     &                ANORMAL2(J)*ANORMAL1(L)*COS_ALPHA/
     &
(ANORMFC(ANORMAL1)**2.D0*ANORMFC(ANORMAL2)**2.D0)+
     &                ANORMAL2(J)*ANORMAL2(L)/
     &                (ANORMFC(ANORMAL1)*ANORMFC(ANORMAL2)**3.D0)
                ELSEIF (I.EQ.2.AND.K.EQ.2) THEN
                  PPCPNPN(I,J,K,L)=ANORMAL1(J)*ANORMAL2(L)/
     &
(ANORMFC(ANORMAL1)*ANORMFC(ANORMAL2)**3.D0)-
     &                DELTA(J,L)*COS_ALPHA/ANORMFC(ANORMAL2)**2.D0+
     &                ANORMAL2(J)*ANORMAL1(L)/
     &
(ANORMFC(ANORMAL1)*ANORMFC(ANORMAL2)**3.D0)+
```

```
     &                3*ANORMAL2(J)*ANORMAL2(L)*COS_ALPHA/
     &                ANORMFC(ANORMAL2)**4.D0
                    ENDIF
                  ENDDO
                ENDDO
              ENDDO
            ENDDO

            DO I=1,2
              DO J=1,3
                DO K=1,3
                  DO L=1,3
                    DO M=1,3
                      DO N=1,3
                        IF (I.EQ.1.AND.K.EQ.1.AND.M.EQ.2) THEN
                          PPNPXPX(I,J,K,L,M,N)=EPS(J,L,N)
                        ELSEIF (I.EQ.1.AND.K.EQ.2.AND.M.EQ.1) THEN
                          PPNPXPX(I,J,K,L,M,N)=EPS(J,N,L)
                        ELSEIF (I.EQ.2.AND.K.EQ.3.AND.M.EQ.1) THEN
                          PPNPXPX(I,J,K,L,M,N)=EPS(J,L,N)
                        ELSEIF (I.EQ.2.AND.K.EQ.1.AND.M.EQ.3) THEN
                          PPNPXPX(I,J,K,L,M,N)=EPS(J,N,L)
                        ELSE
                          PPNPXPX(I,J,K,L,M,N)=0.D0
                        ENDIF
                      ENDDO
                    ENDDO
                  ENDDO
                ENDDO
              ENDDO
            ENDDO

            DO I=1,2
              DO J=1,3
                DO K=1,3
                  DO L=1,3
                    DO M=1,3
                      DO II=1,2
                        DO JJ=1,3
                          DO KK=1,3
                            DO LL=1,3
                              DO MM=1,4
                                DO NN=1,3

PART1(M,MM,NN)=PART1(M,MM,NN)+PPCPNPN(I,J,II,JJ)*PNPX(I,J,K,L)
     &                  *PXPXS(K,L,1,M)*PNPX(II,JJ,KK,LL)
     &                  *PXPXS(KK,LL,MM,NN)
                                ENDDO
                              ENDDO
                            ENDDO
                          ENDDO
                        ENDDO
                      ENDDO
```

```
                    ENDDO
                  ENDDO
                ENDDO
              ENDDO
            ENDDO
          ENDDO

          DO I=1,2
            DO J=1,3
              DO K=1,3
                DO L=1,3
                  DO M=1,3
                    DO II=1,3
                      DO JJ=1,3
                        DO KK=1,4
                          DO LL=1,3

PART2(M,KK,LL)=PART2(M,KK,LL)+PCPN(I,J)*PPNPXPX(I,J,K,L,II,JJ)
     &                    *PXPXS(K,L,1,M)*PXPXS(II,JJ,KK,LL)
                          ENDDO
                        ENDDO
                      ENDDO
                    ENDDO
                  ENDDO
                ENDDO
              ENDDO
            ENDDO
          ENDDO

          DO I=1,3
            DO J=1,4
              DO K=1,3
                PPAPXPX(I,J,K)=PPAPCPC*PAPX(1,I)*PAPX(J,K)/PAPC**2.D0+
     &                         PAPC*PART1(I,J,K)+PAPC*PART2(I,J,K)
              ENDDO
            ENDDO
          ENDDO

              DO I=1,3
            DO J=1,4
              DO K=1,3
                PPVPXPX(I,J,K)=PPVPAPA*PAPX(1,I)*
     &                           PAPX(J,K)+PVPA*PPAPXPX(I,J,K)
              ENDDO
            ENDDO
          ENDDO

        ENDIF
      END
CCCCCCCCCCCCCCCCCCCCCCCCCCCCCCCCCCCCCCCCCCCCCCCCCCCCCCCCCCCCCCCCCCCCCCCCCCCCCC

CCCCCCCCCCCCCCCCCCCCCCCCCCCCCCCCCCCCCCCCCCCCCCCCCCCCCCCCCCCCCCCCCCCCCCCCCCCCC
```

```
C     SUBROUTINE USED TO CALCULATE ALPHA ANGLE AND RELATED QUANTITIES
CCCCCCCCCCCCCCCCCCCCCCCCCCCCCCCCCCCCCCCCCCCCCCCCCCCCCCCCCCCCCCCCCCCCCCCCCC
      SUBROUTINE ALPHASUB(J,X,X1,X2,X3,X4,ANORMAL1,ANORMAL2,COS_ALPHA
     &                    ,ALPHA)
      IMPLICIT DOUBLE PRECISION (A-H, O-Z)
        REAL*8 X(4,3),X1(3),X2(3),X3(3),X4(3),ANORMAL1(3),ANORMAL2(3)
        CALL COORD1SUB (J,X,X1)
        CALL COORD2SUB (J,X,X2)
        CALL COORD3SUB (J,X,X3)
        IF(J.EQ.1) THEN
          CALL COORD4SUB (J,X,X4)
        ENDIF
        ANORMAL1=0.D0
        ANORMAL2=0.D0
        DO I=1,3
          DO M=1,3
            DO N=1,3
              IF (J.EQ.1) THEN
                ANORMAL1(I)=ANORMAL1(I)+EPS(I,M,N)*X1(M)*X2(N)
              ENDIF
              IF (J.EQ.2) THEN
                ANORMAL1(I)=ANORMAL1(I)+EPS(I,M,N)*X1(M)*X2(N)
              ENDIF
            ENDDO
          ENDDO
        ENDDO
        DO I=1,3
          DO M=1,3
            DO N=1,3
              IF (J.EQ.1) THEN
                ANORMAL2(I)=ANORMAL2(I)+EPS(I,M,N)*X3(M)*X4(N)
              ENDIF
              IF (J.EQ.2) THEN
                ANORMAL2(I)=ANORMAL2(I)+EPS(I,M,N)*X3(M)*X1(N)
              ENDIF
            ENDDO
          ENDDO
        ENDDO

        COS_ALPHA = -DOT_PRODUCT(ANORMAL1,ANORMAL2)
     &              /((ANORMFC(ANORMAL1))*(ANORMFC(ANORMAL2)))
      IF(DABS(COS_ALPHA-1.D0).LE.1D-4) THEN
            COS_ALPHA=1.D0-1D-4
      ENDIF
      IF(DABS(COS_ALPHA+1.D0).LE.1D-4) THEN
            COS_ALPHA=-1.D0+1D-4
      ENDIF
      ALPHA=DACOS(COS_ALPHA)
      END
*************************************************************************
```

```
CCCCCCCCCCCCCCCCCCCCCCCCCCCCCCCCCCCCCCCCCCCCCCCCCCCCCCCCCCCCCCCCCCCCCCCCCC
        FUNCTION DISTANCE(X1,X2)
**********************************************************************
*     The distance between two points                                *
**********************************************************************
        IMPLICIT DOUBLE PRECISION (A-H, O-Z)
        REAL*8 DISTANCE
        REAL*8 X1(3),X2(3)
        DISTANCE = DSQRT((X1(1)-X2(1))**2.D0+(X1(2)-X2(2))**2.D0
     &         +(X1(3)-X2(3))**2.D0)
        RETURN
        END
**********************************************************************


CCCCCCCCCCCCCCCCCCCCCCCCCCCCCCCCCCCCCCCCCCCCCCCCCCCCCCCCCCCCCCCCCCCCCCCCCC
      FUNCTION DELTA(I,J)
**********************************************************************
* The function for Kronecker delta                                   *
**********************************************************************
      IMPLICIT DOUBLE PRECISION (A-H, O-Z)
        REAL*8 DELTA
        IF (I.EQ.J) THEN
          DELTA=1.D0
          RETURN
        ElSE
          DELTA=0.D0
          RETURN
        ENDIF
      END
**********************************************************************


CCCCCCCCCCCCCCCCCCCCCCCCCCCCCCCCCCCCCCCCCCCCCCCCCCCCCCCCCCCCCCCCCCCCCCCCCC
      FUNCTION EPS(I,J,K)
**********************************************************************
* The function for Levi-Civita symbol (epsilon)                      *
**********************************************************************
      IMPLICIT DOUBLE PRECISION (A-H, O-Z)
        REAL*8 EPS
        IF ((I.EQ.1.AND.J.EQ.2.AND.K.EQ.3)
     &   .OR.(I.EQ.2.AND.J.EQ.3.AND.K.EQ.1)
     &   .OR.(I.EQ.3.AND.J.EQ.1.AND.K.EQ.2)) THEN
          EPS=1.D0
          RETURN
        ELSEIF ((I.EQ.3.AND.J.EQ.2.AND.K.EQ.1)
     &   .OR.(I.EQ.2.AND.J.EQ.1.AND.K.EQ.3)
     &   .OR.(I.EQ.1.AND.J.EQ.3.AND.K.EQ.2)) THEN
          EPS=-1.D0
          RETURN
        ElSE
          EPS=0.D0
```

```
        RETURN
      ENDIF
    END
*************************************************************************


CCCCCCCCCCCCCCCCCCCCCCCCCCCCCCCCCCCCCCCCCCCCCCCCCCCCCCCCCCCCCCCCCCCCCCCCCC
      FUNCTION ANORMFC(X)
*************************************************************************
* The norm of vector "X"                                                *
*************************************************************************
      IMPLICIT DOUBLE PRECISION (A-H, O-Z)
      REAL*8 X(3)
        ANORMFC=DSQRT((X(1))**2.D0+(X(2))**2.D0+(X(3))**2.D0)
      END
*************************************************************************


CCCCCCCCCCCCCCCCCCCCCCCCCCCCCCCCCCCCCCCCCCCCCCCCCCCCCCCCCCCCCCCCCCCCCCCCCC
      SUBROUTINE COORD1SUB (J,X,X1)
*************************************************************************
* Calculate vector X1 ("J" is the situation number)                     *
*************************************************************************
      IMPLICIT DOUBLE PRECISION (A-H, O-Z)
        REAL*8 X(4,3),X1(3)
        IF (J.EQ.1) THEN
          X1(:)=X(2,:)-X(1,:)
          RETURN
        ENDIF
        IF (J.EQ.2) THEN
          X1(:)=X(4,:)-X(1,:)
          RETURN
        ENDIF
      END
*************************************************************************
CCCCCCCCCCCCCCCCCCCCCCCCCCCCCCCCCCCCCCCCCCCCCCCCCCCCCCCCCCCCCCCCCCCCCCCCCC
      SUBROUTINE COORD2SUB (J,X,X2)
*************************************************************************
* Calculate vector X2 ("J" is the situation number)                     *
*************************************************************************
      IMPLICIT DOUBLE PRECISION (A-H, O-Z)
        REAL*8 X(4,3),X2(3)
        IF (J.EQ.1) THEN
          X2(:)=X(3,:)-X(1,:)
          RETURN
        ENDIF
        IF (J.EQ.2) THEN
          X2(:)=X(2,:)-X(1,:)
          RETURN
        ENDIF
      END
*************************************************************************
```

```
CCCCCCCCCCCCCCCCCCCCCCCCCCCCCCCCCCCCCCCCCCCCCCCCCCCCCCCCCCCCCCCCCCCCCCCCCCCC
      SUBROUTINE COORD3SUB (J,X,X3)
**********************************************************************
* Calculate vector X3 ("J" is the situation number)                  *
**********************************************************************
      IMPLICIT DOUBLE PRECISION (A-H, O-Z)
        REAL*8 X(4,3),X3(3)
        IF (J.EQ.1) THEN
          X3(:)=X(3,:)-X(4,:)
          RETURN
        ENDIF
        IF (J.EQ.2) THEN
          X3(:)=X(3,:)-X(1,:)
          RETURN
        ENDIF
      END
**********************************************************************
CCCCCCCCCCCCCCCCCCCCCCCCCCCCCCCCCCCCCCCCCCCCCCCCCCCCCCCCCCCCCCCCCCCCCCCCCCCC
      SUBROUTINE COORD4SUB (J,X,X4)
**********************************************************************
* Calculate vector X4 ("J" is the situation number)                  *
**********************************************************************
      IMPLICIT DOUBLE PRECISION (A-H, O-Z)
        REAL*8 X(4,3),X4(3)
        IF (J.EQ.1) THEN
          X4(:)=X(2,:)-X(4,:)
          RETURN
        ENDIF
      END
**********************************************************************
```

APPENDIX F

PDMS WALL PATTERNS FOR FABRICATION OF SILICON NANOMEMBERANCE

The detailed geometry of the pre-patterned PDMS wall for Miura-ori pattern is given in Fig. A4, A and B.

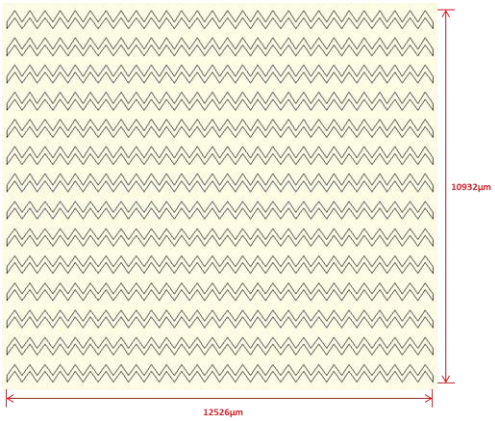

A

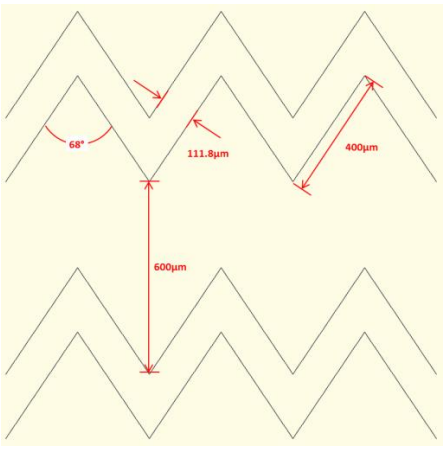

B

Fig. A4. Geometry of the pre-patterned PDMS wall with Miura-ori pattern. (**A**) Overall dimension. (**B**) Detailed dimension.

The detailed geometry of the pre-patterned PDMS wall for water bomb pattern is given in Fig. A5, A and B.

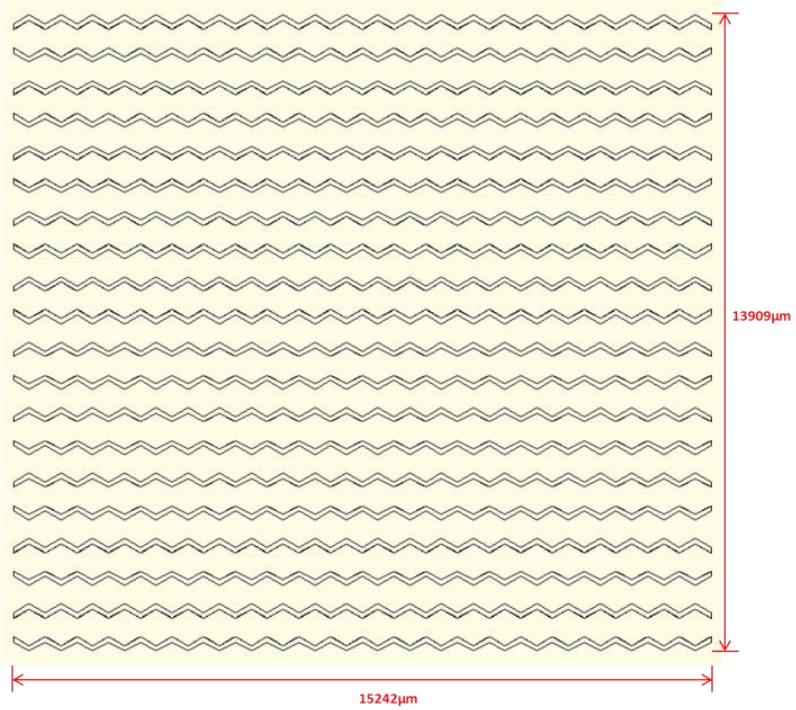

A

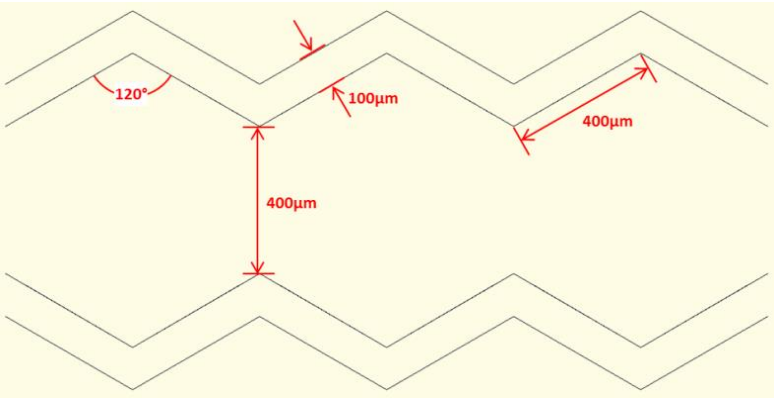

B

Fig. A5. Geometry of the pre-patterned PDMS wall with magic ball pattern. (**A**) Overall dimension. (**B**) Detailed dimension.

The detailed geometry of the pre-patterned PDMS wall for non-rigidly foldable pattern is given in Fig. A6, A and B.

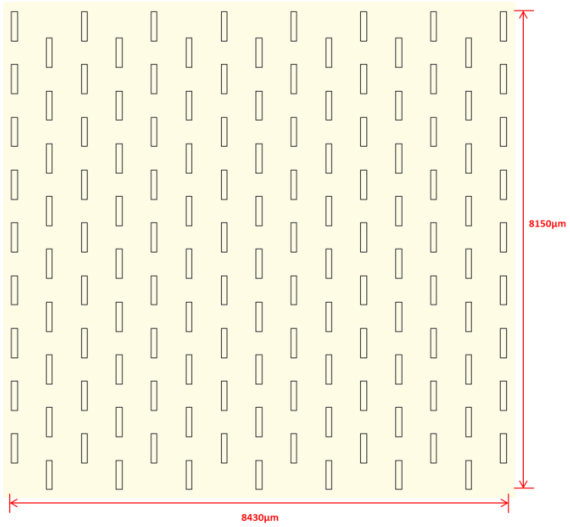

A

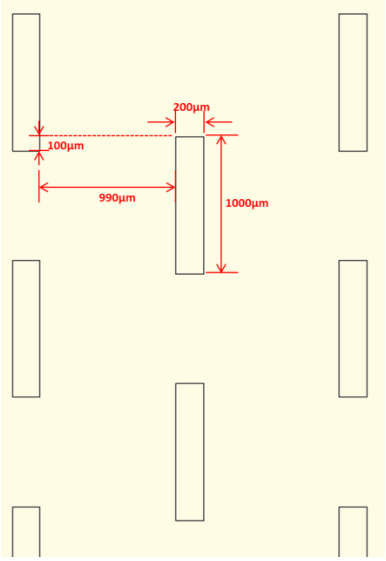

B

Fig. A6. Geometry of the pre-patterned PDMS wall with non-rigidly foldable pattern. (**A**) Overall dimension. (**B**) Detailed dimension.

The detailed geometry of the pre-patterned PDMS wall for stars pattern is given in Fig. A7, A and B.

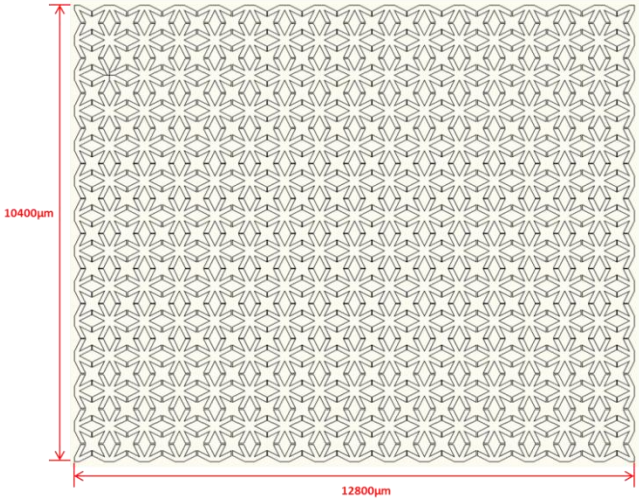

A

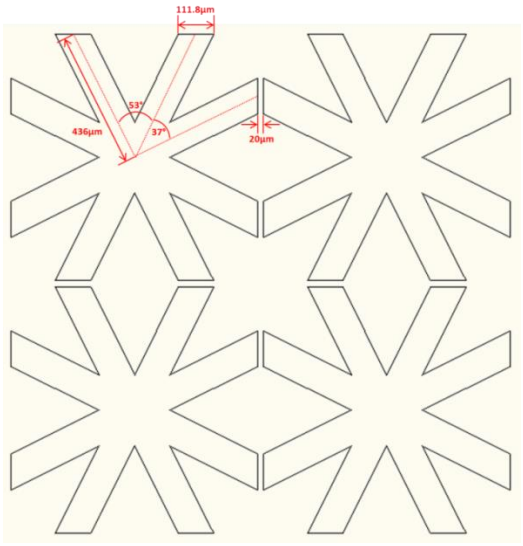

B

Fig. A7. Geometry of the pre-patterned PDMS wall with star pattern. (**A**) Overall dimension. (**B**) Detailed dimension.

The detailed geometry of the pre-patterned PDMS wall for US Flag pattern is given in Fig. A8, A, B and C.

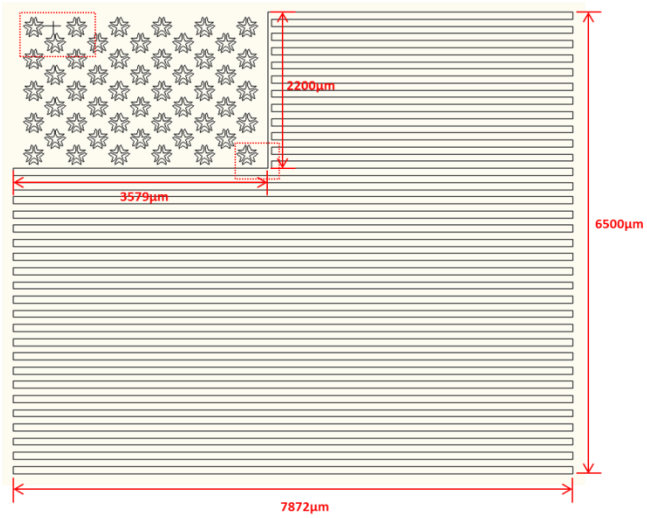

A

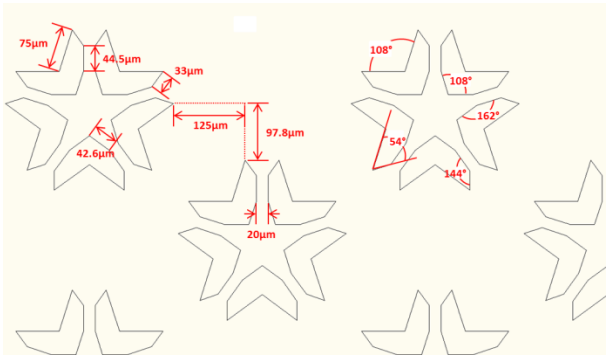

B

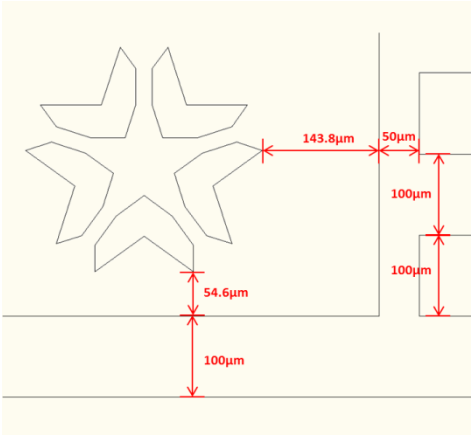

C

Fig. A8. Geometry of the pre-patterned PDMS wall with US flag pattern. (**A**) Overall dimension. (**B**) Detailed dimension. (**C**) Detailed dimension near the boundary of star pattern and strip pattern.

APPENDIX G

DERIVATION OF ANALYTIC SOLUTION FOR MIURA-ORI AND WATER BOMB PATTERN

Fig. A9, A and B show the 3D view and the top view of the unit cell of a Miura-ori pattern. The origin of stationary coordinate system is "O". Due to the biaxial compressive strain (<0), the overall strain of the pattern in y-direction due to the biaxial compression is ε, thus the stretch ratio in y-direction is $\lambda = 1-\varepsilon$. The length of line BC and AB are assumed to be a and b, respectively. The angle $\angle ABC$ is denoted as β. Then we can obtain the vector $\overrightarrow{OA} = \left(0, -a\lambda, -a\sqrt{1-\lambda^2}\right)$, and $\overrightarrow{OC} = \left(b\sqrt{1-\left[\cos\beta/\lambda\right]^2}, -b\cos\beta/\lambda, 0\right)$. The normal vector of the plane OABC is then $\mathbf{n} = \overrightarrow{OA} \times \overrightarrow{OC}$. As the origin O is in this plane, the equation of the plane can be shown as: $A_1 x + A_2 y + A_3 z = 0$ ($0 < x < B_2$, $B_1 x / B_2 - a\lambda < y < B_1 x / B_2$), where $A_1 = -ab\sqrt{1-\lambda^2}\cos\beta/\lambda$, $A_2 = -ab\sqrt{\left(1-\lambda^2\right)\left[1-\left(\cos\beta/\lambda\right)^2\right]}$, $A_3 = ab\lambda\sqrt{1-\left(\cos\beta/\lambda\right)^2}$, $B_1 = -\left(b\cos\beta\right)$, and $B_2 = b\sqrt{1-\left(\cos\beta/\lambda\right)^2}$.

Similarly, the equation of the plane OCDE is: $-A_1 x - A_2 y + A_3 z = 0$ ($0 < x < B_2$, $B_1 x / B_2 < y < B_1 x / B_2 + a\lambda$). The equation of the plane OAFG is: $-A_1 x + A_2 y + A_3 z = 0$ ($-B_2 < x < 0$ $-B_1 x / B_2 - a\lambda < y < -B_1 x / B_2$). The equation of the plane OEGH is: $A_1 x - A_2 y + A_3 z = 0$ ($0 < x < B_2$, $-B_1 x / B_2 < y < -B_1 x / B_2 + a\lambda$).

In both FEA and the experiment, we have the following dimensions: $a = 400\mu m$ (include the dimension of wall on y-direction), $b = 400\mu m$, $\beta = 34^\circ$, $\lambda = 96.4\%$. Then we can obtain the constants as: $A_1 = -36588$, $A_2 = -21710$, $A_3 = 78708$, $B_1 = 331.6150$, $B_2 = -204.1193$. For the line cut by the yz-plane, we need only to solve the equations:

$$\begin{cases} A_1x + A_2y + A_3z = 0 \\ x = 0 \end{cases} \text{ for line EO and } \begin{cases} -A_1x - A_2y + A_3z = 0 \\ x = 0 \end{cases} \text{ for line OA.}$$

After proper offset, we can obtain the theoretical profile for Miura-ori in y-direction, which is shown in Fig. 5.4. Similarly, the other two profiles for Miura-ori can be obtained.

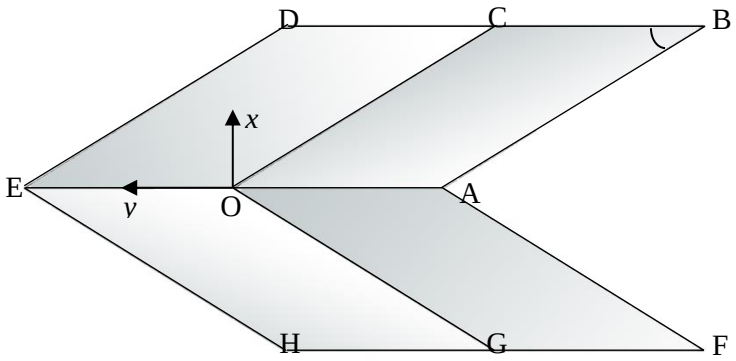

A

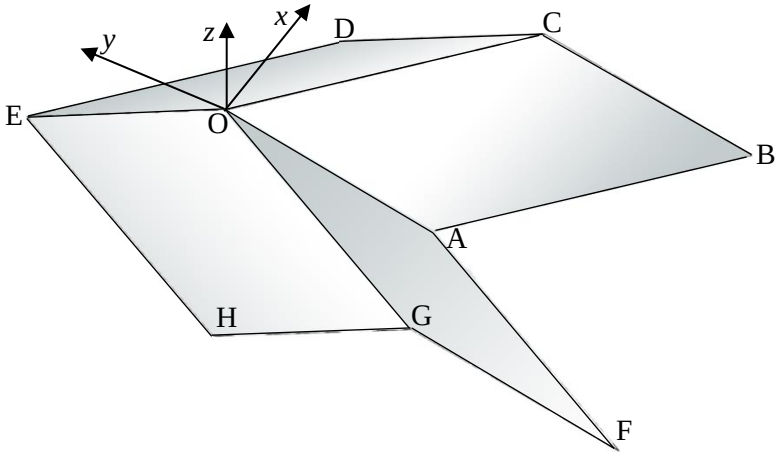

B

Fig. A9. Analytical geometry of a unit cell for Miura-ori pattern. (**A**) Top view. (**B**) Perspective view.

3D view and the cross section view (cut along the plane COF) of the unit cell of the water bomb pattern are shown in Fig. A10, A and B. The origin of stationary coordinate system is "O". Assuming we know the overall strain ε of the pattern in x-direction due to the biaxial compression, the stretch ratio in x-direction is $\lambda = 1-\varepsilon$. The length of line BC and OC are assumed to be a and b, respectively. Then we can obtain the vector $\overrightarrow{OC} = (0, a\sin\theta, a\cos\theta)$, $\overrightarrow{OB} = \left(-a\lambda, b, a\sqrt{1-\lambda^2}\right)$, where, $\theta = \arctan\left(1/\sqrt{1-\lambda^2}\right) - \arctan\left(\sqrt{1-\lambda^2}\right)$. The normal vector of the plane OBC is then $\mathbf{n} = \overrightarrow{OC} \times \overrightarrow{OB}$. As the origin O is in this plane, the equation of the plane can be shown as: $C_1 x + C_2 y + C_3 z = 0$ ($x < 0$, $bx + a\lambda y > 0$, $(b - a\sin\theta)x + a\lambda(y - a\sin\theta) < 0$), where, $C_1 = a^2 \sin\theta\sqrt{1-\lambda^2} - ab\cos\theta$, $C_2 = a^2\lambda\cos\theta$, $C_3 = -a^2\lambda\sin\theta$.

Similarly, the equation of the plane OCD is: $-C_1 x + C_2 y + C_3 z = 0$ ($x > 0$, $-bx + a\lambda y > 0$, $(b - a\sin\theta)x - a\lambda(y - a\sin\theta) > 0$). The equation of the plane ODE is: $\sqrt{1-\lambda^2}\,x - \lambda z = 0$ ($x < a\lambda$, $-bx + a\lambda y < 0$, $bx + a\lambda y > 0$). The equation of the plane OEF is: $-C_1 x - C_2 y + C_3 z = 0$ ($x > 0$, $bx + a\lambda y < 0$, $(b - a\sin\theta)x + a\lambda(y + a\sin\theta) > 0$). The equation of the plane OAF is: $C_1 x - C_2 y + C_3 z = 0$ ($x < 0$, $-bx + a\lambda y < 0$, $(b - a\sin\theta)x - a\lambda(y + a\sin\theta) < 0$). The equation of the plane OAB is: $\sqrt{1-\lambda^2}\,x + \lambda z = 0$ ($x > -a\lambda$, $-bx + a\lambda y > 0$, $bx + a\lambda y < 0$).

In the experiment, we have the following dimensions: $a = 400\mu m$, $b = 457.735\mu m$ (include the dimension of wall on y-direction), $\lambda = 96.4\%$. Then we can obtain the constants as: $\theta = 60.22^{\circ}$, $C_1 = -54015$, $C_2 = 76609$, $C_3 = 133870$.

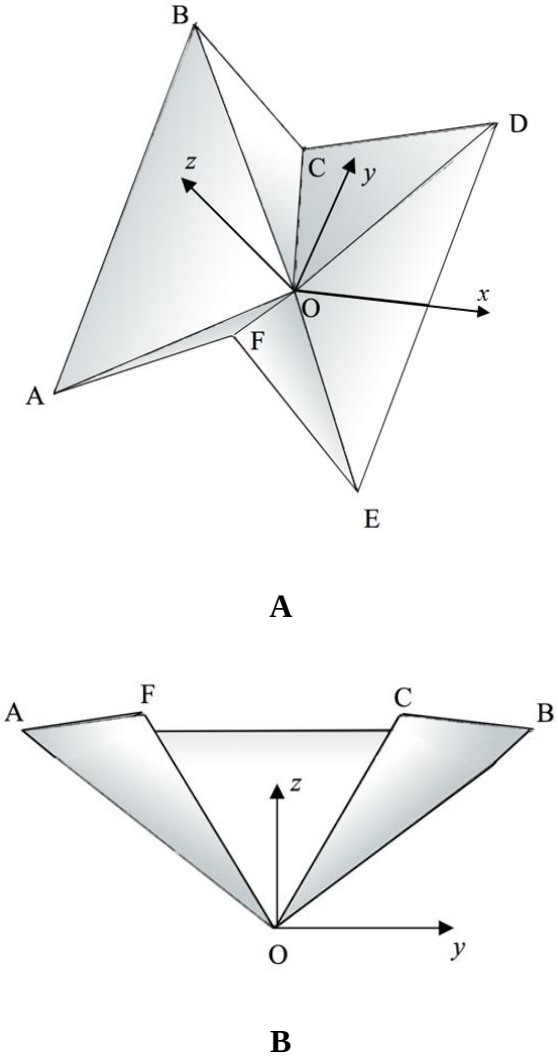

Fig. A10. Analytical geometry of a unit cell for waterbomb pattern. (**A**) Perspective view. (**B**) Side view.